Direct Numeric Simulation of Shock Wave Structures without the Use of Artificial Viscosity

Kenneth Bernard Jordan
Marquette University

DIRECT NUMERIC SIMULATION OF SHOCK WAVE STRUCTURES WITHOUT THE USE OF ARTIFICIAL VISCOSITY

by

Kenneth B Jordan, B.S., M.S.

A Dissertation submitted to the Faculty of the Graduate School,
Marquette University,
In Partial Fulfillment of the Requirements for
The Degree of Doctor of Philosophy

Milwaukee, Wisconsin

August 2011

ABSTRACT
DIRECT NUMERIC SIMULATION OF SHOCK WAVE STRUCTURES
WITHOUT THE USE OF ARTIFICIAL VISCOSITY

Kenneth B Jordan, B.S., M.S.

Marquette University, 2011

The purpose of this work is to directly simulate shock wave structures without the use of artificial viscosity. The commonly used artificial viscosity model is replaced with an irreversibility model. Irreversibilities are not typically taken into account when modeling the shock processes because shocks are resolved in a large domain where the thickness of the shock is thin compared to the numeric grid resolution. The result is the shock is poorly resolved. In addition processes other than shock processes are adiabatic and reversible. The result is artificial viscosity, a form of irreversibility, is added to the numeric cells near the shock in order to account for the irreversibilities generated within the shock structure. In this work the shocks are resolved and the physical sources of irreversibilities, namely viscous dissipation and localized heat transfer, are directly incorporated within the shock process. The resulting simulations yield a more realistic shock structure, the shape of which can be integrated to determine the resulting increase in entropy of the shocked material. Metrics such as shock thickness and wave structure compare favorably to experimental results.

Irreversibility is traditionally accounted for by inserting artificial viscosity into the energy balance. Artificial viscosity reduces numerical overshoot, diminishes the total energy, and smears out the shock front over several cells thereby eliminating the need for nanoscale grid resolution necessary to resolve the shock front and numerically resolve the gradients. This approach fails to correctly model the shock wave structure of distended materials because their dynamic loading is a highly dissipative process and completely irreversible. Thus, the work described herein models on a bulk scale a thermodynamically consistent representation of the irreversibilities associated with shock wave formation such as viscous dissipation and heat conduction and seeks to determine if these sources of irreversibility are comparable to artificial viscosity.

ACKNOWLEDGMENTS

Kenneth B. Jordan, B.S., M.S.

I would like to thank Dr. John P. Borg for his assistance and guidance in this work, and for opening doors of opportunity for me to advance my engineering career. I also want to thank Dr. Nigro for his words of encouragement and Dr. Bowman for his technical insight, and Dr. Riesel for directing my research efforts and helping me obtain my MS in Mechanical Engineering from UWM. I would like to thank my wife and parents for their support and encouragement. Finally, I would like to thank the Graduate School and the Department of Mechanical Engineering at Marquette University.

TABLE OF CONTENTS

LIST OF TABLES

LIST OF FIGURES

Chapter 1

Introduction

Chapter 1 of this dissertation presents the objectives and goals of this work as well as the methodology that was used in its completion and a literature review.

1.1 Objectives & Goals

The purpose of this dissertation is to develop a better understanding of how porous/granular materials behave when subjected to shock loading. This will be achieved through understanding the role of irreversibilities which arise from such phenomena as void collapse, internal heating, and initial porosity in the dynamic compaction of porous/granular materials. The secondary objective of this dissertation is to use entropy to replace the artificial viscosity model [1, 2, 3] currently implemented in hydrocode formulations because it contains parameters not linked to physical properties.

The goal of this research is to enhance existing continuum computational models and/or equations of state, or develop new models and/or equations of state that simulate the physical behavior of porous/granular materials experiencing shock loading. Continuum models currently in use originated within distinct scientific communities to address a particular class of problems. Therefore, these models are not readily applicable to other situations. Currently continuum level modeling does not directly couple grain level dynamics such as void collapse, plastic flow, or heating to the bulk simulation and they include parameters not linked to material properties. This research work proposes

that grain level dynamics and irreversibilities can be summarized into continuum mechanics and thermodynamics via heat conduction and viscous dissipation.

1.2 Methodology

This work used a combined numeric and analytic approach supplemented with experimental data to accomplish the stated research objectives. A variety of methods were used to improve the numeric simulations of porous/granular materials including incorporating entropy production into the conservation equations, and using a higher order polynomial in the Mie-Grüneisen equation of state.

Irreversibilities are directly accounted for in the governing equations by the inclusion of viscous dissipation and heat conduction which eliminates the need for an additional constitutive relation such as artificial viscosity. This approach removes the need to directly calculate entropy states which are not directly measurable and cannot be validated by comparison to experimental data. This methodology was initially tested on an ideal monatomic gas, before being applied to liquids, heterogeneous and homogeneous solids. The results of the ideal monatomic gas simulations were compared to a well known analytic solution as well as to available experimental data. The governing equations used in the numeric formulation are the Navier-Stokes (NS) equations. The use of the Navier-Stokes equations makes for a more complete analysis because this set of equations is thermodynamically consistent because they include temperature. This contrasts with most hydrocode formulations that do not include temperature in their derivation. The one-dimensional plane flow Navie-Stokes equations were implemented in a non-dimensional second order accurate Eulerian hydrocode formulation called NS. The unique contribution to this field of study is found in applying the Navier-Stokes

equations to porous/granular materials experiencing shock loading. The numeric results were assessed by comparison to one-dimensional shock wave experiments and analytic solutions were available.

1.3 Literature Review

The research thrusts of this work are centered on improving the predictive capabilities of hydrocodes when applied to porous/granular materials by replacing grain level dynamics with irreversibilities based on bulk scale thermodynamic concepts. To complete the assigned task a thorough understanding of hydrocodes, experimental methods, and analytic techniques are needed.

1.3.1 Literature Review - Experimental

Until recently most of the experimental work involving porous/granular materials has revolved around the dynamic compaction of ductile metallic powders such as copper and iron. An early pioneer in this area was Hermann, who, in 1969, conducted one dimensional (plain strain) experiments on iron powder and suggested the use of the P-α equation of state to model the compaction event. The P-α model relates the density of the distended material to its fully consolidated density through $\alpha = \rho_{distended}/\rho_{consolidated}$ which is tuned to the experimental data [10]. This continuum level model provides an additional constitutive equation which describes the removal of porosity and therefore facilitates the improved predictive capabilities of hydrocodes. In recent years the use of ceramic powders, plastics/polymers, rubber, and composite materials has become common place, which has spurred the need for new models or equations of state. Work with metallic powders continues today and efforts by W. J. Nellis and D. J. Benson in their 1994 work with “Dynamic compaction of copper powder: Computation and

experiment" is considered essential reading. Benson and Nellis used mesoscale simulations to directly simulate grain on grain interactions thereby removing porosity and the need for additional constitutive model such as the P-α model. Mesoscale simulations track the individual grains that make up the distended material and models their morphology during the compaction event. This approach is vastly different from the continuum approach which views the distended material as a continuous material with different properties from the fully consolidated form. This work is concerned with modeling the dynamic compaction of porous silica powder on a continuum level without the aid of a porosity constitutive model. Experiments conducted by D.J. Chaptman et al and J. P. Borg et al in 2005 used wet silica and dry silica respectively with density values as low as 0.1 g/cc. Today there is great interest in the shock loading response of wet and dry silica because of their strategic importance to the military.

1.3.2 Literature Review – Computational

The original goal of this work was to use a Lagrangian hydrocode formulation (KO) based on Wilkins Hemp code [2] to model such phenomena as void collapse, internal heating, and initial porosity in the dynamic compaction of porous/granular materials. There has been a lot of work performed in reference to modeling grain dynamics such as R. L. Williams in his 1990 work "Parametric studies of dynamic powder consolidation using a particle-level numerical model". D. J. Benson in 1994 studied the effect of particle morphology in his work "An analysis by direct numerical simulation of the effects of particle morphology on the shock compaction of copper powder". Grain level dynamics such as void collapse, frictional heating, and jetting etc were studied and modeled by Tang, Horie, and Psakhie in their 1997 work "Discrete

Meso-Element Modeling of Shock Processes in Powders". In contrast to the grain level approach which directly simulates the grain on grain iterations the continuum level approach has historically relied upon constitutive models such as the P-α compaction model, the Snow Plow compaction model, and Meyers Porous compaction model to simulate the dynamic compaction of porous materials [9, 10, 23]. Continuum level models such as snow-plow [4], p-α [5], p-λ [6], or CAP models [7] were created within distinct communities to deal with a specific class of problems. In general they fail to result in adequate predictive capabilities for various high strain rates, and low density to volume materials. Following a careful review of the open literature and examining our own work it became apparent that the equation of state was the key component to accurately model on bulk scale porous/granular materials. This thrust lead to modifying the commonly used Mie-Grüneisen equation of state [14]. Details concerning the modifications made to the Mie-Grüneisen are contained in Chapter 5 of this work. While this effort produced results that represent an improvement over the standard Mie-Grüneisen equation of state as applied to porous silica it failed to adequately replicate pressure signatures across the entire velocity and density ranges tested.

As an alternative approach to using a Lagrangian formulation and trying to modify an existing equation of state the decision was made to switch to an Eulerian formulation. Many of the commercially available hydrocodes are Eulerian based such as CTH. The Eulerian hydrocode formulation is a departure from the Lagrangian formulation that was initially used in this work. The benefit of using a Lagrangian formulation over an Eulerian formulation is the Lagrangian formulation enables tracking of grain on grain interactions and grain morphology which isn't possible with an Eulerian

formulation. The primary advantage to using an Eulerian formulation over a Lagrangian formulation is that Eulerian formulations are better suited to deal with the large deformations present in shock problems [10], because an Eulerian mesh does not experience entanglement or other mesh related problems that occur with a Lagrangian formulation. D.J. Benson discusses in details the differences between Eulerian and Lagrangian formulations in his 1990 paper "Computational Methods in Lagrangian and Eulerian Hydrocodes".

The artificial viscosity model frequently used in modern hydrocodes was first proposed by J. Von Neuman and R. Richtmyer in 1949 [1]. A secondary term was added by Landshoff in 1955 [12]. Artificial viscosity smears out the shock front eliminating the need for nanoscale resolution and dampens out numerical overshooting. Alternative methods of simulating shocks without the use of artificial viscosity occur in gas dynamics with the use of the Navier-Stokes equations. The application of the Navier-Stokes equations to an ideal monatomic gas follows the work of G. T. Elizarova in 2005 and 2007 where the Navier-Stokes equations were applied to helium, nitrogen and argon gas [13,27,28]. This work involved simulating the shock wave structure of an ideal monatomic gas and predicting shock thickness without the use of artificial viscosity. Artificial viscosity was replaced with viscous dissipation and heat conduction within the shock front. This work was extended by comparing the numeric solution to an exact analytic.

1.3.3 Literature Review - Analytic

There are two analytic solutions presented in this work. The first solution is the higher order polynomial for the cold curve compression contribution to the pressure

function of the Mie-Grüneisen equation of state [1, 9]. The Mie-Grüneisen equation of state is a functional relationship for pressure corresponding to changes in volume and internal energy. This constitutive relation was developed for fully consolidated metals. The Mie-Grüneisen equation of state is routinely used in commercially available codes such as CTH, and is typically represented by either a third order polynomial or a fifth order polynomial that is an exact fit to experimental data. The second analytic solution is for a standing shock wave in an ideal gas. The complete solution is presented in Bird, Stewart and Lightfoot Transport Phenomena. The successful application of the Navier-Stokes (NS) equations to an ideal monatomic gas has provided proof that viscous dissipation and heat conduction can be used to replace artificial viscosity in the simulation of shock waves. The analytic solution and the NS formulation are computational stable and do not contain non-physical parameters. The analytic solution is nondimensional and assumes constant viscosity and does an adequate job modeling shock wave structures in gases. Using the NS formulation to directly model the shock wave structure presented the opportunity to compare a computational simulation to an analytic solution and experimental results. Good agreement between the three indicates that this approach is valid and should be studied further. The new contribution of this work to this field is the application of the Navier-Stokes equations to shock waves in incompressible substances.

Chapter 2

Introduction to Shock Physics

2.1 Shock Waves

Shock waves are nearly instantaneous changes in the particle velocity, pressure, temperature, entropy, and density in a solid, liquid, or gaseous medium [8]. Shock waves form when a wave following the loading profile of an initial disturbance moves faster than the leading edge. The increase in the trailing edge velocity occurs because the sound speed of a material increases as the density increases. In other words the leading edge of the shock wave compresses the material thereby increasing the density. Subsequently, the portion of the wave traveling through the higher density material moves faster until it catches the leading edge. This steep wave is now a nearly instantaneous change in the material state and is called a shock wave. This is graphically illustrated below in Fig. 2.1.1.

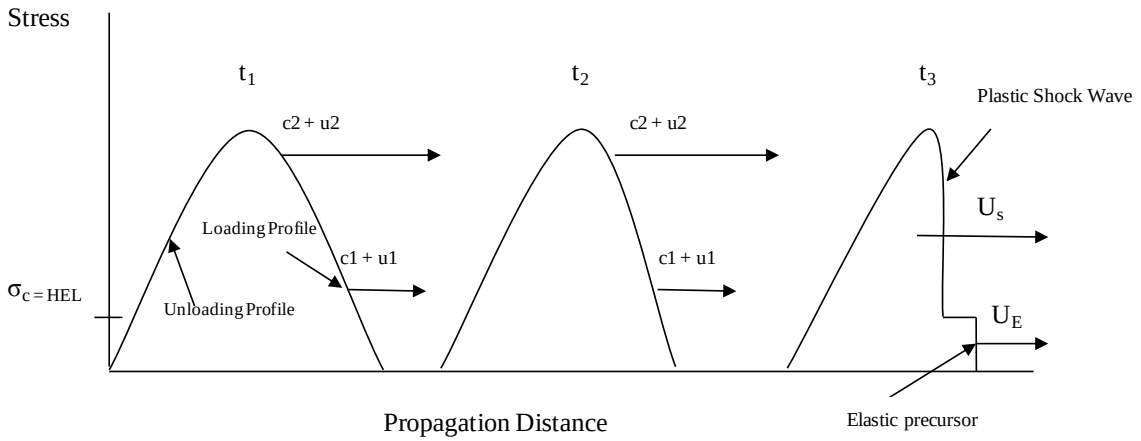

Figure 2.1.1: Disturbance moves at a speed of c + u, when the stress is above σ_c which is the critical stress (Hugoniot Elastic Limit) for plastic deformation, c is the sound speed of material which is f(ρ), u is the particle speed, and U is the speed of the shock wave. For stability $U \geq u+c$ [8].

Shock front thicknesses are finite and on the order of the molecular mean free path of the medium, on the order of four times mean free path length for gases and on the order of the mean free path length for solids. These small length scales are usually considered to be too minute to resolve numerically. However, using the NS formulation, with very high computational resolution, we were able to numerically resolve the shock front in argon gas under various loading conditions. Irreversible conditions exist within the shock front due to plastic deformation (solids), viscous shear stress and heat conduction (solids, liquids, gases) as material flows in the direction of the shock. While conditions in the shock front are not adiabatic, irreversible, and not in equilibrium, outside the shock front the material is assumed to be adiabatic and reversible. This is graphically illustrated in Fig. 2.1.2.

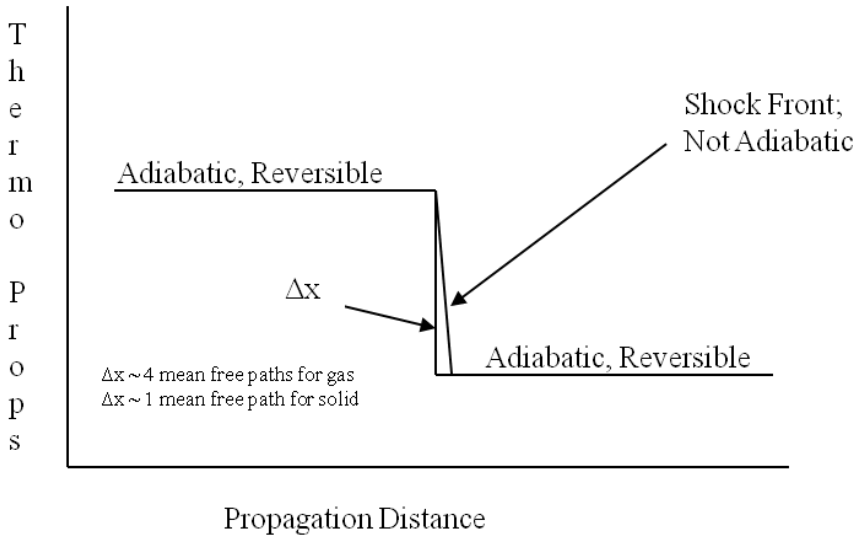

Figure 2.1.2: Shock front thickness is on the order of the molecular mean free path of the medium, i.e. 4x for a gas & 1x for solids [8].

The typical assumption made in hydrocodes is that all processes are adiabatic and isentropic. When these two assumptions are made the 2nd law is not incorporated into the derivation of the governing equations. In relation to a stationary point some finite distance from the shock front the processes are adiabatic because the shock velocity is much greater than the sound speed of the medium. Since conduction occurs at speeds much slower than the speed of sound there is insufficient time for conduction to occur between the shock front and the material immediately behind or in front of the shock. Within the shock front the mechanism that increases the temperature and pressure is momentum transfer and the irreversibilities associated with this process are approximated by heat conduction. In addition, processes away from the shock front are assumed to be reversible, i.e. when unloaded the material returns to its' initial state. Thus, away from the shock front processes are assumed isentropic.

2.2 Hydrocode Formulation

The term hydrocode is used to described a class of computer based numeric formulations which are distinct from more commonly used formulations such as solid material modeling (FEA) or computational fluid dynamics (CFD). In traditional solid material modeling (FEA) the deformation strains are small and the plastic deformation is not necessarily of interest. In addition the strain rates are slow such that an isothermal assumption is sufficient; this is not the case for shock processes in solids. As a result there is typically no need for a formulation, which incorporates a thermodynamic equation of state or even an energy equation. In traditional computational fluid dynamics, which incorporates shock processes, the material strength, the separation of elastic and plastic deformation is ignored. This greatly simplifies the material constitutive relations. In addition most CFD codes assume Newtonian behavior, i.e. linear stress-strain rate behavior as opposed to linear stress-strain behaviors associated with perfectly elastic materials. The word hydro stems from the word hydrodynamic, meaning inviscid fluid behavior; however modern hydrocodes can and do incorporate a variety of stress-strain or strain rate constitutive relations. Thus hydrocodes are a class of computational codes which seek solutions to material deformation problems which must incorporate both thermodynamic and material strength constitutive relations. The following sections outline the equations which describe the hydrodynamic behavior of condensed materials and the codes in which they are encoded: KO and NS.

2.3 Lagragian Formulation: KO

The hydrocode KO formulation described here utilizes the Lagrangian formulation of the conservation equations in a Lagrangian coordinate system in order to numerically resolve the shock interactions in solid materials. The following briefly describes a typical

hydrocode formulation utilized in the modeling of shock processes in condensed matter. A more complete descriptions can be found in Wiklins [9], and Benson [10]. Section 6.2 contains several modifications made to this formulation. The Lagrangian unsteady compressible conservation of mass equation is

$$\frac{D\rho}{Dt} = -\rho \nabla \cdot \vec{V}. \tag{2.3.1}$$

The time rate of change of density for the element is equal to the density multiplied by the velocity gradient per unit volume, because no mass flow is allowed into or out of the material element. The momentum equation is

$$\frac{\rho D\vec{V}}{Dt} = -\nabla \vec{P} + \nabla \cdot \vec{\vec{\sigma}}, \tag{2.3.2}$$

where P is the mechanical pressure and σ is the deviatoric shear distortion. The energy equation is more complicated but it is also reduced by making several assumptions. The assumptions are that there is no nuclear, radiative, electromagnetic, or potential energy in the system. It is also assumed that there is no internal heat or entropy generation, and the effects of gravity and external forces are negligible. Finally it is assumed that the process is adiabatic resulting in the following simplified energy equation

$$\frac{D}{Dt}\left(\rho e + \rho \frac{\vec{V}^2}{2} \right) + \left(\nabla \cdot \vec{P}\vec{V} \right) + \nabla \cdot \left[\vec{\vec{\sigma}} \cdot \vec{V} \right] = 0,$$

$$\dot{E} = \text{ Internal } + \text{ Kinetic } = \text{ Total Energy } = \frac{D}{Dt}\left(\rho e + \rho \frac{\vec{V}^2}{2} \right),$$

$$\dot{E} + \left(\nabla \cdot \vec{P}\vec{V} \right) + \nabla \cdot \left[\vec{\vec{\sigma}} \cdot \vec{V} \right] = 0. \tag{2.3.3}$$

The commonly used stress strain constitutive relationship assumed to be in effect is the one used for consolidated materials, i.e. that the material behaves according to perfectly

elastic-plastic behavior with constant flow stress. Equations (2.3.4) and (2.3.5) describe the stress strain relationships for the principle stress element (σ_{ii}) and the corresponding cross term (σ_{ij}) as functions of pressure (P), bulk modulus (μ), relative volume (V), artificial viscosity (q), and velocity strain (ε);

$$\sigma_{ii} = (-P + q) + 2\mu\left(\varepsilon_{ii} - \frac{1}{3}\frac{\Delta V}{V}\right), \tag{2.3.4a}$$

$$\sigma_{ij} = 2\mu\varepsilon_{ij}. \tag{2.3.4b}$$

This assumption is valid for a large class of brittle and ductile materials as confirmed by one-dimensional experiments that show a square elastic precursor wave ahead of the plastic wave, as illustrated in Fig. 2.1.1. This behavior is simple to model assuming elastic-plastic behavior. The magnitude of the dynamic yield strength can be determined from the experiment by measuring the amplitude of the elastic precursor, i.e. the Hugoniot elastic limit (HEL). The relationship between static and dynamic yield strength can be estimated by equations (2.3.4) and (2.3.5). The elastic precursor travels faster than the plastic wave. However, porous/granular materials such as silica do not show an elastic precursor wave in front of the plastic wave, but if the same material is in a fully consolidated configuration it does show the two-wave structure. Therefore, it is reasonable to assume that the two wave structure is somehow muted by the removal of porosity.

In the elastic-plastic model the mean pressure, P, is defined as $P = (1/3)(\sigma_{xx} + \sigma_{yy} + \sigma_{zz})$, which is the volumetric compression $P = (1/3)(\Delta V/V)$. The principle stress in the element, σ, is defined as $\sigma_{ii} = (-P + q) + s_{ii}$, where q is the artificial viscosity. Along the principle axis the resistance to shear distortion, s, is defined as $s_{ii} = 2\mu(\varepsilon_{ii} - (1/3)(\Delta V/V))$.

The cross terms for stress and distortion are as follows; $\sigma_{ij} = s_{ij}$, where $s_{ij} = 2\mu\varepsilon_{ij}$ where $i \neq j$. Using the continuity equation the relationship between the change in volume and the strain is as follows: $\Delta V/V = \varepsilon_{xx} + \varepsilon_{yy} + \varepsilon_{zz}$. The stress deviators are defined so that they do not contribute to the mean pressure, P.

The material yields plastically whenever stress exceeds the strength of the material. The yield condition allows the material to elastically deform until the elastic limit is reached beyond which point the material flows plastically. If the stress state calculated exceeds the yield strength of the material it would then be outside of the elastic yield surface (Von Mises). The material is brought back onto the yield surface along a path normal to the yield surface. Figure 2.3.1 shows conceptually how this is implemented in the program. The energy associated with the plastic deformation of the material is excluded from the energy equation thereby reducing the available energy. The Von Mises yeild condition is shown in equation (2.3.5).

$$\left(s_1^2 + s_2^2 + s_3^2\right) - \frac{2}{3}(Y^o)^2 \leq K \qquad (2.3.5)$$

If $K \leq 0$ the material is within the elastic limit. If $K > 0$ the multiply the stress deviators by $\sqrt{2/3}Y^o / \sqrt{s_1{}^2 + s_2{}^2 + s_3{}^2}$. Currently, KO calculates plastic energy but subtracts it from the total energy in order to remain on the yield surface. The plastic energy is not continually tracked because temperature is not required in the formulation.

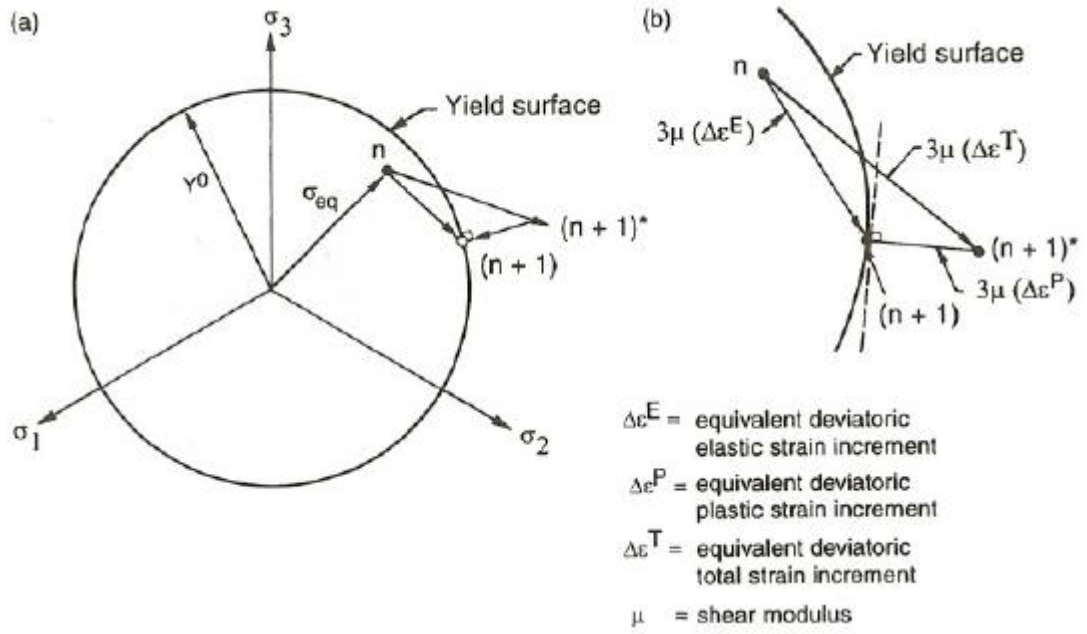

Figure 2.3.1: Von Mises yield condition [9, pg 44]. Figure (a) depicts the yield surface and the three principle axis and figure (b) illustrates how a stress value that exceeds the yield surface is brought back to the surface.

2.3.1 KO Artificial Viscosity Formulation

Artificial viscosity is the way in which irreversibilities are incorporated into hydrocodes. This methodology was first proposed by VonNeumann and Richtymer in 1949 [1]. While the model was proposed for an ideal gas it has been successfully applied to many materials, solids or fluids, and performs several essential functions in modern hydrocodes. It dampens the numerical overshoots behind the shock front, reduces the available energy, and smears the front across multiple cells so that nanoscale resolution is not needed to resolve gradients within the shock front. Although Von Neumann and Richtymer state that the use of artificial viscosity was implemented purely for mathematical reasons the form of it is roughly based on a physical construct, namely Newtonian viscous dissipation of energy within the shock front. A linear term was added

by Landshoff in 1955 [11], which together these form an equation listed below which is the form most often implemented in hydrocode formulation.

$$q = C_o^2 \frac{\rho}{V}\left(\frac{\partial U}{\partial r}\right)^2 (\Delta r)^2 + C_L \frac{\rho a}{V}\left(\frac{\partial U}{\partial r}\right)\Delta r, \tag{2.3.1.1}$$

where q is the artificial viscosity, ρ is the density, C_L and C_O are constants, P is the pressure and a = $\sqrt{P/\rho}$ is the local sound speed of the material and Δr is the local grid spacing parameter. The artificial viscosity, q, is defined as zero for $\partial U/\partial r \geq 0$, because the artificial viscosity is only applied when the velocity gradient is negative and the volume gradient is positive. This insures that the artificial viscosity is only applied during compaction (i.e. a shock) and not during release, which is considered isentropic. A more complete derivation of the governing equations is found in Appendix A. These governing equations provide the basis on which the one-dimensional hydrocode KO is written, and can easily be extended to higher dimensions as in HEMP[9].

The second term, not originally proposed by Von Neumann and Richtymer, was proposed by Landshoff in 1955 [12]. Together the artificial viscosity consists of two shear stress terms: a bulk non-linear and a longitudinal linear term. Both contain gradients in the direction of flow and dependent on the wave speed. The magnitude of the viscous terms contains non-physical parameters, C_L and C_O, which although they represent bulk longitudinal directions they are often set to arbitrary values such as 2 and 1 respectively [1, 2, 9]. C_O determines the number of grid spaces over which the shock front will be spread and is usually set to value of 2 which corresponds to 3 or 5 grid spaces. C_L and C_O can be optimized through trial and error, but if the values are set lower than 2 and 1 respectively the numerical overshoot will increase because the shock front

thickness is being made thinner at which point nanoscale resolution would be necessary to resolve the gradients in the shock front [2].

The applicability of a viscous dissipation term within the shock front is debatable, notwithstanding the idea is that the material is plastically deforming at a constant flow stress. This plastic deformation, which is above the yield strength, is fluidic in nature, even in solids, and as such, viscous dissipation applies. Since the artificial viscosity is only active in the shock front as the material is compressed it serves to relax the isentropic assumption across the shock front and acts as a dissipative term because it reduces the available energy, defined by:

$$\Delta E = -(P+q)\Delta V + \Delta Z. \qquad (2.3.1.2)$$

Here the change in internal energy is equal to the pressure-volume work plus the shear distortion energy ΔZ, which is equivalent to the shear distortion, plastic deformation, work $\nabla \cdot \left[\vec{\vec{\sigma}} \cdot \vec{V} \right]$. Since, the artificial viscosity is only active in compaction when the velocity gradient is negative and the pressure is positive the artificial viscosity reduces the effective pressure, i.e. $P \geq (P+q)$ when q is active in the shock front, and $P = (P+q)$ when q = 0 elsewhere.

2.3.2 KO Discretization

A uniform spatial grid was used to sub divide the material into an even number of cells based on the original material length. In the one-dimensional Lagrangian formulation KO each cell consists of two faces and a cell center. The velocity and position are tracked at the cell faces and all thermodynamic properties are determined at the cell center. A resolution study was conducted on KO and the results indicate that the

optimal number of cells per unit length is 50 cells per millimeter. The grid indices for time and space are denoted as "j" and "n" respectively. Equations (2.3.2.1), (2.3.2.2), and (2.3.2.8) show the one-dimensional, Lagrangian, central difference, discretization of the conservation mass, momentum, and energy. The mass distribution determined by equation (2.3.2.1) is determined at the beginning of the simulation at time zero and remains constant throughout the remainder of the simulation because there is no mass flow into or out of a cell.

$(2.3.2.1)$ Mass zoning

$$m_{j+1} = \frac{\rho_0}{V_0}\left[\left(r_{j+2}^0\right) - \left(r_{j+2}^0\right)\right].$$

$(2.3.2.2)$ Equation of motion

$$U_j^{n+1} = U_j^{n-1} + \frac{\Delta t^n}{\phi_j^n}\left[\left(\sum r\right)_{j+1}^n - \left(\sum r\right)_{j-1}^n\right],$$

where

$$\left(\sum r\right)_{j+1}^n = \left[-\left(P^n + q^{n-1}\right) + s_1^n\right]_{j+1},$$

$$\phi_j^n = \frac{1}{2}\left[\rho_{0\,j+1}\left(\frac{r_{j+2}^n - r_j^n}{V_{j+1}^n}\right) + \rho_{0\,j-1}\left(\frac{r_j^n - r_{j-2}^n}{V_{j-1}^n}\right)\right].$$

While there is no mass flow allowed equation (2.3.2.3) shows the change in relative volume, which is used to determine the density in a given cell. Once the change in relative volume is determined the new position of each cell face is found using the time step and the velocity found using the equation of motion.

$(2.3.2.3)$ Conservation of mass

$$V_{j+1}^{n+2} = \frac{\rho_0}{m_{j+1}}\left[\left(r_{j+2}\right) - \left(r_j\right)\right]^{n+2},$$

$$r_j^{n+2} = r_j^n + U_j^{n+1}\Delta t^{n+1}.$$

Equations (2.3.2.4) and (2.3.2.5) are the velocity strains and stress deviators respectively.

Equations (2.3.2.6) and (2.3.2.7) are the Von Misses yield condition and the artificial viscosity constitutive relation.

$(2.3.2.4)$ Calculation of velocity strains

$$\left(\dot{\varepsilon}_1\right)_{j+1}^{n+1}=\frac{U_{j+2}^{n+1}-U_j^{n+1}}{r_{j+2}^{n+1}-r_j^{n+1}},$$

$$\left(\dot{\varepsilon}_2\right)_{j+1}^{n+1}=\frac{U_{j+2}^{n+1}+U_j^{n+1}}{r_{j+2}^{n+1}+r_j^{n+1}}.$$

$(2.3.2.5)$ Stress deviators

$$\left(s_1\right)_{j+1}^{n+2}=\left(s_1\right)_{j+1}^{n}+2\mu\left[\left(\dot{\varepsilon}_1\right)_{j+1}^{n+1}\Delta t^{n+1}-\frac{1}{3}\left(\frac{V^{n+2}-V^n}{V^{n+1}}\right)_{j+1}\right],$$

$$\left(s_2\right)_{j+1}^{n+2}=\left(s_2\right)_{j+1}^{n}+2\mu\left[\left(\dot{\varepsilon}_2\right)_{j+1}^{n+1}\Delta t^{n+1}-\frac{1}{3}\left(\frac{V^{n+2}-V^n}{V^{n+1}}\right)_{j+1}\right],$$

$$\left(s_3\right)_{j+1}^{n+2}=-\left[\left(s_1\right)_{j+1}^{n+2}+\left(s_2\right)_{j+1}^{n+2}\right].$$

$(2.3.2.6)$ Von Mises yield condition

$$\left(s_1^2+s_2^2+s_3^2\right)-\frac{2}{3}(Y^o)^2=K^{n+2}.$$

$(2.3.2.7)$ Artificial Viscosity

$$q_{j+1}^{n+1}=C_O{}^2\rho_{j+1}^{n+1}\left(U_{j+2}^{n+1}-U_j^{n+1}\right)^2+C_L a\rho_{j+1}^{n+1}\left|U_{j+2}^{n+1}-U_j^{n+1}\right|,$$

where $a=\sqrt{P/\rho},\ C_O=2;C_L=1.$

$(2.3.2.8)$ Energy equations

$$\left(\Delta Z\right)_{j+1}^{n+1}=V_{j+1}^{n+1}\left[s_1\dot{\varepsilon}_1\right]_{j+1}^{n+1}\Delta t^{n+1},\ s_1{}^{n+1}=\frac{1}{2}\left(s_1{}^{n+1}+s_1{}^{n}\right)\text{ etc, }\overline{q}=\frac{1}{2}\left(q^{n+2}+q^{n-1}\right),$$

$$\left(E\right)_{j+1}^{n+2}=\left(\frac{E^n-\left\{\frac{1}{2}\left[\rho_0c^2\left[x+\left(2s-\frac{\gamma_0}{2}\right)x^2+s\left(3s-\gamma_0\right)x^3\right]^n+P^n\right]+\overline{q}\right\}\left[V^{n+2}-V^n\right]+\Delta Z}{1+\frac{1}{2}\left[\gamma_0\right]\left[V^{n+2}-V^n\right]}\right)_{j+1},$$

where $x=1-V$ and V is relative volume.

Equation (2.3.2.9) is the Mie-Grüneisen equation of state that relates pressure to changes in volume and internal energy [14]. The Mie-Grüneisen was originally developed for metals in their fully consolidated form. The Mie-Grüneisen is a summation of two functions; a cold compression function and an internal energy function. The cold compression function, which is an error function, is represented here by a third order polynomial, which assumes pressure is a function of volume change and not temperature. The cold compression error function may also be represented by either a higher order polynomial or a curve fit to its exact solution (experimental data relating pressure to specific volume) as done in the commercial code CTH. The internal energy function relates internal energy to pressure by the gamma parameter. The gamma parameter is experimentally determined and typically a unique value for each material. The gamma parameter can be functionally linked to changes in volume or temperature, however in this work the analysis is simplified by using a singular value available in open literature. By calculating internal energy before pressure and using an old value of pressure to determine the future internal energy value this formulation decouples pressure and energy so that they don't have to be determined simultaneously.

$(2.3.2.9)$ Pressure equation of state

$$P_{j+1}^{n+2} = \rho_0 c^2 \left[\left(1 - V^{n+2}\right) + \left(2s - \frac{\gamma_0}{2} \right) \left(1 - V^{n+2}\right)^2 + s\left(3s - \gamma_0\right)\left(1 - V^{n+2}\right)^3 \right]_{j+1} + \gamma_0 E_{j+1}^{n+2}.$$

These equations form the basis of the KO hydrocode. At the edges, the second order central difference scheme is replaced by second order forward difference or backward difference schemes. The code is staggered in space and time. The code is considered spatially staggered because the velocity and position are determined on the cell faces while the thermodynamic properties are determined at the cell center. The code is

temporally staggered because the velocity, velocity strains, and the artificial viscosity is found at the half time step while relative volume, stress deviators, pressure, and energy are found at the full time step. The KO hydrocode is based on Wilkins one dimensional HEMP formulation [9].

2.4 Eulerian Formulation: NS

The NS hydrocode described here refers to an explicit - second order accurate, finite difference, Eulerian formulation of the Navier-Stockes equations. The use of nanoscale resolution in the NS code facilitates direct resolution of the shock front which eliminates the need to dampen numerical overshoot or oscillations through the artificial viscosity constitutive relation. A brief description of the NS formulation used in this work is presented here. A more complete description can be found in the work of Elizorova [13]. The Navier-Stokes Eulerian formulation for the one-dimensional conservation equations of mass, momentum, and energy are

$$\frac{\partial \rho}{\partial t} + \frac{\partial j}{\partial x} = 0, \tag{2.4.1}$$

$$\frac{\partial (\rho u)}{\partial t} + \frac{\partial (ju)}{\partial x} + \frac{\partial P}{\partial x} = \frac{\partial \Pi_{xx}}{\partial x}, \tag{2.4.2}$$

$$\frac{\partial E}{\partial t} + \frac{\partial (jH)}{\partial x} + \frac{\partial q}{\partial x} = \frac{\partial (\Pi_{xx} u)}{\partial x}. \tag{2.4.3}$$

In equation (2.4.1) ρ is the density, t is time, j is the mass flux density vector ($j = \rho u$), x is the spatial dimension, and u is the particle velocity. Equation (2.4.2) is the conservation of momentum equation and includes the normal stress denoted by $\partial P / \partial x$, and the shear-stress tensor using Stokes assumption is Π_{xx}, where $\Pi_{xx} = 4/3\, \mu \partial u / \partial x$. Stokes assumption will be relaxed when implementing the Navie-Stokes equations in

liquids and solids. The enthalpy in equation (2.4.3), is defined in the usual way, H = (E + P)/ρ; and q refers to the heat flux vector, where Fourier heat flux is assumed: $q = -\kappa \partial T / \partial x$. The viscosity, μ, and the thermal conductivity, κ, in a perfect gas are determined by the following equations $\mu = \mu_\infty (T/T_\infty)^w$ and $\kappa = \gamma R \mu / [(\gamma - 1)\Pr]$ where μ_∞ and T_∞ are the viscosity and temperature of the far field upstream of the shock. The Prandtl number is denoted by Pr, and γ is the ratio of specific heats.

2.4.1 NS Discretization

A uniform spatial grid was used to sub divide the domain. The grid was always chosen to be much less than the anticipated shock thickness for added numeric stability. The time step, which satisfied the Courant Stability Criterian, used in the process was directly linked to the spatial step insuring maximum stability and removing the need for artificial dissipation. In an effort to minimize the appearance of steep gradients and in order to compare different materials at different initial conditions, the code was nondimensionalized. The variables with the "*" symbol are the dimensional variables while the "∞" variables refers to the upstream conditions in the far field, such as temperature, density, and sound speed, and the "i" terms are the dimensionless quantities. In the NS formulation q and s refer to heat conduction and entropy respectively, as opposed to the KO formulation where q and s represented artificial viscosity and stress deviators.

$$T_i = \frac{T_i^*}{T_\infty}, \tag{2.4.1.1}$$

$$\rho_i = \frac{\rho_i^*}{\rho_\infty}, \tag{2.4.1.2}$$

$$P_i = \frac{P_i^*}{\rho_\infty \cdot C_\infty \cdot C_\infty}, \tag{2.4.1.3}$$

$$u_i = \frac{u_i^*}{C_\infty}, \tag{2.4.1.4}$$

$$E_i = \frac{E_i^*}{\rho_\infty \cdot C_\infty \cdot C_\infty}, \tag{2.4.1.5}$$

$$\mu_i = \frac{\mu_i^*}{\rho_\infty \cdot C_\infty \cdot \lambda}. \tag{2.4.1.6}$$

The time derivatives were approximated using an explicit first order forward difference method. The spatial derivatives were approximated with a second order central or upwind/downwind stencil on a staggered mesh. The Navier-Stokes equations, applicable to an ideal gas, rewritten in nondimensional finite difference form are:

$$\hat{\rho}_i = \rho_i - \frac{h_t}{h_x}\left(j_{i+1} - j_{i-1}\right), \tag{2.4.1.7}$$

$$\hat{u}_i = \left[\rho_i u_i + \frac{h_t}{h_x}\left[\left(\Pi_{i+1} - \Pi_{i-1}\right) - \left(j_{i+1}u_{i+1} - j_{i-1}u_{i-1}\right) - \left(P_{i+1} - P_{i-1}\right)\right]\right] / \hat{\rho}_i, \tag{2.4.1.8}$$

$$\hat{E}_i = E_i + \frac{h_t}{h_x}\left[\left(\Pi_{i+1}u_{i+1} - \Pi_{i-1}u_{i-1}\right) - \left(j_{i+1}H_{i+1} - j_{i-1}H_{i-1}\right) - \left(q_{i+1} - q_{i-1}\right)\right], \tag{2.4.1.9}$$

$$\hat{P}_i = \left(\gamma - 1\right)\left[\hat{E}_i - \hat{\rho}_i(\hat{u}_i)^2 / 2\right], \tag{2.4.1.10}$$

$$T_i = \gamma P_i / \rho_i. \tag{2.4.1.11}$$

These five equations describe the cell centered system in terms of dimensionless pressure, energy, temperature, density, and velocity. The shear-stress tensor and the heat flux vector in nondimensional finite difference form are:

$$\Pi_{i+1} = \frac{4}{3}\left(\frac{1}{2}\left(\eta_{i+2} + \eta_i\right)\right)\left(\frac{u_{i+2} - u_i}{h_x}\right), \tag{2.4.1.12}$$

$$q_{i+1} = -\frac{1}{(\gamma-1)\mathrm{Pr}}\left(\frac{1}{2}(\eta_{i+2}+\eta_i)\right)\left(\frac{T_{i+2}-T_i}{h_x}\right). \quad (2.4.1.13)$$

The cell face values are found by averaging:

$$j_{i+1} = (\rho_{i+2}u_{i+2} - \rho_i u_i)/2, \quad (2.4.1.14)$$

$$\rho_{i+1} = (\rho_{i+2} - \rho_i)/2, \quad (2.4.1.15)$$

$$u_{i+1} = (u_{i+2} - u_i)/2, \quad (2.4.1.16)$$

$$P_{i+1} = (P_{i+2} - P_i)/2, \quad (2.4.1.17)$$

$$E_{i+1} = (E_{i+2} - E_i)/2, \quad (2.4.1.18)$$

$$H_{i+1} = (E_{i+1} + P_{i+1})/\rho_{i+1}. \quad (2.4.1.19)$$

The next set of equations shows how variables are put into dimensional form;

$T_i^* = T_i \cdot T_\infty$ units of [K],
$\rho_i^* = \rho_i \cdot \rho_\infty$ units of [Kg/m^3],
$P_i^* = P_i \cdot \rho_\infty \cdot C_\infty \cdot C_\infty$ units of [N/m^2],
$u_i^* = u_i \cdot \sqrt{(\gamma \cdot R_\infty \cdot T_i)}$ units of [m/s],
$E_i^* = E_i \cdot \rho_\infty \cdot C_\infty \cdot C_\infty$ units of [N/m^2],
$\eta_{\mathrm{i}}^* = \eta_i \cdot \rho_\infty \cdot C_\infty \cdot \lambda$ units of [Kg/m$\cdot$s],
$\Pi_i^* = \Pi_i \cdot \rho_\infty \cdot C_\infty \cdot C_\infty$ units of [N/m^2],
$q_i^* = q_i \cdot \rho_\infty \cdot C_\infty \cdot C_\infty \cdot C_\infty$ units of [Kg/s^3],
$\Delta s^* = \Delta s \cdot C_\infty \cdot C_\infty / T_\infty$ units of [J/Kg$\cdot$K].

To obtain the entropy generated within the shock front we integrate across the shock front using the following integral form:

$$\Delta s = \int \frac{\vec{\Pi}}{T}\frac{du_x}{dx}dx - \int \frac{1}{T}\frac{d\vec{q}}{dx}dx. \quad (2.4.1.20)$$

The entropy production values obtained with this formulation were compared to the analytic formulation for the change in entropy for an ideal gas.

Chapter 3

Problem Description

3.1 Compaction of Porous/Granular Materials

The dynamic compaction of porous/granular material research is relevant to many applications including but not limited to; blast protection (armored vehicles), tectonic plate movement (earthquakes), and debris colliding with space shuttle, powder metallurgy and powder manufacturing. The mechanism by which distended (porous/granular) materials are crushed and eventually consolidated is not well understood from the perspective of classic strength of material models. The purpose of this work is to directly model the irreversible process by which a porous/granular material is consolidated by shock loading using viscous dissipation and heat transfer as a guide to suggest improvement to current formulations.

Typically, in hydrocodes irreversibility is accounted for through the inclusion of an artificial viscosity model, and the unrecoverable work expended to plastically deform the material. Artificial viscosity operates only in the shock front during compression and relates the sound speed of a material to its pressure and density. Even though artificial viscosity is based on a physical construct, the sound speed of the material, it is rate dependent and contains non physical parameters. This work seeks to replace the artificial viscosity model with an entropy model derived from fundamental principles of thermodynamics.

The inclusion of entropy into the hydrocode should make the formulation more dissipative by reducing the availability energy that can be transmitted with the shock. Entropy reduces the available energy via the mechanisms of heat conduction and viscous dissipation. This energy loss should be coupled with the energy loss associated with plastic deformation. The energy associated with plastic deformation is thought to be retained in the material as heat and contributes to the residual internal energy, which is substantially higher for a distended material as compared to a fully consolidated material given the same loading conditions. With entropy and temperature included the formulation is now thermodynamically complete and the primary energy sources and sinks are now properly accounted for. Accurate accounting of the available energy should lead to improvements in predicting the peak temperature, internal energy, and pressure in porous/granular materials.

Hydrocodes require an equation of state for system closure and one of the equations of state used in this work, the Mie-Grüneisen [14], relates pressure to internal energy and volume. While this equation of state works well for fully consolidated materials it does not perform as well for porous/granular materials. Furthermore, it is thermodynamically incomplete, because it does not contain information regarding the temperature or entropy. Details concerning this particular equation of state are presented in the subsequent chapters.

Chapter 4

KO Analysis

4.1 Introduction

This investigation started by implementing and investigating the Mie-Grüneisen equation of state in the KO hydrocode. Initial simulations were unable to successfully simulate the dynamic compaction of extremely porous silica (density near 0.1 g/cc). The program would experience cell volume collapse and shut down. This was unexpected since, the program was able to simulate the dynamic compaction of a fully consolidated material.

4.2 Flyer Plate Experiments

In order to better understand the simulations presented below, this section presents a short review of one-dimensional (plain strain) shock experiments. One-dimensional shock experiments are impact experiments that are designed to launch a plane shock wave into a material of interest. The material of interest, the target, is usually sandwiched between two plates, an impact or front plate and back plate, both of which have a known response curve called the Hugoniot. The Hugoniot describes the material response to shock loading and relates impact speed to shock wave speed. The flyer plate is the plate launched towards the impact plate at a specified velocity. In most instances, the impact plate is made up of the same material as the flyer plate.

Since the Hugoniot is known for all materials except the material of interest a technique called impedance matching [15] can be employed, which determines the shock speed and the particle speed, and stress and/or pressure of the shock launched into the material. This technique is only valid so long as the wave front remains planar, i.e. one-dimensional wave behavior. The experimental dimensions are set to make the shock wave measured by the gages one-dimensional. This is done by making the samples used large enough that the three-dimensional shock wave launched into the material on impact is reduced to one-dimension initially. Eventually, reflected waves come in from the sides and obscure the measurements, but that happens later in time. Manganin gages [16, 17] are embedded inside the material of known response or placed on the front or back of the material of interest to measure the stress and time of arrival for the shock, which can be used to establish the shock velocity. Below in Figure 4.2.1 is a picture of a typical gas gun used in one-dimensional shock experiments [18].

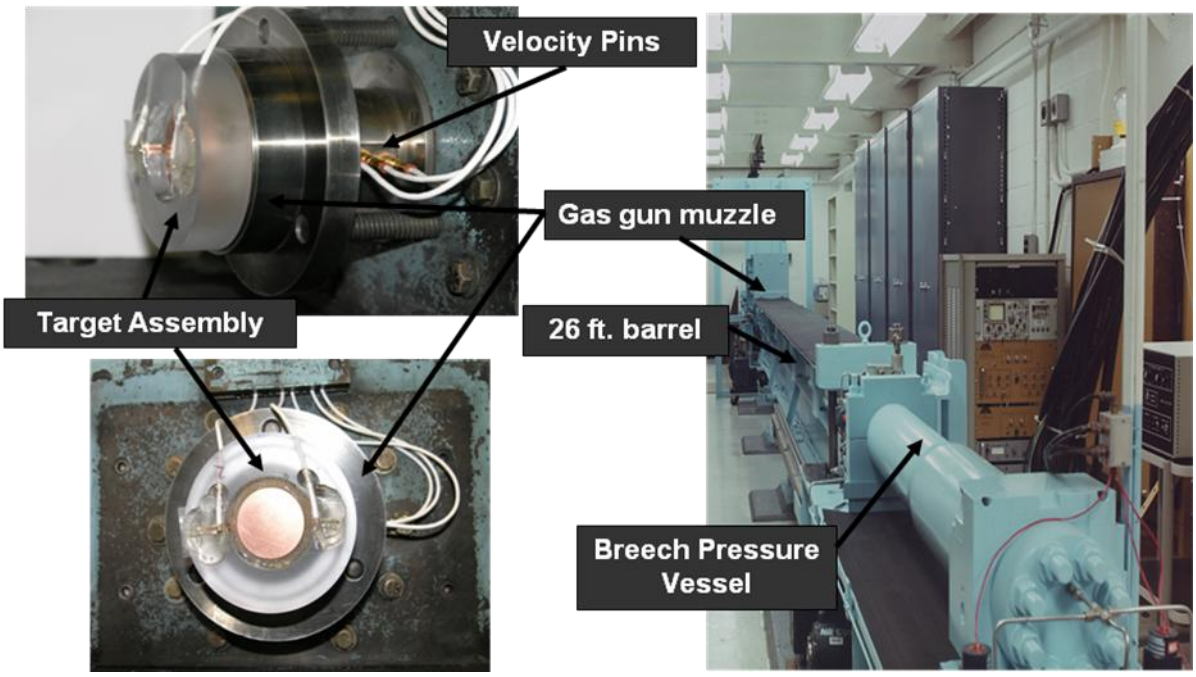

Figure 4.2.1: Gas Gun Facility at the Naval Surface Warfare Center, Dahlgren Division (NSWCDD). The gun muzzle, barrel, breech pressure vessel, velocity pins and target assembly are shown.

The picture in Fig. 4.2.1 is of the gas gun facility at the Naval Surface Warfare Center, Dahlgren Division (NSWCDD) [18]. Gas guns use high pressure gas to launch flyer plates at desired velocity towards the target. Figure 4.2.2 is a schematic of a typical setup [18,19].

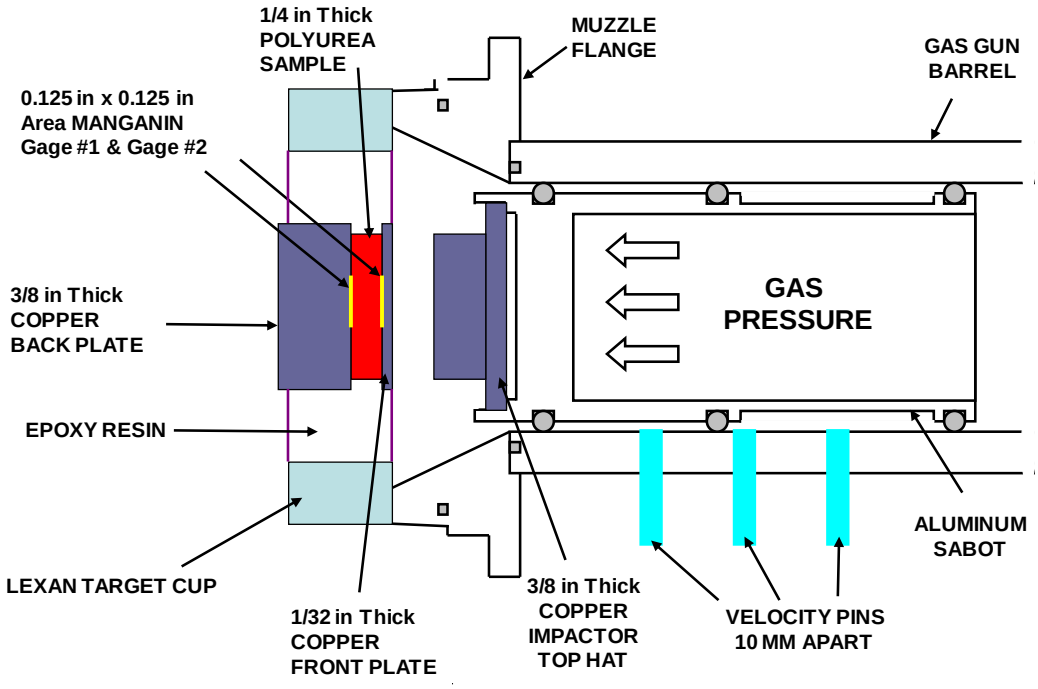

Figure 4.2.2: Schematic for One-Dimensional Hugoniot Experiments as implemented at NSWCDD.

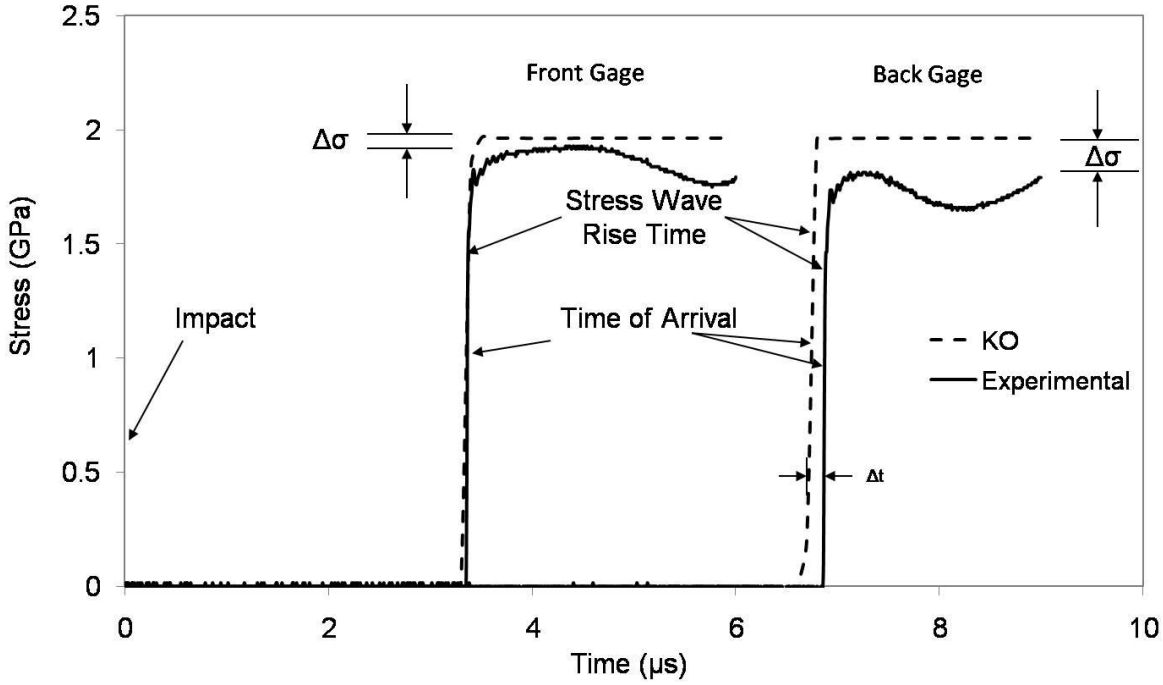

Figure 4.2.3: Copper impacting a section of PMMA sandwiched between a copper impact plate and a copper back plate. The impact speed was 555 m/s. The symbol Δσ represent the difference in peak stress between the experimental pressure signature and predicted pressure signature using the hydrocode KO.

Figure 4.2.3 presents a typical series of time traces obtained from a flyer plate experiment. The geometry for this experiment is a section of Polymethyl-mehacrylate (PMMA) sandwiched between two copper plates impacted by a copper plate at a speed of 555 m/s. Figure 4.3 presents data obtained from two Manganin gauges, one placed in front of the PMMA target plate and the other behind the target plate along with the KO simulation. Figure 4.3 demonstrates that the KO program adequately simulates the dynamic compaction of fully consolidated materials. The results seen here are comparable to the results obtained from commercially available hydrocodes. As seen in Fig. 4.2.3 the code successfully predicts wave features both qualitatively and quantitatively. There is only a slight overshoot in the peak stress and a small deviation in

the arrival time for shock wave at the back gage. These features demonstrate that the KO code captures the underlying physics of the phenomena. In Fig 4.2.3 it should be noted that the material is not displaying classic two wave structure, i.e. PMMA is not behaving like a perfectly elastic-plastic material with an elastic precursor wave in front of a plastic wave, even though the stress reported by the two gages are above the HEL (Hugoniot Elastic Limit) of 0.75 GPa reported in literature [20]. PMMA is a polymer and despite not using a polymer specific strength of material model the hydrocode KO does an adequate job predicting the shock response of the material under the specified loading conditions.

Figure 4.2.4 shows how the code fails to qualitatively or quantitatively model the dynamic compaction of the porous/granular material Silica. Figure 4.2.4 compares one-dimensional (plain strain) experimental results to the KO results for the dynamic compaction of silica with a density of 0.1 g/cm^3. These results demonstrate the modeling limitations of the hydrocode KO, i.e. KO fails to adequately model porous/granular materials.

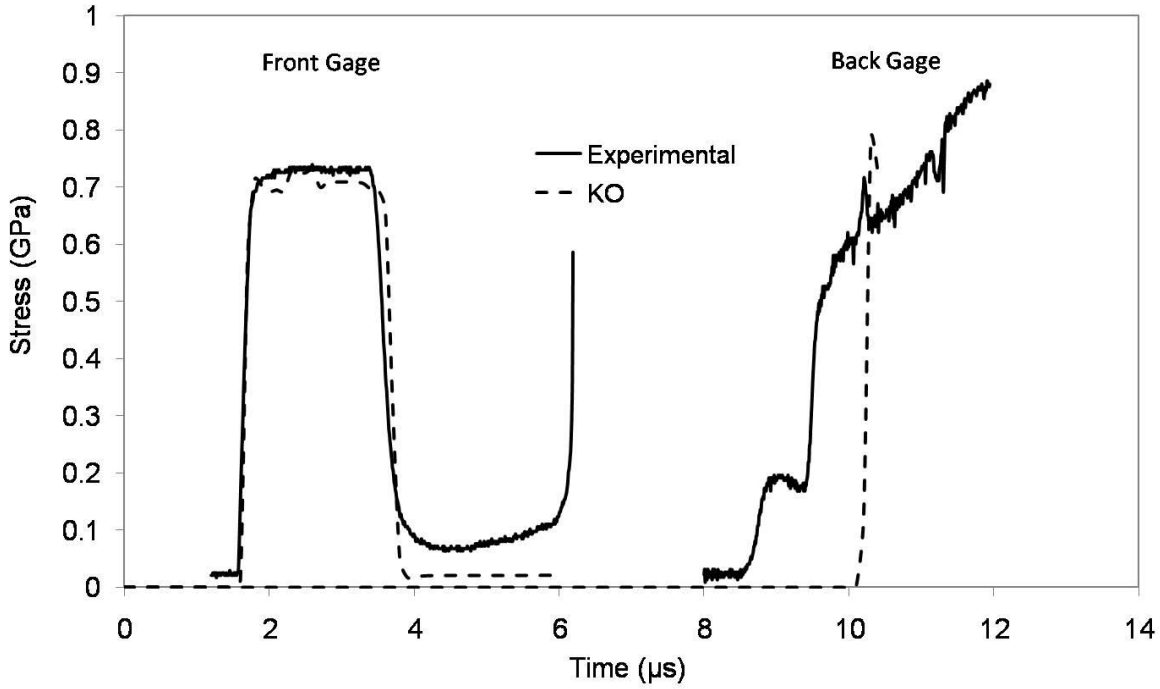

Figure 4.2.4: Silica, density of 0.1 g/cm^3, sandwiched between two PMMA, density of 1.2 g/cm^3, plates and impacted by a PMMA flyer plate at 405 m/s.

As seen in Fig. 4.2.4 the time of arrival and the peak stress on the back gage are poor predictions when compared to the gage data. We interpret these discrepancies as indicators that the equation of state modeling the underlying physics of the dynamic compaction of porous/granular materials is deficient. This initial modeling effort seemed to indicate that the failure to adequately model the dynamic compaction of porous/granular materials was due to the fact that the consolidation process, where void spaces are removed, occurs on a scale associated with the meso/grain or particle size and not on a bulk material scale, which is the underlying formulation for the code KO. This interpretation of the modeling results lead to the conclusion that only direct simulation of grain level dynamics could resolve the modeling inadequacies, because it is here on a mesoscale were the grains experience fractures, morphology, friction heating, and jetting.

Subsequent modeling efforts altered this point of view when it was found that a commercially available code, CTH [21], was able to produce results without crashing using the same equation of state, the Mie-Grüneisen, and the same input parameters as KO. Initial efforts to resolve this difference between the code used in this work, KO, and CTH revolved around using sub-iteration to simultaneously solve the energy and the Mie-Grüneisen equation of state, and grid refinement to reduce mesh deformation. These efforts failed to improve the original KO results, therefore it was concluded that the implementation of the Mie-Grüneisen equation of state was the source of the problem.

Chapter 5

Equation of State Development

5.1 Review of Mie-Grüneisen Equation of State

The Mie-Grüneisen equation of state has a long history of successful implementation and works well for consolidated materials experiencing moderate strain levels. The Mie-Grüneisen model [14] assumes that the total pressure and internal energy of a solid are function of the cold energy and pressure, thermal energy and pressure, and the electronic energy and pressure [22].

$$E_{Total} = E_c + E_t + E_e \tag{5.1.1}$$

$$P_{Total} = P_c + P_t + P_e \tag{5.1.2}$$

The subscript "-c-" refers to the cold energy and pressure which describes the compression of the material at 0 K. The cold pressure and energy, which only represents the lattice compaction, are functions of density only and independent of temperature. The subscript "-t-" refers to the thermal pressure and energy, which is caused by the motion of atoms. The subscript "-r-" refers to the electronic pressure and energy and is caused by the thermal excitation of electrons. Since the electronic energy and pressure is only important at temperatures above 10,000 K it is excluded from the derivation of the Mie-Grüneisen model [14].

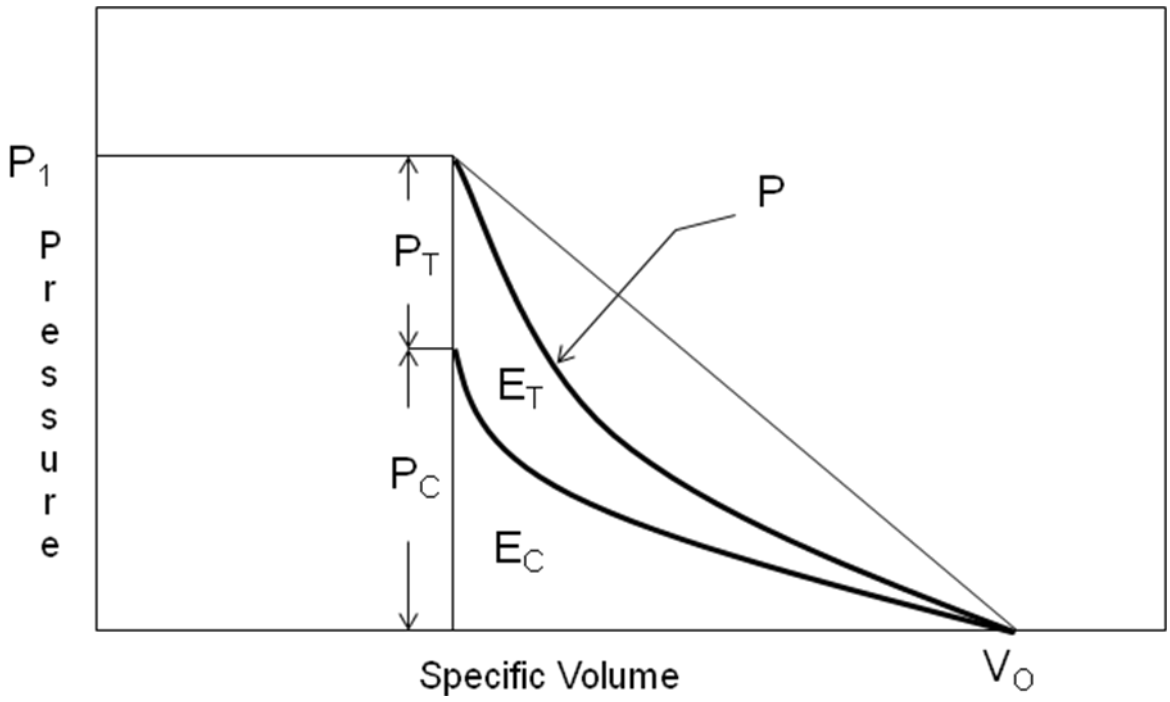

Figure 5.1.1: Mie-Grüneisen model [14] assumes that the total pressure in a material is only a function of the thermal pressure and cold pressure.

The basic formulation of the the Mie-Grüneisen EOS is statistically based. The formulation proceeds by selecting a partition function describing the distribution of energy to represent the thermal contribution and an error function to represent the lattice compaction [9, 23].

The resulting analysis yields a simple EOS which is applicable on a bulk material scale. The Mie-Grüneisen model [14] with the cold curve as the reference state, is

$$P(V,T) - P(V,0) = \frac{\gamma(V)}{V}[E(V,T) - E(V,0)], \tag{5.1.3}$$

where P is the pressure, V is the volume, E is the internal energy, and γ is the Grüneisen parameter [9, 24]. This derivation uses the convention that $E(V_0, 0) = 0$, i.e. the internal energy is zero at a temperature of 0 K. Therefore equation (5.1.3), using the Hugoniot (locus of all possible end states) as the reference curve, may be rewritten as

$$P_H(V) - P(V,0) = \frac{\gamma(V)}{V}[E_H(V) - E(V,0)]. \tag{5.1.4}$$

In equation (5.1.4) the unknown state, the cold curve, is determined from the known reference state, the Hugoniot. Assuming a linear relationship between the shock velocity, U_s, and the particle speed, U_p, and using the Rankine-Hugoniot equations (i.e. the jump conditions) [9, 24],

$$P_H(V) = \rho_0 U_S U_P, \text{ and } \frac{V}{V_0} = 1 - \frac{U_P}{U_S} \tag{5.1.5}$$

$$U_s = c + sU_p, \text{ and } P_H(V) = \frac{\rho_0 c^2 x}{(1-sx)^2}, \tag{5.1.6}$$

$$E_H(V) = \frac{P_H V_0 x}{2}, \text{ and } \gamma(V) = \frac{\gamma_0 V}{V_0}, \tag{5.1.7}$$

where $x = 1 - V/V_0$ and the subscript zero refers to quantities on the undisturbed material properties. In addition we define the cold pressure as the change in the cold (minimal) internal energy with respect to volume at 0 K [9, 24]

$$P(V,0) = P_0(V) = -\frac{\partial E_0}{\partial V}. \tag{5.1.8}$$

After inserting equations (5.1.5) - (5.1.8) into equation (5.1.4) and collecting terms we obtain a 1st order differential equation for the cold curve energy, $E_0(V)$ [9, 24]

$$-\frac{\partial E_0}{\partial V} = \frac{\gamma_0}{V_0} E_0 + \frac{\rho_0 c^2 x}{(1-sx)^2}\left(1 - \frac{\gamma_0}{2} x\right). \tag{5.1.9}$$

The exact solution of equation (5.1.9) yields an error function, the zero-Kelvin energy equation (5.1.10), which is problematic for implementation into computer codes.

$$E_0(V) = \int_0^x \gamma_0 E_0(V,0) + \frac{c^2 x}{(1-sx)^2}\left(1 - \frac{\gamma_0 x}{2}\right) dx \tag{5.1.10}$$

To avoid the use of an error function, a power series solution was assumed in x. It is typical that a 3rd order power series solution is utilized which works well for fully consolidated materials. However, it fails to produce adequate results when applied to porous/granular materials as will be shown here. Extending the power series solution in *x* to a 6th order polynomial results in the cold curve energy $E_0(V)$ having the following form and coefficients

$$
\begin{aligned}
&E_0(V) = E_{00} + E_{01}x + E_{02}x^2 + E_{03}x^3 + E_{04}x^4 + E_{05}x^5 + E_{06}x^6, \\
&E_{00} = E_{01} = 0, E_{02} = \frac{1}{2}(c^2 + {\gamma_0}^2 E_{00}), \\
&E_{03} = \frac{1}{6}(4sc^2 + {\gamma_0}^3 E_{00}), \\
&E_{04} = \frac{1}{24}(-2\gamma_0 sc^2 + 18s^2c^2 + {\gamma_0}^4 E_{00}), \\
&E_{05} = \frac{1}{120}(-18\gamma_0 s^2c^2 + 96s^3c^2 - 2{\gamma_0}^2 sc^2), \\
&E_{06} = \frac{1}{360}(300s^4c^2 - 72\gamma_0 s^3c^2 - 9{\gamma_0}^2 s^2c^2 - {\gamma_0}^3 sc^2).
\end{aligned}
\tag{5.1.11}
$$

The pressure can be obtained from equation (5.1.8), thus the cold pressure solution has the same order as the cold energy solution. Solving the Mie-Grüneisen equation for the Hugoniot pressure we obtain

$$P_H(V) = P_0(V) + \frac{\gamma_0}{V_0}[E_H(V) - E_0(V)]. \tag{5.1.12}$$

Inserting equations (5.1.6)-(5.1.8) and (5.1.11) into (5.1.12), we obtain pressure as a function of strain, $x = 1 - V/V_0$, and internal energy

$$
\begin{aligned}
&P_H(V,E) = k_1 x + k_2 x^2 + k_3 x^3 + k_4 x^4 + k_5 x^5 + k_6 x^6 + \gamma_0 E, \\
&k_1 = \rho_0 c^2, \\
&k_2 = (2s - \frac{\gamma_0}{2})\rho_0 c^2, \\
&k_3 = (3s^2 - \gamma_0 s)\rho_0 c^2, \\
&k_4 = (4s^3 - \frac{3}{2}\gamma_0 s^2)\rho_0 c^2, \\
&k_5 = (5s^4 - 2\gamma_0 s^3)\rho_0 c^2, \\
&k_6 = (-\frac{5}{6}\gamma_0 s^4 + \frac{1}{5}{\gamma_0}^2 s^3 + \frac{1}{40}{\gamma_0}^3 s^2 + \frac{1}{360}{\gamma_0}^4 s)\rho_0 c^2.
\end{aligned}
\tag{5.1.13}
$$

For consolidated materials experiencing strains less that 10%, there is little difference between the exact solution for the cold curve, equation (5.1.10), and a 3rd through 6th order polynomial solution. The internal energy for the exact solution and the power series solution approach infinity as strain increases as seen in Fig. 5.1.2.

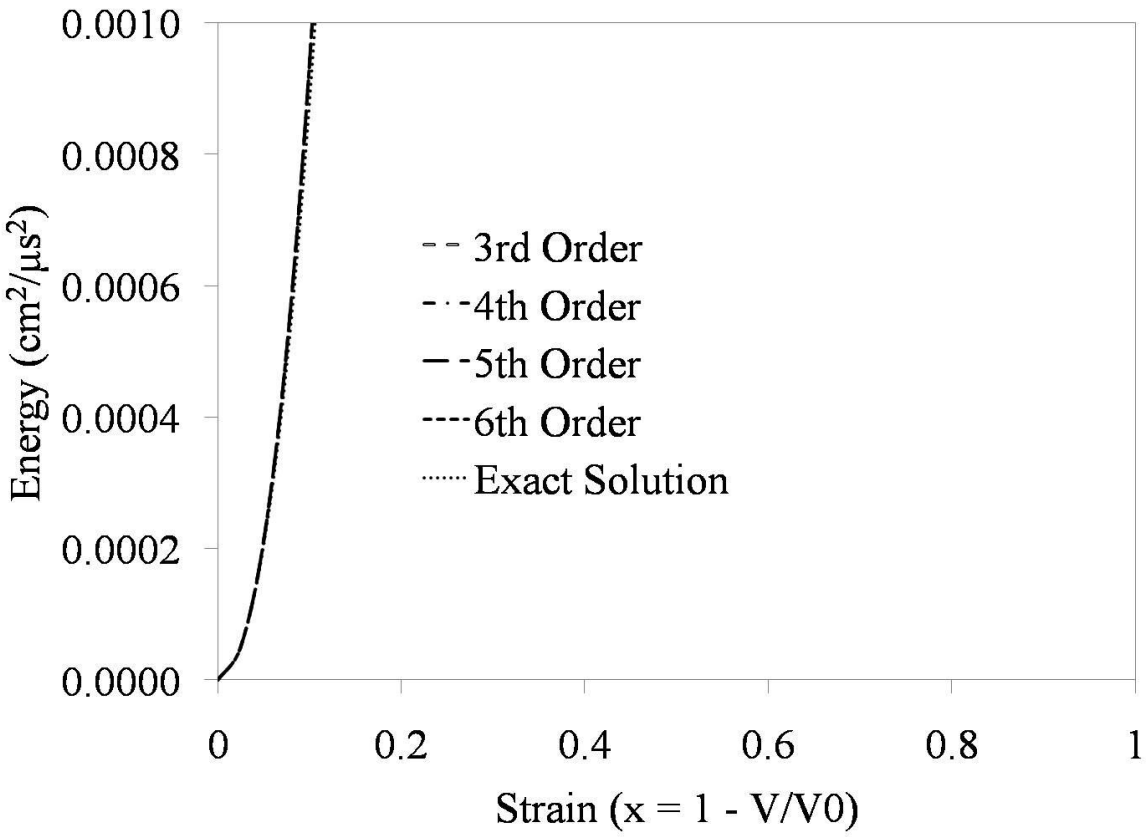

Figure 5.1.2: Cold Curve for Copper with ρ_0 = 8.93 g/cc, s = 1.49, c = 0.49 cm/μs, and γ_0 = 1.99 [9].

While strains less than 10% are common place in shock and ballistic problems for consolidated materials, this is not the case for extremely porous granular materials. In these cases it is critically important to accurately reproduce the exact error function solution for the cold curve at higher strains because porous granular materials experience greater deformation and strain than that experienced by consolidated materials under the same loading conditions. As can be seen in Fig. 5.1.3, the power series solutions begin to deviate noticeably from the exact solution at 60% strain.

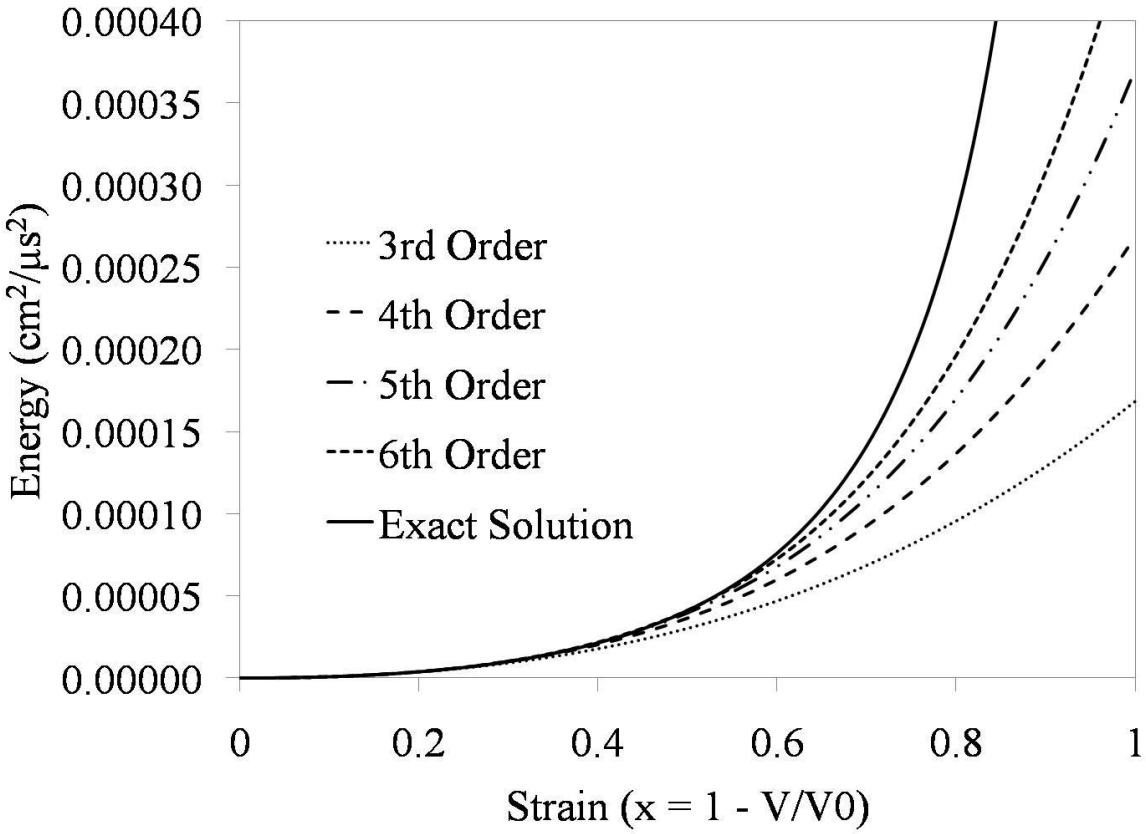

Figure 5.1.3: Cold curve for porous silica with ρ_0 = 0.10 g/cc, s = 0.9736, c = 0.0121 cm/μs, and γ_0 = 0.3 [9].

These various representations of the cold curve were implemented as part of the Mie-Grüneisen equation of state in KO [9].

For the data of interest here, namely highly porous silica powder, the expectation is that there will be large strains in the silica powder as it is compacted. Hugoniot and pressure-time data was obtained for initial densities of 0.77 g/cc, 0.25 g/cc, and 0.10 g/cc porous silica from the Cavendish Laboratory, University of Cambridge [9, 25]. Utilizing a 3rd order representation of the cold curve within KO failed because computational cell volumes went to zero. The code would fail at the first silica cell because the internal energy and pressure in the cell would not increase enough to resist the reduction in volume required by the shock front. By adding higher order terms to the cold curve, the

response is effectively stiffened, as illustrated in Figure 5.1.3. Thus the operational capabilities of KO were increased so that shock waves in silica powders with initial densities as low as 0.1 g/cc could be resolved. One should bear in mind how low an initial solid density of 0.1 g/cc is; air has a density of 1.2 g/cc.

Figure 5.1.4 presents a pressure-time signature of 0.1 g/cc silica powder obtained from two manganin gages, placed near the front and back side of the powder respectively. For a complete description of the experiment and data set see Borg, *et.al.* [9, 25]. The experimental data is compared to two numeric simulations: CTH [21] and KO [9]. When comparing these results it is of interest to note that the Mie-Grüneisen formulation implemented in CTH is a 5^{th} order polynomial fit to the exact solution for the cold curve, equation (5.1.10) [26].

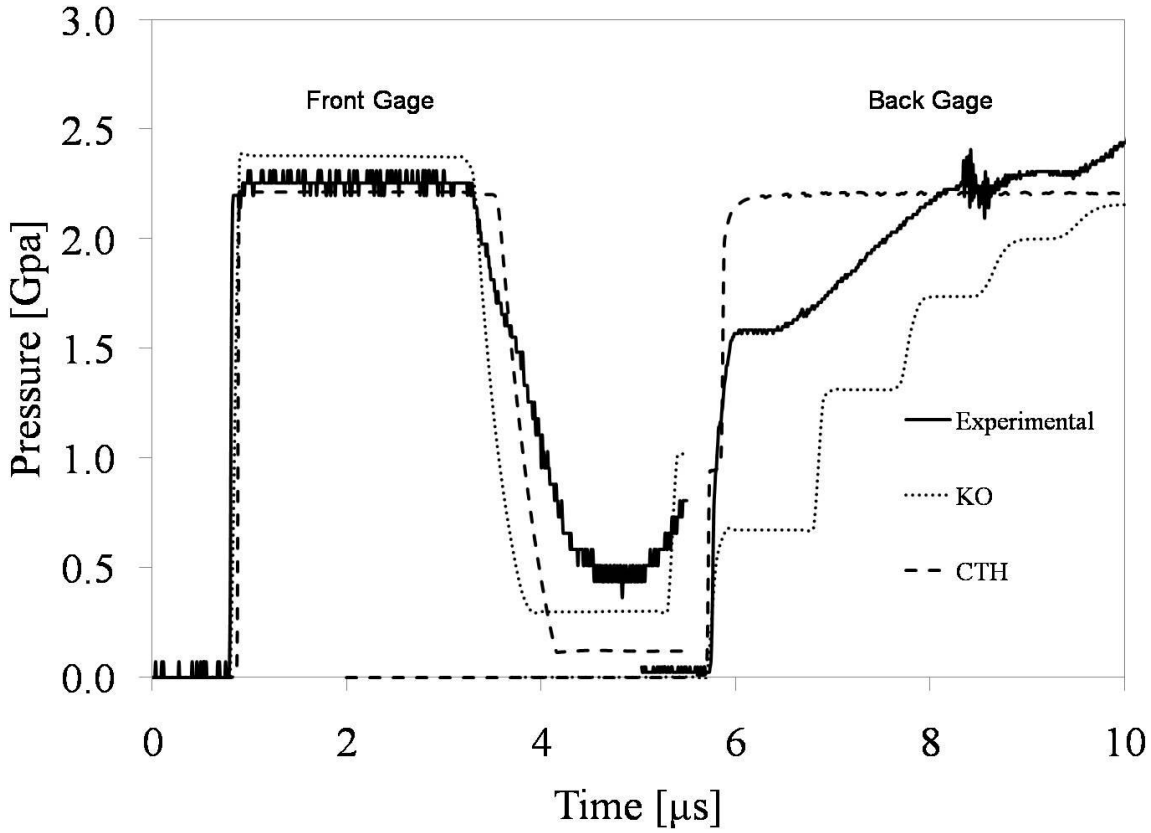

Figure 5.1.4: Experimentally obtained pressure signatures of 0.10 g/cc porous silica at an impact speed of 1100 m/s compared to CTH and KO.

Several interesting features of these two experimental signatures as well as the resulting simulations can be observed. First, the Hugoniot strain, $x = 1 - V/V_0$, in the powder is approximately $x = 0.97$. Thus, when comparing this strain to Fig. 5.1.3, one can observe that the order of the cold curve representation will be critical. Second, the experimental data indicates a rise in the front gage near 5 μs. It is unknown whether this is an artifact of the gage or an actual variation in the pressure. Thus the use of Manganin gages in this extreme application is not well characterized. If the gage results are to be believed, this rise, which appears after the initial one-dimensional compaction wave, would indicate unsteadiness in the thermodynamic state of the powder. Although CTH indicates this feature should not be present in the signature, KO does predict a rise in

stress. Third, the back gage indicates that the transmitted stress signature rises near 6 μs, plateaus near a stress of 1.6 GPa, and then slowly rises to near 2.25 GPa at approximately 7 μs. The CTH simulation immediately rises to 2.25 GPa, over-predicting these pressure signature features. The KO simulation, however, under-predicts these features but exhibits re-shock like behavior more closely resembling the experimental signature, and eventually asymptoting to 2.25 GPa.

The results in Fig. 5.1.4 are consistent with other initial densities of the porous silica at high impact speeds, and these results are shown in Fig. 5.1.5 and Fig. 5.1.6. The existence of these features in the experimental data, as well as the discrepancy between CTH and KO, motivate the current work.

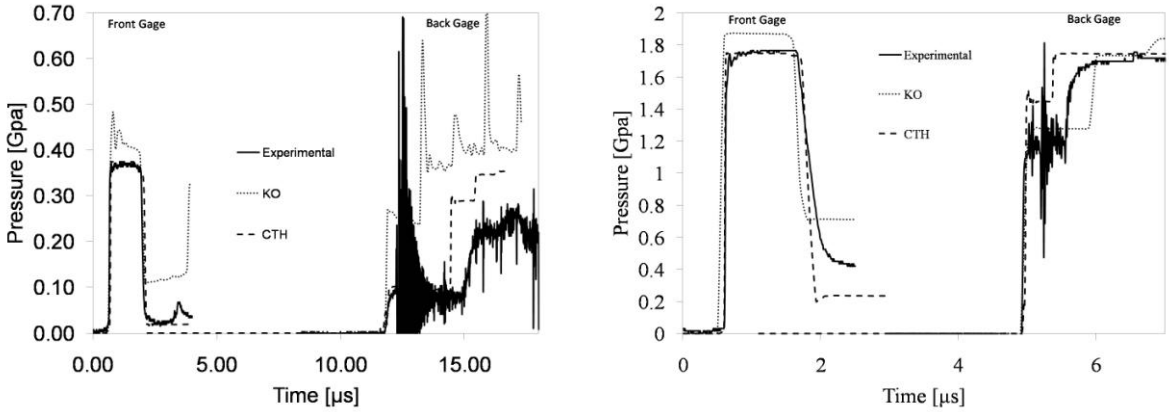

Figure 5.1.5: Experimentally obtained pressure signatures of 0.25 g/cc porous silica at impact speeds of 900 m/s (left) and 220 m/s (right) compared to CTH and KO.

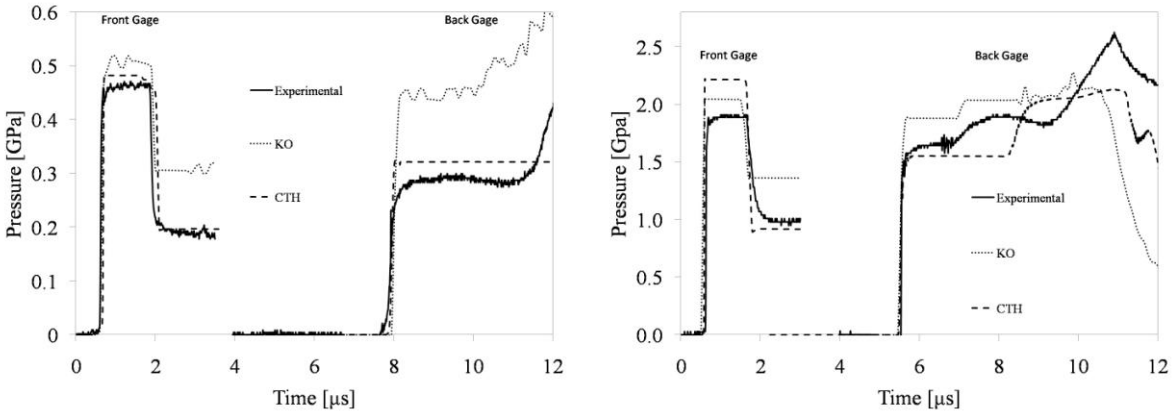

Figure 5.1.6: Experimentally obtained pressure signatures of 0.77 g/cc porous silica at impact speeds of 280 m/s (left) and 970 m/s (right) compared to CTH and KO.

This work indicates that higher order representations of the cold curve are necessary when applying the Mie-Grüneisen equation of state to extremely porous granular materials. These additional terms are necessary if the numeric representation of the cold curve deviates significantly from the exact cold curve solution, i.e. the error function of equation (5.1.10). For the given experimental data, the KO simulations indicate that a 6^{th} order formulation over-predicts the stress at low particle velocity, while under-predicting the stress at high particle velocity. Coding the error function would involve numerically integrating the 1^{st} order differential equation for $E_0(V)$, equation (5.1.10) and fitting a polynomial of sufficient order through the resulting solution to obtain a better representation of the exact solution [26]. This could result in a better representation of the cold curve and a more accurate simulation of the experimental data.

These results indicate that the Mie-Grüneisen equation of state performs adequately when applied to porous/granular materials if the cold curve representation is done properly, i.e. using either the exact solution at every instance in time or fitting a polynomial of sufficient order through the exact solution. These results also show that even with the exact solution there is significant overshoot in some instances and the

predicted signature doesn't always match up with the experimental data. It is our conclusion that is the result of assuming that this process is both adiabatic and isentropic. This works seek to explore what happens when the isentropic assumption is removed and this process is no longer modeled as reversible.

Chapter 6

Ideal Gas – Argon

6.1 Introduction

The Navier-Stokes (NS) equations have a long history of use in fluid mechanics. The Navier-Stokes equations can be used to describe the density profile of a shock wave in a gas [13, 27]. The NS equations provide a proven method for the direct simulation of a shock front in a gas without the use of artificial damping. The NS equations include viscous dissipation and heat conduction which form the basis for the macroscopic view for entropy generation that this works seeks to employ in the dynamic compaction of porous/granular materials. The use of these equations in an ideal gas provides insight into using entropy to replace artificial viscosity.

The objective of the following analysis was to perform direct numeric simulations on perfect gases in order to build up expertise needed to perform direct numeric simulations on granular materials.

6.2 Numeric Solution – Navier-Stokes

Direct numeric simulation of the shock wave structure of argon gas was investigated using the Navier-Stokes equations for one dimensional plane flow

$$\frac{\partial \rho}{\partial t} + \frac{\partial j}{\partial x} = 0, \tag{6.2.1}$$

$$\frac{\partial (\rho u)}{\partial t} + \frac{\partial (ju)}{\partial x} + \frac{\partial P}{\partial x} = \frac{\partial \Pi_{xx}}{\partial x}, \tag{6.2.2}$$

$$\frac{\partial E}{\partial t}+\frac{\partial\left(jH\right)}{\partial x}+\frac{\partial q}{\partial x}=\frac{\partial\left(\Pi_{xx}u\right)}{\partial x}. \tag{6.2.3}$$

The simulations reported here are modeled as a shock tube experiment where the shock wave is stationary and the fluid is in motion. The parameters used in the NS code as related to argon gas can be found in the literature [13].

The numeric and analytic simulations are compared to experimental results [28]. Shock front thickness and entropy for three Mach numbers 1.55, 3.38, and 9 were used in the comparison. The effect of viscosity was studied using three viscosity models; constant viscosity where μ is constant, the Power Law model where μ is a function of temperature to some power $\mu=\mu_{\infty}\left(T/T_{\infty}\right)^{w}$, and Maxwell's viscosity model where $\mu=\frac{2}{3}\frac{\sqrt{mKT/\pi}}{\pi d^{2}}$. The results of a resolution study using the NS code are presented in Table 6.2.1.1. The analytic solution and its associated results will be discussed in the next section.

Recall from section 2.4 that entropy is calculated by integrating over the shock front with the following equation

$$\Delta s=\int\frac{\vec{\Pi}}{T}\frac{du_{x}}{dx}dx-\int\frac{1}{T}\frac{d\vec{q}}{dx}dx. \tag{2.4.1.20}$$

The results obtained from this integration are compared to the change in entropy used for an ideal gas assuming constant specific heats

$$\Delta s=c_{v,avg}\ln\frac{T_{2}}{T_{1}}+R\ln\frac{v_{2}}{v_{1}}. \tag{6.2.4}$$

Shock front thickness is found by initially determining the dimensionless reciprocal shock thickness which is defined as λ/δ where λ is the upstream mean free path and δ is the shock thickness [13]. The reciprocal shock thickness in finite difference form is

$$\frac{\partial \rho}{\partial x} = \frac{\lambda}{\delta} = \max_i[(\rho_{i+2} - \rho_{i-2}) / 2h_x] / (\rho^{(2)} - \rho^{(1)}), \tag{6.2.5}$$

where ρ is density and *hx* is the spatial distance and $\rho^{(2)}$ and $\rho^{(1)}$ are the density values upstream and downstream of the shock front respectively. This equation essentially assumes the shock thickness can be represented by a linear line through the shock front. Equation (6.2.5) assumes that the maximum density gradient is equivalent to the reciprocal shock thickness. The results of the resolution study in Table 6.2.1.1. indicate that at least 50 million iterations were needed in order for the values reported for shock thickness or entropy to converge to a single value.

Given that this problem is a boundary value problem with the application of far field (x→±∞) boundary conditions at the edges, the domain size affects the numeric solution by either decreasing or increasing the shock front thickness. In the ideal gas simulations the symbol "γ" represents the ratio of specific heats. Upstream of the shock front the left boundary conditions (L.B.C) are defined as

$$\rho = \rho_{ref} / \rho_{\infty} = 1,$$

(L.B.C. 1)

$$U = M, \tag{L.B.C. 2}$$

$$P = \frac{1}{\gamma}, \tag{L.B.C. 3}$$

$$E = \rho \frac{U^2}{2} + \frac{P}{\gamma - 1}, \tag{L.B.C. 4}$$

$$T = \frac{\gamma P}{\rho}, \qquad \text{(L.B.C. 5)}$$

$$\eta_{\text{Constant}} = \frac{\mu_0}{\rho_\infty c_\infty \lambda}, \qquad \text{(L.B.C. 6a)}$$

$$\eta_{\text{Power Law}} = \frac{\mu_0 (T)^\omega}{\rho_\infty c_\infty \lambda}, \qquad \text{(L.B.C. 6b)}$$

$$\eta_{Maxwell} = \left(\gamma^{\left(\omega - \frac{1}{2}\right)} 5 \sqrt{\frac{2a\cos(-1)}{16}} \left(\frac{P_i}{\rho_i} \right)^\omega \right) \Big/ \rho_\infty c_\infty \lambda, \qquad \text{(L.B.C. 6c)}$$

$$Jx = \rho U, \qquad \text{(L.B.C. 7)}$$

$$q = 0. \qquad \text{(L.B.C. 8)}$$

where γ is the ratio of specific heat and M is the Mach number. The right boundary conditions (R.B.C) were defined by the Rankine-Hugoniot jump conditions;

$$\rho_i = \frac{\rho(\gamma+1)M^2}{(\gamma-1)M^2+2}, \qquad \text{(R.B.C. 1)}$$

$$P_i = \frac{P\left(2\gamma M^2 - (\gamma-1)\right)}{(\gamma+1)}, \qquad \text{(R.B.C. 2)}$$

$$T_i = \frac{\gamma P_i}{\rho_i}, \qquad \text{(R.B.C. 3)}$$

$$U_i = \frac{U\left(2+(\gamma-1)M^2\right)}{(\gamma+1)M^2}, \qquad \text{(R.B.C. 4)}$$

$$E_i = \frac{\rho_i U_i^2}{2} + \frac{P_i}{\gamma-1}, \qquad \text{(R.B.C. 5)}$$

$$\eta_{\text{Constant}_i} = \frac{\mu_0}{\rho_\infty c_\infty \lambda}, \qquad \text{(R.B.C. 6a)}$$

$$\eta_{\text{Power Law}_i} = \frac{\mu_0 \left(T_i\right)^{\omega}}{\rho_\infty c_\infty \lambda}, \qquad \text{(R.B.C. 6b)}$$

$$\eta_{Maxwell_i} = \left(\gamma^{\left(\omega - \frac{1}{2}\right)} 5 \sqrt{\frac{2a\cos(-1)}{16}} \left(\frac{P_i}{\rho_i} \right)^{\omega} \right) \Big/ \rho_\infty c_\infty \lambda, \qquad \text{(R.B.C. 6c)}$$

$$Jx_i = \rho_i U_i, \qquad \text{(R.B.C. 7)}$$

$$q_i = 0. \qquad \text{(R.B.C. 8)}$$

The jump conditions are used to determine the end state for a material under a prescribed dynamic loading condition, but they do not describe the evolution of the loading process. The domain was split into two separate sections with one half set to the left boundary conditions while the other half was set to the right boundary conditions.

If the domain size is too small the width of the shock front may be too thin in comparison to experimental data, or if the domain size is large the shock front may be too broad in comparison to the available experimental data. Therefore the relative distance between the far field boundary conditions and the shock front is important and should be chosen to accurately describe Dirichlet boundary conditions at infinity. The grid spatial resolution needed is also a function of the domain size. The smaller the domain size the fewer grid nodes that need to be used and the larger the domain size the more grid nodes will be needed. While high resolution may be desired near regions with steep gradients such as the shock front results using the NS code show that high resolution is needed throughout the domain particularly at the far field edges were the boundary conditions are imposed because of the appearance of spurious waves originating at the edges of the domain. High resolution throughout the domain limits the appearance of these waves which have the potential to interfere with the maximum density gradient calculations. In

an effort to have the numerical simulations efficiently converge to the steady state solution with a minimum number of nodes, a resolution study was conducted in which the number of nodes was varied and a resulting solution was converged. Once the solution was converged two metrics were used to assess the accuracy of the solution: shock wave thickness and entropy generation.

6.2.1 Shock Wave Thickness and Entropy Generation

In order to assess the effect of where the far field boundary condition can be applied, a numeric study applying the boundary condition at zeta = 5, 10, 100, etc was carried out. Research efforts concluded that the optimal distance was zeta = +/- 150. Table 6.2.1.1 presents the results of a spatial grid and viscosity model study at total domain size of 300 zeta.

Table 6.2.1.1 Resolution Study of the shock wave structure in argon gas.

Mach # 1.55	Constant Viscosity Model		**Mach# 3.38**	Constant Viscosity Model		**Mach #9**	Constant Viscosity Model	
Nx	ST-DGM	Entropy	Nx	ST-DGM	Entropy	Nx	ST-DGM	Entropy
300	5.47	12.76	300	4.18	60.52	300	NA	NA
600	3.82	15.03	600	2.17	97.98	600	NA	NA
1200	3.29	15.99	1200	1.24	155.35	1200	1.06	16.39
2400	3.04	16.31	2400	0.82	193.12	2400	0.59	281.95
4800	2.99	16.42	4800	0.65	211.08	4800	0.33	517.76
9600	2.97	16.46	9600	0.58	218.63	9600	0.23	629.42
19200	2.97	16.52	19200	0.56	221.82	19200	0.18	685.23
Mach # 1.55	Maxwell Viscosity Model		**Mach# 3.38**	Maxwell Viscosity Model		**Mach #9**	Maxwell Viscosity Model	
Nx	ST-DGM	Entropy	Nx	ST-DGM	Entropy	Nx	ST-DGM	Entropy
300	7.50	14.69	300	5.17	127.25	300	NA	NA
600	6.29	15.84	600	3.42	175.94	600	3.95	408.94
1200	5.95	16.25	1200	2.85	201.70	1200	3.44	562.60
2400	5.83	16.39	2400	2.62	213.76	2400	3.25	643.47
4800	5.80	16.46	4800	2.56	219.29	4800	3.18	688.78
9600	5.80	16.52	9600	2.55	221.94	9600	3.16	712.51
19200	5.79	16.51	19200	2.55	223.06	19200	3.15	724.42
Mach # 1.55	Power Law Viscosity Model		**Mach# 3.38**	Power Law Viscosity Model		**Mach #9**	Power Law Viscosity Model	
Nx	ST-DGM	Entropy	Nx	ST-DGM	Entropy	Nx	ST-DGM	Entropy
300	6.06	13.51	300	NA	NA	300	NA	NA
600	4.62	15.35	600	2.82	152.88	600	NA	NA
1200	4.17	16.08	1200	2.11	189.99	1200	2.51	497.34
2400	4.02	16.33	2400	1.87	208.36	2400	2.26	604.92
4800	3.99	16.43	4800	1.78	216.78	4800	2.19	667.54
9600	3.98	16.50	9600	1.75	220.77	9600	2.17	701.49
19200	3.97	16.49	19200	1.75	222.52	19200	2.16	719.09

Shock front thickness and change in entropy values are shown for the three viscosity models tested. Table values are arranged according to viscosity model and Mach number. The far field is set +/- 150 units and all simulations were carried out to 50 million iterations to satisfy the convergence criteria. The column marked ST-DGM refers to the shock thickness found using the density gradient model of equation 6.2.5.

There are several noteworthy trends that appear in Table 6.2.1.1. Notice that as the resolution increases the entropy and shock thickness values converge to a single value for a given viscosity model and Mach number. The NS converged value for entropy for Mach 1.55 for the constant viscosity model is 16.52 KJ/Kg*K. This value compares favorably to the analytic solution value of 16.49 KJ/Kg*K. The NS value for shock front thickness of 2.97 zeta compares favorably to the analytic solutions value of 3.10 zeta. This trend indicates that the resolution study worked as anticipated with accuracy increasing with increased resolution. The NS code predicted values for entropy production undershoot the anticipated results by a significant margin at low resolution as

compared to the entropy production values at higher resolution. The same trend is displayed for the shock front thickness (ST). For ST values at low resolution the NS code predicts too large a value for the shock front thickness, however as the resolution is increased the results improve depending upon the viscosity model used in the simulation. The results contained in Table 6.2.1.1 show that the viscosity model plays more of a role in the calculation of the width of the shock front as compared to entropy production. The Power Law viscosity model outperforms the constant viscosity assumption and the Maxwell viscosity model irrespective of the resolution used. The Maxwell viscosity model returns a value for viscosity that is too large for the given conditions and as a result over dampens the shock and spreads out the shock front. Constant viscosity makes the shock front too thin at higher Mach numbers which conflicts with experimental data [28]. The experimental data shows that in a gas the shock front starts off at some finite value at a Mach number around 1 and then reaches a minimum near Mach 3.5 and once again thickens as the Mach number continues to increase. Since the constant viscosity model doesn't adjust the viscosity to changes in pressure or temperature the predictions of a progressively thinner shock front with increasing Mach number falls in line with expectations.

The analytic solution results are contained in Table 6.2.1.2. It should be noted that the analytic solution assumes that viscosity is constant and doesn't change with temperature or pressure. That is why the shock thickness (ST) values listed in Table 6.2.1.2 continue to decrease as Mach number increases. The entropy values shown in Table 6.2.1.2 were calculated using the change in entropy equation for an ideal gas.

Table 6.2.1.2: Analytic results for shock front thickness and the change in entropy.

Mach # 1.55		**Mach# 3.38**		**Mach #9**	
ST	ΔS [KJ/Kg*K]	ST	ΔS [KJ/Kg*K]	ST	ΔS [KJ/Kg*K]
3.10	16.49	0.72	224.55	0.23	738.31

Figure 6.2.1.1 graphs the change in entropy as a function of Mach number for the three viscosity models used in this work. As seen in Fig. 6.2.1.1 the effect of the viscosity model on entropy is small except at higher Mach numbers where it appears that use of Maxwell's viscosity model results in the largest amount of entropy produced as compared to the other two models and the Power Law model returning the smallest entropy production value. The ideal gas entropy production values on Fig. 6.2.1.1 were generated using equation 6.2.4. There is good agreement between the numeric solutions and the ideal gas analytic solution at low Mach numbers before deviating away from the ideal gas analytic solution at higher Mach numbers. The Maxwell viscosity model has the best prediction of entropy production values when compared to the ideal gas analytic solution.

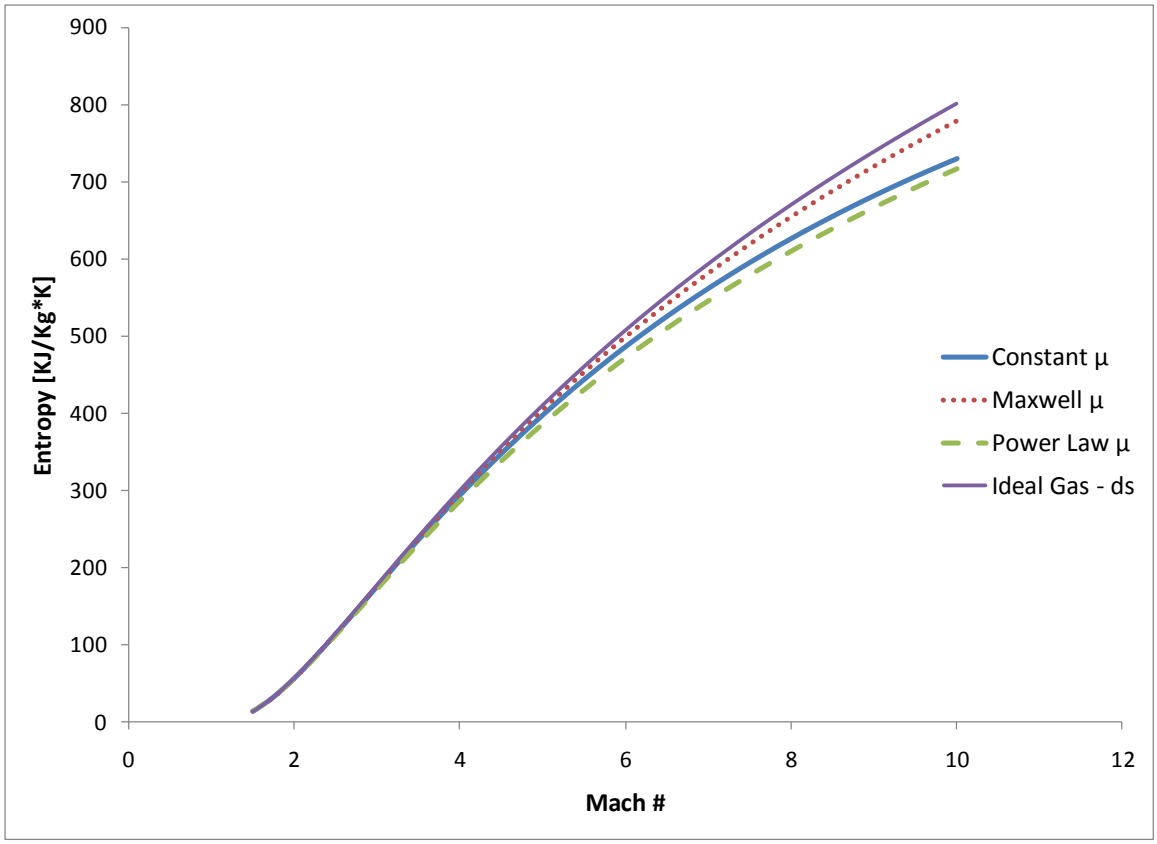

Figure 6.2.1.1: Change in Entropy vs. Mach number for the ideal gas change in entropy equation and the three viscosity models; constant viscosity, Maxwell viscosity, Power Law viscosity.

Figure 6.2.1.2 graphs reciprocal shock thickness versus Mach number. As seen in this figure the assumption that viscosity remains constant across a shock front and remains unaffected by temperature or pressure adversely affects the density gradient and causes poor predictions for the reciprocal shock thickness.

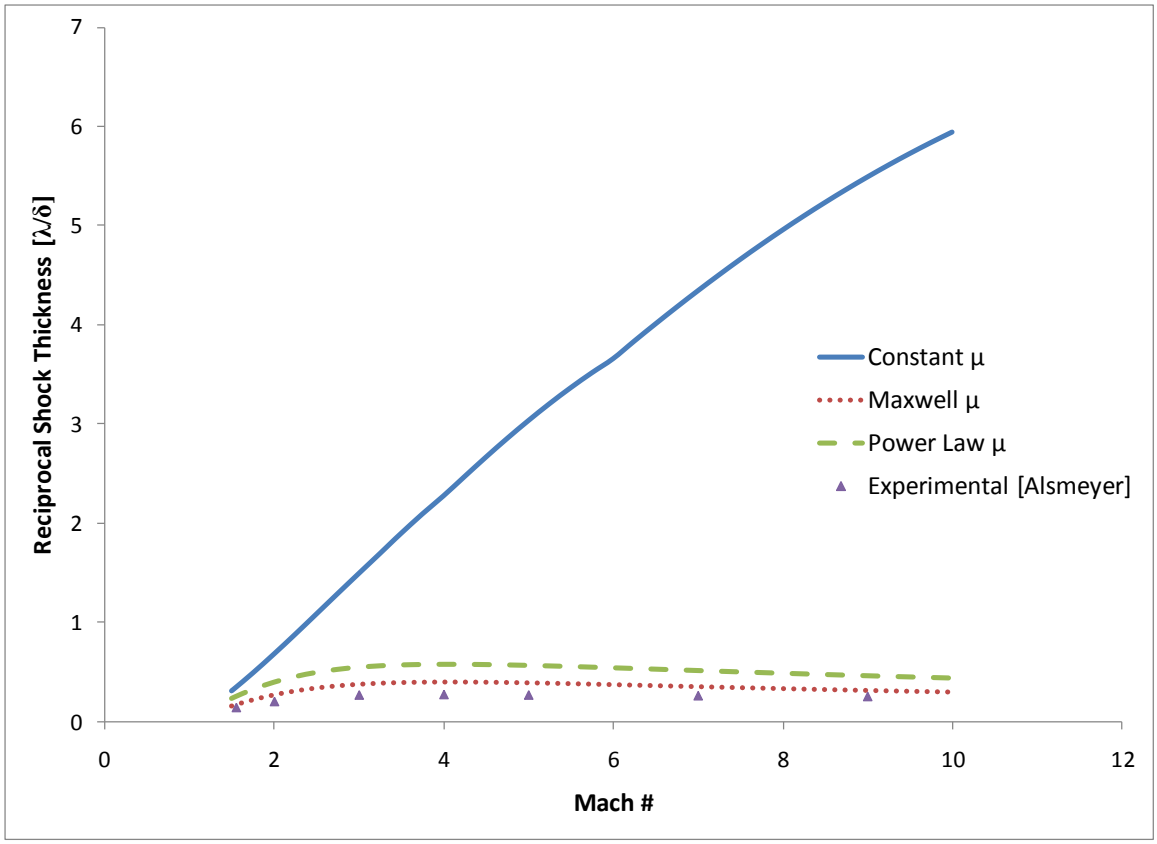

Figure 6.2.1.2: Reciprocal shock thickness versus Mach number. The constant viscosity line indicates that the assumption of constant viscosity does not work well when using the density gradient to determine reciprocal shock thickness.

Figure 6.2.1.3 is the same graph as Fig. 6.2.1.2 except that the constant viscosity data is removed from the graph permitting closer inspects of the variable viscosity models, the Power Law model and Maxwell's viscosity model, and Alsmeyer's experimental data [28]. The important feature of Fig. 6.2.1.3 is that is shows that the shock front is thicker at lower Mach numbers, reaching a maxima near 3.5, and then decreases as the Mach number increases as expected but then the shock front thickens again at higher Mach numbers. The experimental data by Alsmeyer also exhibits this trend [28].

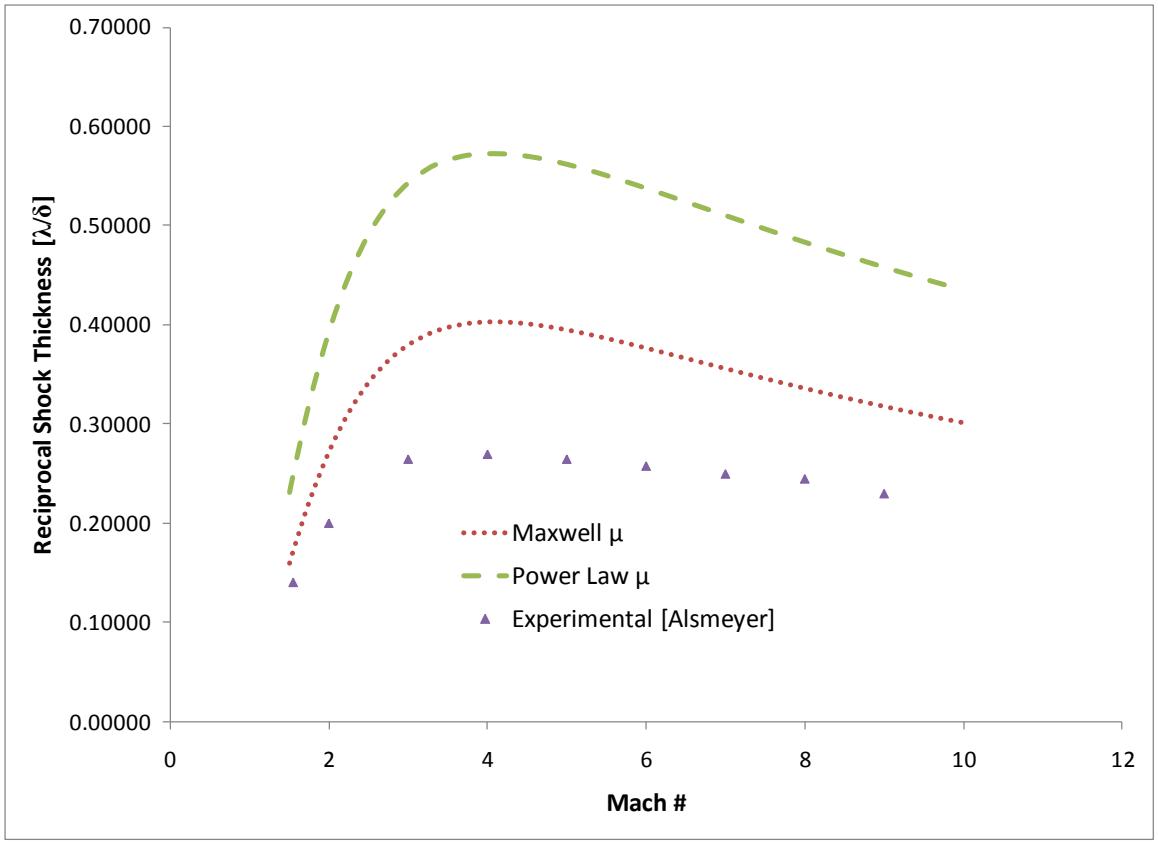

Figure 6.2.1.3: Reciprocal Shock Thickness versus Mach number. Note the minimum shock thickness occurs near Mach # 3.5.

6.3 Analytic Solution

The full derivation of the analytic solution to a one-dimensional stationary shock wave in a gas is available in the open literature [29, pg. 150]; the results are presented below for completeness. The result of this derivation is a non-linear closed form solution

$$\frac{1-\phi}{(\phi-\alpha)^{\alpha}} = \exp\left[\beta Ma_1 (1-\alpha)(\zeta-\zeta_0)\right], \tag{6.3.1}$$

where $\beta = \frac{9}{8}(\gamma-1)\sqrt{\frac{\pi}{8\gamma}}$, $\alpha = \frac{\gamma-1}{\gamma+1} + \frac{2}{\gamma+1}\frac{1}{Ma_1^{\,2}}$, and $Ma_1 = \frac{v_1}{\sqrt{\gamma R T_1 / M}}$.

This solution is transcendental in ϕ which is the dimensionless velocity defined as the local velocity v_x by the upstream velocity v_1, where $\phi = v_x / v_1$. The dimensionless spatial coordinate ζ is defined by the relation x/λ, where x is the current position in the domain

and λ is the mean free path of the gas upstream of the shock, and $\zeta_0 = x_0/\lambda$. A solution for equation 6.3.1 is obtained through the bisection method found in Numerical Recipes. Thus the analytic solution can be compared with the NS solutions and the experimental data obtained from the literature [28].

Figure 6.3.1 compares the analytic solution to the numeric solution and the experimental data for argon gas with an inlet Mach number of 9, Pr is 2/3, R is 208.1 J/Kg*K, initial density is 1.62 Kg/m^3, and γ is 5/3. Figure 6.3.1 contains several data sets of the NS solution and displays them according to grid spatial resolution. As seen in Fig 6.3.1 there is good agreement between the analytic and numeric solutions. Note that as the resolution increases the numeric solution converges to the analytic solution which is as expected since they are both assuming constant viscosity. The rise time of shock front is too rapid for the analytic and numeric solutions as compared to the experimental data. The analytic and numeric solutions are predicting a nearly instantaneous change in the thermodynamic state of the gas whereas the experimental data shows that the change in state takes place over a finite distance and time.

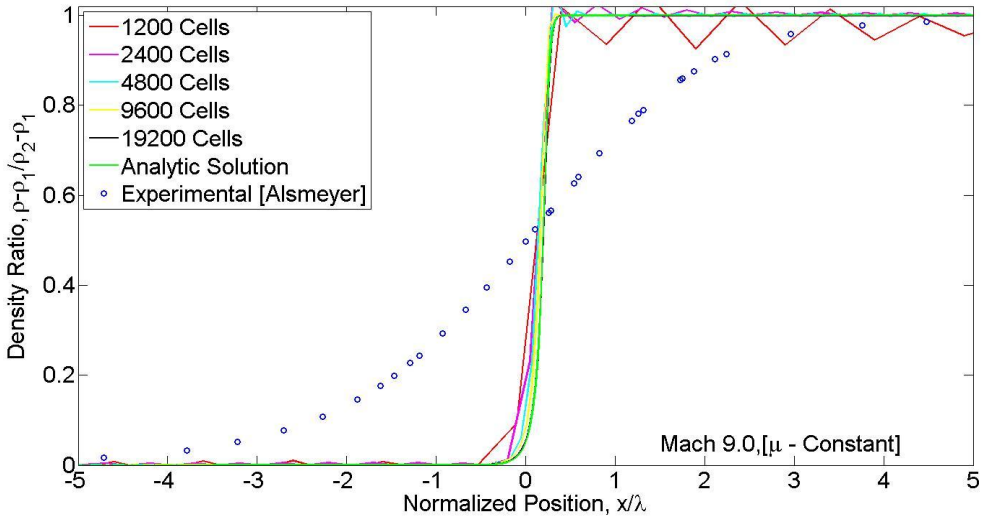

Figure 6.3.1: Analytic Solution versus Numeric Solution and Experimental Data for argon gas at Mach 9 assuming constant viscosity.

Figure 6.3.2 compares the analytic and numeric solutions to the Mach 9 experimental data. In the numeric simulations the constant viscosity assumption was replaced with Maxwell's viscosity model. In general the numeric solution more closely matches the experimental data than does the analytic solution. This suggests that the Maxwell viscosity model is an improvement over the constant viscosity assumption used for the analytic solution.

The results shown in Fig. 6.3.2 are replicated in Fig. 6.3.3. The only difference between these two graphs is that the numeric solutions presented in Fig. 6.3.3 incorporate the Power Law viscosity model. While the Power Law viscosity model is an improvement over the constant viscosity assumption it does not perform as well as Maxwell's viscosity model under these prescribed conditions. Nevertheless these results indicate that when applying the NS equations in one-dimensional plane flow to an ideal gas the temperature or pressure effects should be taken into account when calculating viscosity.

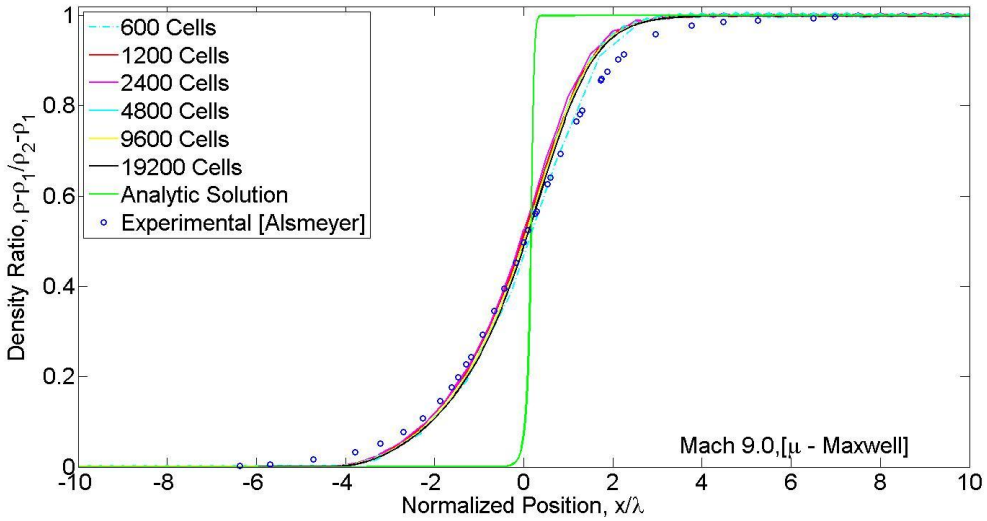

Figure 6.3.2: Analytic Solution versus Numeric Solution and Experimental Data for argon gas at Mach 9 using Maxwell's viscosity model.

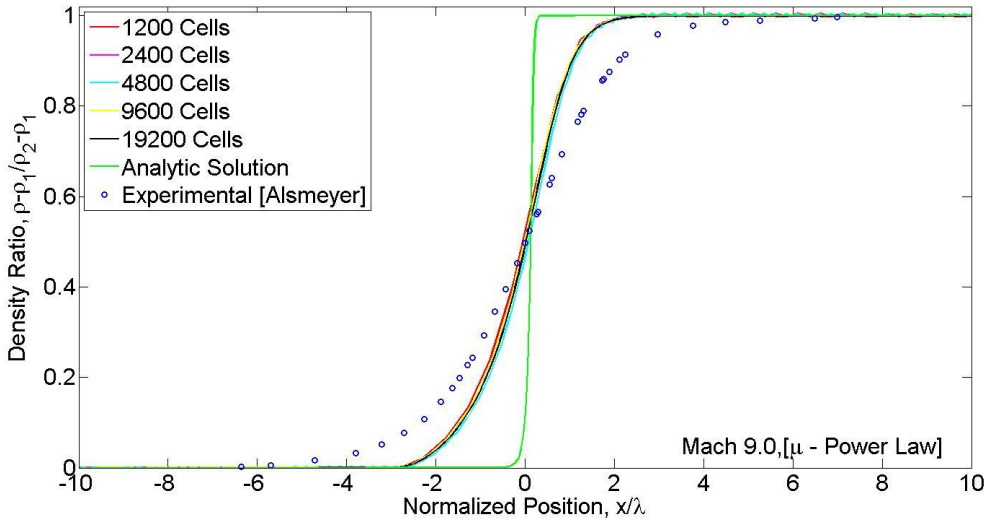

Figure 6.3.3: Analytic Solution versus Numeric Solution and Experimental Data for argon gas at Mach 9 using the Power Law viscosity model.

Figure 6.3.4 compares the analytic and numeric solutions to the experimental data for argon gas at Mach 3.38. Note the magnitude of the oscillations in the NS generated solutions. These oscillations are damped as the resolution is increased. At higher resolution the numeric data converges to the analytic solution at spatial grids greater or equal to 4800 cells. The nearly vertical assent of the shock front for the numeric and

analytic solutions is substantially greater at Mach 3.38 as compared to the experimental data at Mach 9. This indicates that as the shock front widens the worse the assumption of constant viscosity becomes.

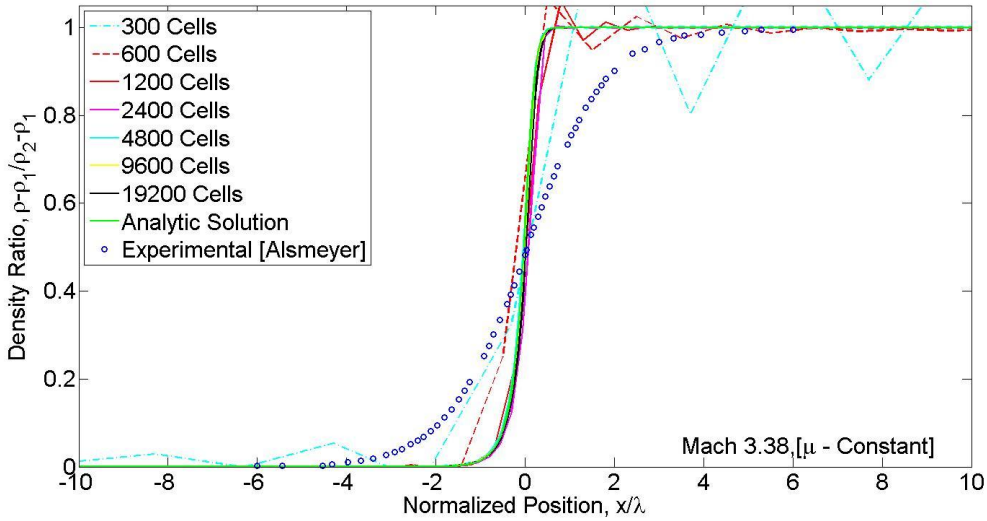

Figure 6.3.4: Analytic Solution versus Numeric Solution and Experimental Data for argon gas at Mach 3.38 assuming constant viscosity.

Figure 6.3.5 and Fig. 6.3.6 shows the effect of the two temperature dependent viscosity models, the Power Law viscosity model and Maxwell's viscosity model, on the NS equations ability to model the shock wave structure of argon gas at Mach 3.38. The temperature dependent viscosity models perform better under these conditions than the constant viscosity case. The Maxwell's viscosity model produces the best results for the Navier-Stokes equations. However, the numeric results for Mach 3.38 using Maxwell's viscosity model do not follow the experimental data as well as in the Mach 9 results.

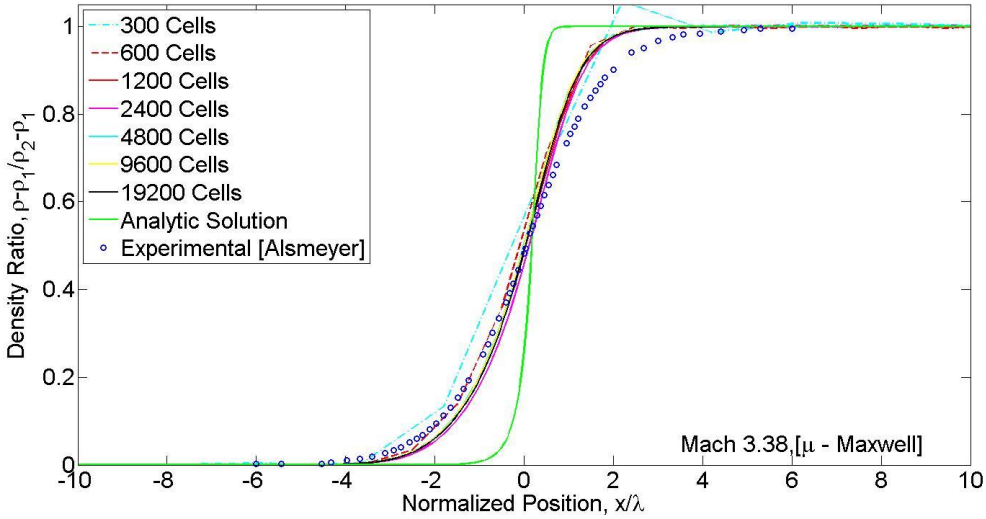

Figure 6.3.5: Analytic Solution versus Numeric Solution and Experimental Data for argon gas at Mach 3.38 using Maxwell's viscosity model.

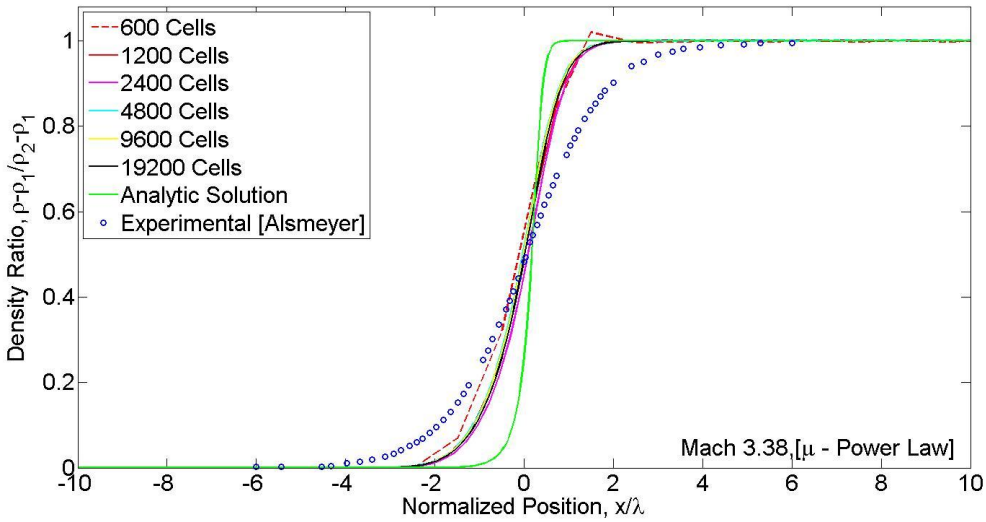

Figure 6.3.6: Analytic Solution versus Numeric Solution and Experimental Data for argon gas at Mach 3.38 using the Power Law viscosity model.

The last experimental data set is for the 1.55 Mach number. The results of this resolution study are similar to the results for the Mach 3.38 and Mach 9 cases. The numeric simulation results generated using Maxwell's viscosity model match up well to the experimental data in regards to shock front thickness. The constant viscosity model predictions are too steep relative to the experimental data. Power Law viscosity produces

results that are similar to the Maxwell viscosity model results. Since these results are in line with the previous results no discussion will be presented here and the reader is encouraged to review the observation of the Mach 3.38 and Mach 9 cases.

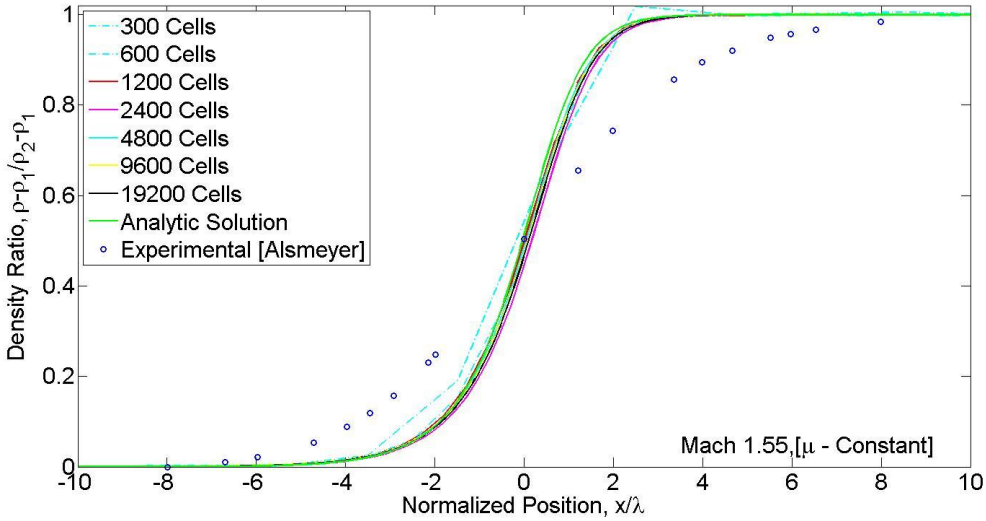

Figure 6.3.7: Analytic Solution versus Numeric Solution and Experimental Data for argon gas at Mach 1.55 assuming constant viscosity.

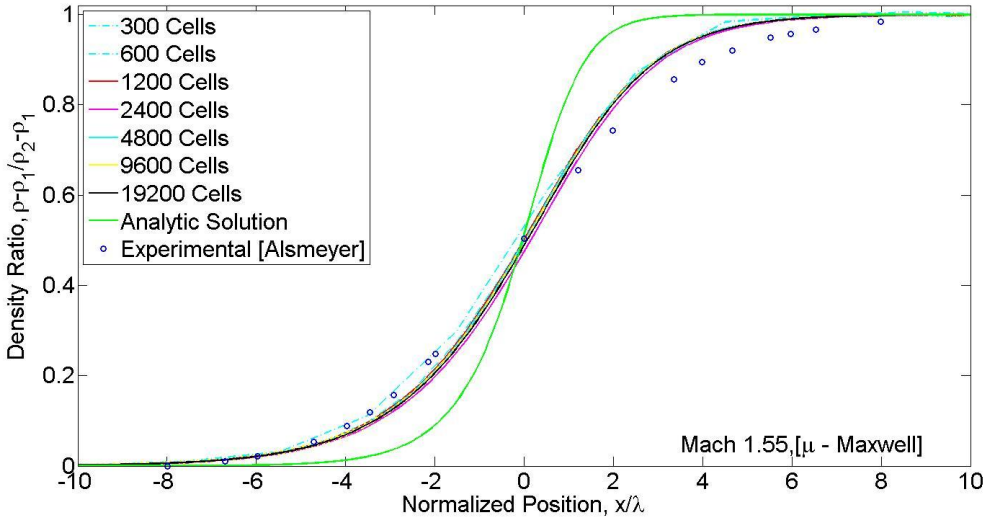

Figure 6.3.8: Analytic Solution versus Numeric Solution and Experimental Data for argon gas at Mach 1.55 using Maxwell's viscosity model.

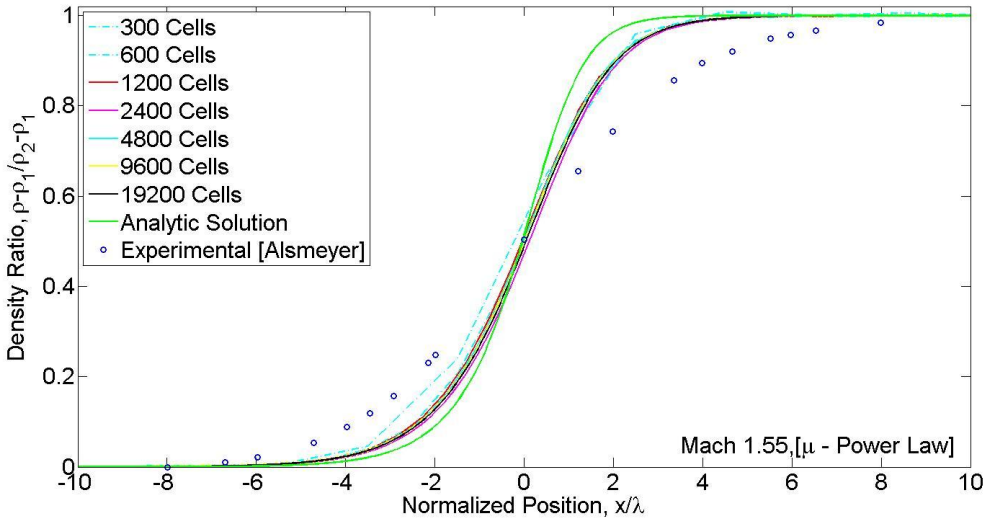

Figure 6.3.9: Analytic Solution versus Numeric Solution and Experimental Data for argon gas at Mach 1.55 using the Power Law viscosity model.

In order to accurately model one-dimensional shock wave structures in compressible fluids with the dimensionless, second order accurate Navier-Stokes equations in finite difference form there are several important features needed and they are; a temperature and or pressure dependent viscosity model, a minimum grid resolution of four cells per unit length or at least ten cells across the shock front. The temperature dependent viscosity models take into account that the viscosity of a compressible fluid increases with increasing temperature. Without this adjustment to the viscosity value there is insufficient viscous dissipation within the shock front, which leads to over predicting the rise time and under predicting the shock width. The minimum grid resolution becomes important as the Mach number increases because any simulation with a resolution below this threshold fails to run to completion because the gradients are too large to be numerically resolved using the NS equations. At Mach numbers below Mach 3 the grid resolution becomes less important because the shock front is near its maximum width value and all resolution cases tested produced valid results as in the Mach 1.55 case

study. The total cells in the domain may be decreased if the total domain size is made smaller. However, the downside is that shrinking the domain might artificially alter the shock thickness as a result of applying the boundary conditions too close to the shock structure. Higher resolution near steep gradients is not sufficient to produce good results, because low resolution near the boundary edges produces spurious waves that interfere with the density gradient calculation producing erroneous results for reciprocal shock thickness.

6.4 Momentum Flux

Consider the momentum conservation equation rewritten below. It states that the time rate of change of momentum is equal to the gradient of the shear stress tensor minus the momentum flux minus the pressure.

$$\frac{\partial(\rho u)}{\partial t} = \frac{\partial \Pi_{xx}}{\partial x} - \frac{\partial(ju)}{\partial x} - \frac{\partial P}{\partial x}. \tag{6.4.1}$$

Figure 6.4.1 is a graph of the dimensionless derivatives vs. the normalized position for argon gas at Mach 1.55 assuming constant viscosity. This graph shows that the change in shear stress across the shock front is minimal and that the momentum flux is nearly identical to the pressure gradient across the shock front.

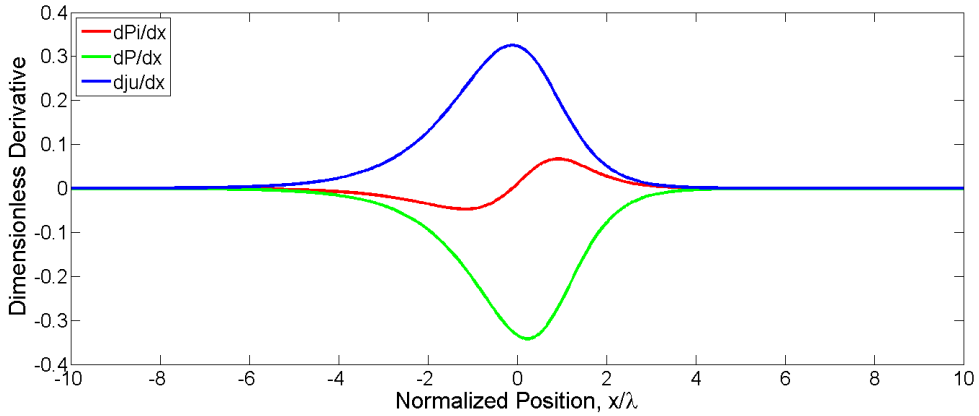

Figure 6.4.1: Derivative contribution to the conservation of momentum equation for argon gas at Mach 1.55 assuming constant viscosity.

Figure 6.4.2 is a graph of the dimensionless derivatives vs. the normalized position for argon gas at Mach 3.38 with constant viscosity. Note that the dimensionless values have increased by an order of magnitude while the velocity has increased from Mach 1.55 to Mach 3.38.

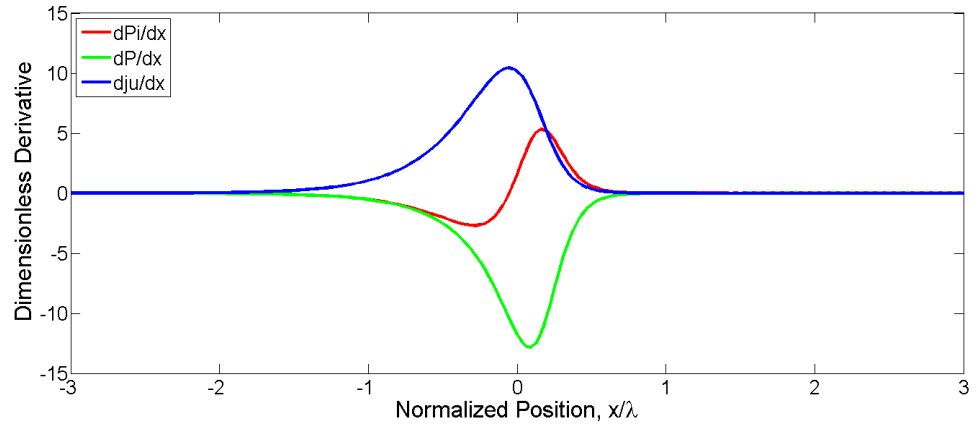

Figure 6.4.2: Derivative contribution to the conservation of momentum equation for argon gas at Mach 3.38 assuming constant viscosity.

Figure 6.4.3 is a graph of the dimensionless derivatives vs. the normalized position for argon gas at Mach 9 with constant viscosity. Note that the dimensionless values have increased again by an order of magnitude while the velocity has increased from Mach 3.38 to Mach 9.

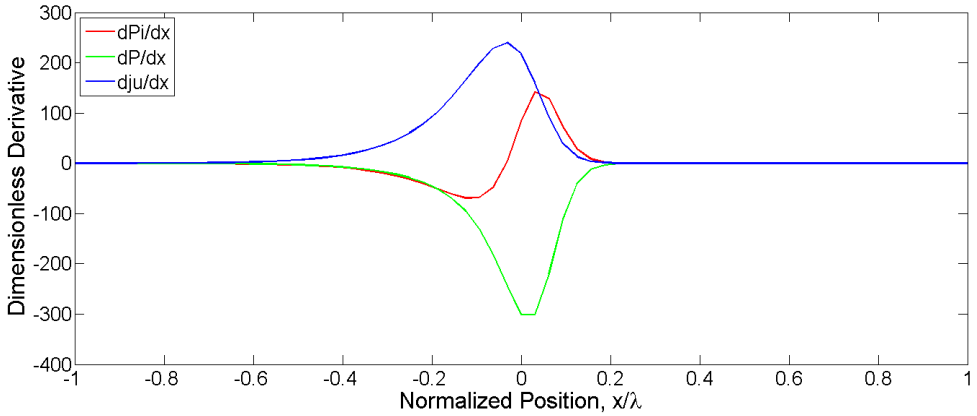

Figure 6.4.3: Derivative contributions to the conservation of momentum equation for argon gas at Mach 9 using the constant viscosity model.

The general trends seen in Figures 6.4.1 – 6.4.3 is that as the Mach number increases the dimensionless derivative values increase. Away from the shock front the derivative values go to zero. The pressure and momentum flux gradients become more weighted towards the downstream high pressure side of the shock front while the shear stress gradient remains evenly weighted across the entire shock front. The normalized position over which the derivatives change decreases as the Mach number increases so that the derivative gradient becomes steeper. This particular trend is observed when using the constant viscosity model, which predicts that as the Mach number increases the shock front thickness decreases. Using a temperature dependent viscosity model such as the Power Law or Maxwell's viscosity model the shock front thickness starts at some finite value then decreases until it reaches a minimum value then increases again to some maximum value. This trend is consistent with experimental data for various gases [28]. This trend is also observed in Figures 6.4.4 – 6.4.6, which demonstrate the effect of using Maxwell's viscosity model.

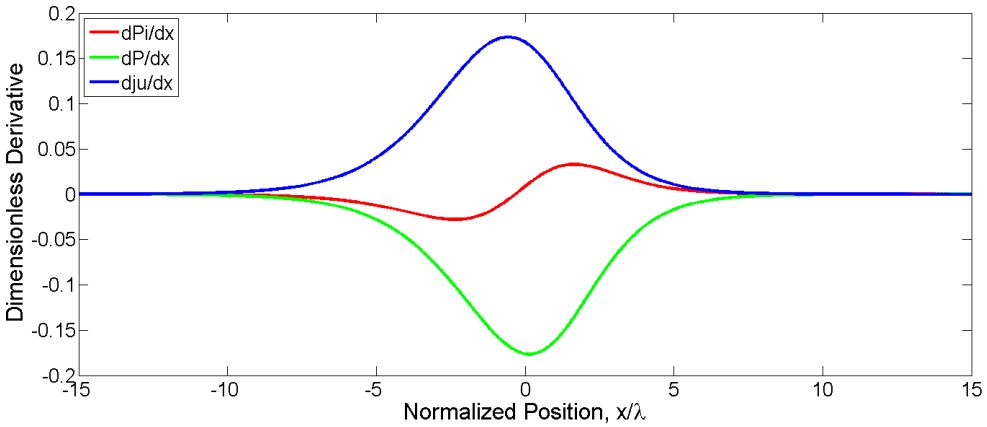

Figure 6.4.4: Derivative contribution to the conservation of momentum equation for argon gas at Mach 1.55 using Maxwell's viscosity model.

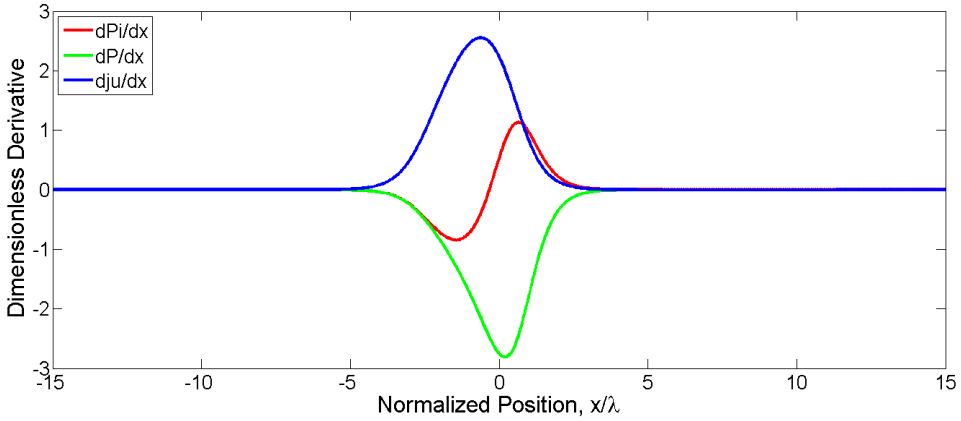

Figure 6.4.5: Derivative contribution to the conservation of momentum equation for argon gas at Mach 3.38 using Maxwell's viscosity model.

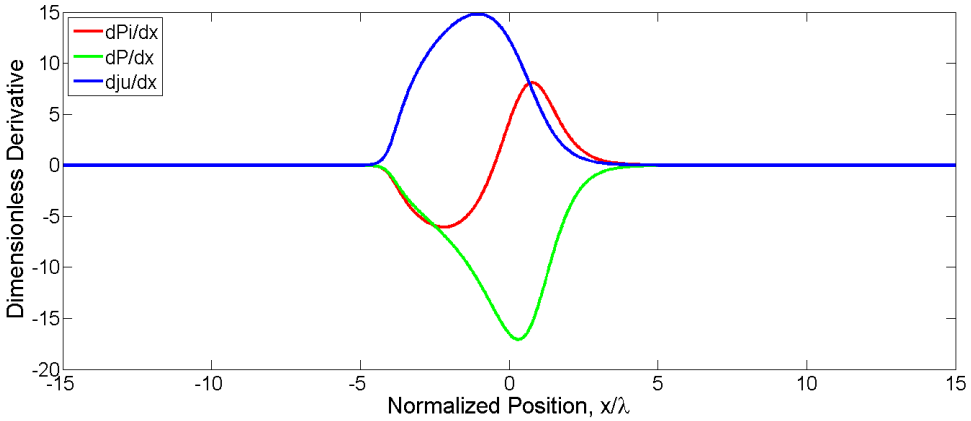

Figure 6.4.6: Derivative contribution to the conservation of momentum equation for argon gas at Mach 9 using Maxwell's viscosity model.

Figure 6.4.7 shows the effect of the Power Law viscosity model on the derivative contributions to the conservation of momentum. The shock front thickness starts at some finite value in (a) then reaches a minimal value near (b) before it increases again in (c).

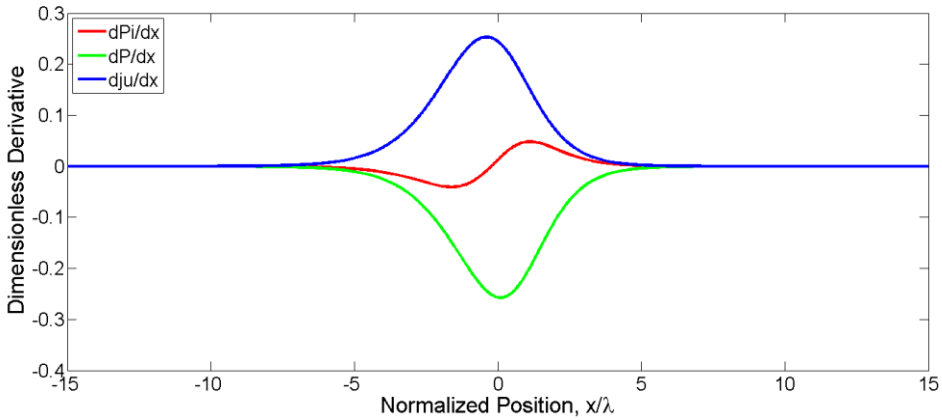

(a)

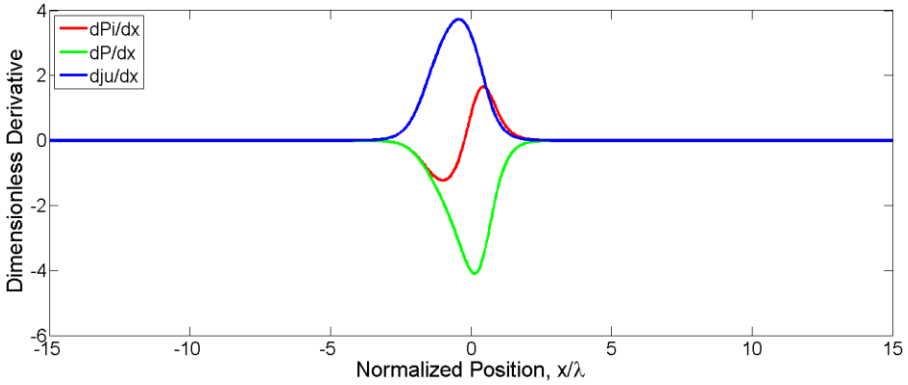

(b)

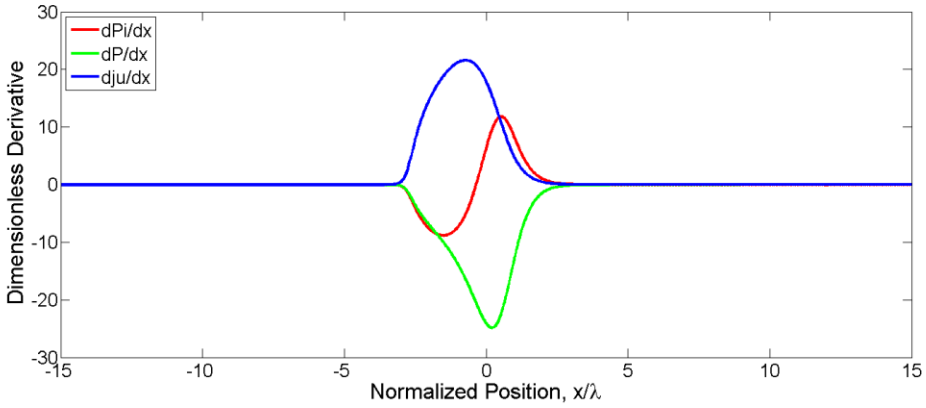

(c)

Figure 6.4.7: Derivative contribution to the conservation of momentum equation for argon gas at Mach1.55 (a), Mach 3.38 (b), and Mach 9 (c) using the Power Law viscosity model.

6.5 Energy Flux

The energy equation used in these simulations is presented below. It states that the time rate of change of energy, which is power, is equal to the gradient of shear flux minus the work flux minus the heat conduction.

$$\frac{\partial E}{\partial t} = \frac{\partial\left(\Pi_{xx} u\right)}{\partial x} - \frac{\partial\left(jH\right)}{\partial x} - \frac{\partial q}{\partial x}. \tag{6.5.1}$$

Figure 6.5.1 shows how these gradients change across the shock front for argon gas at Mach 1.55, Mach 3.38, and Mach 9 assuming viscosity is constant. Note that the work flux term remains relatively negligible despite the shock front thinning and the gradients becoming steeper as the Mach number increases.

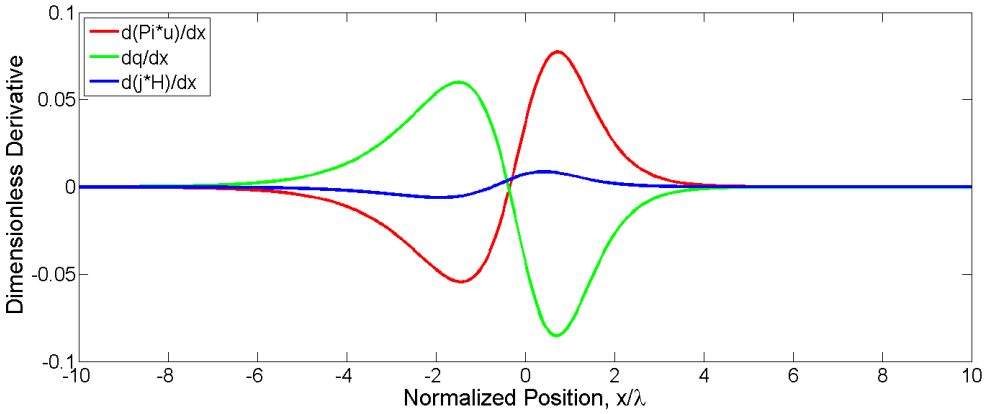

(a)

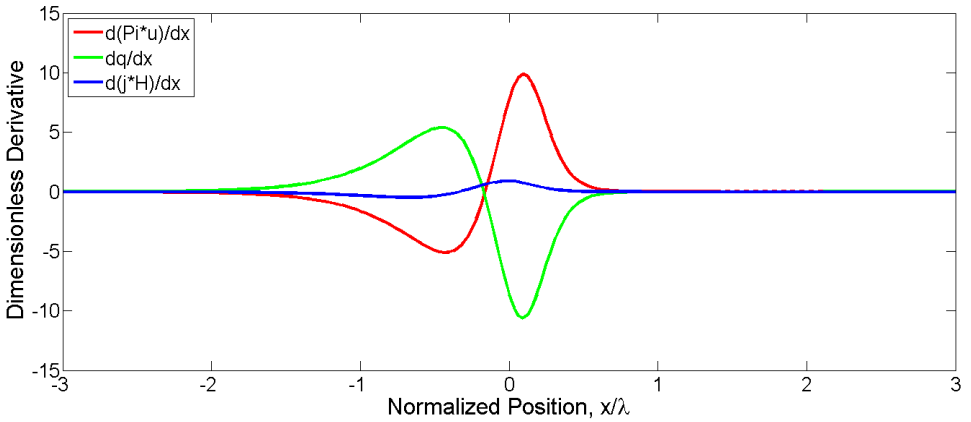

(b)

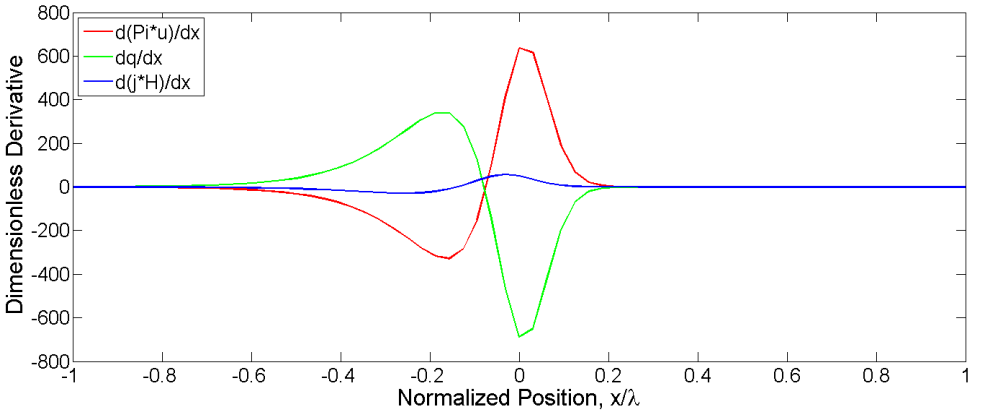

(c)

Figure 6.5.1: Derivative contribution to the conservation of energy equation for argon gas at Mach1.55 (a), Mach 3.38 (b), and Mach 9 (c) using constant viscosity.

The same trends seen in the momentum derivatives, assuming constant viscosity, are displayed in Fig 6.5.1. The shock front thickness is decreasing with increasing Mach number and the amplitude of the gradients is increasing with increasing Mach number. Figure 6.5.2 and Figure

6.5.3 show the effect of the temperature dependent viscosity model on the time rate of change of energy.

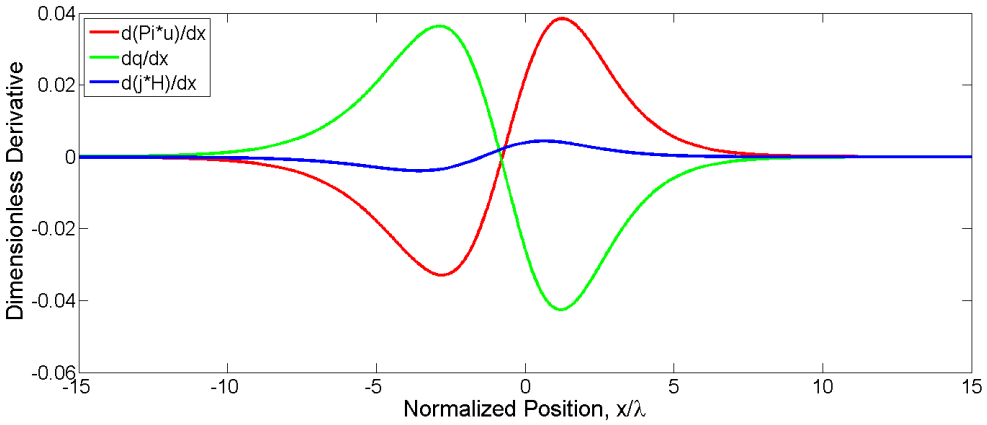

(a)

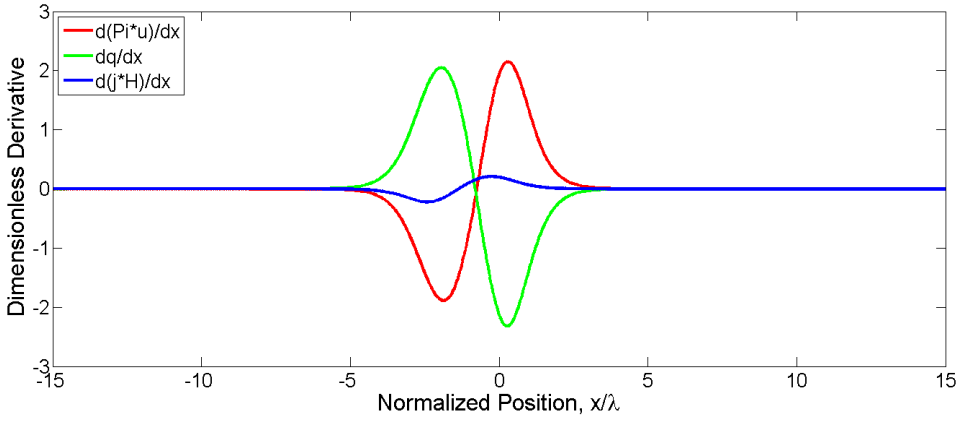

(b)

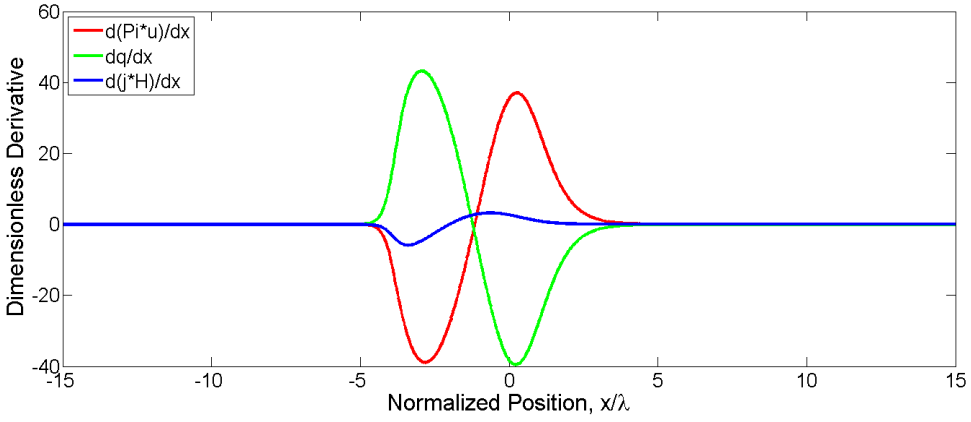

(c)

Figure 6.5.2: Derivative contribution to the conservation of energy equation for argon gas at Mach1.55 (a), Mach 3.38 (b), and Mach 9 (c) using Maxwell's viscosity model.

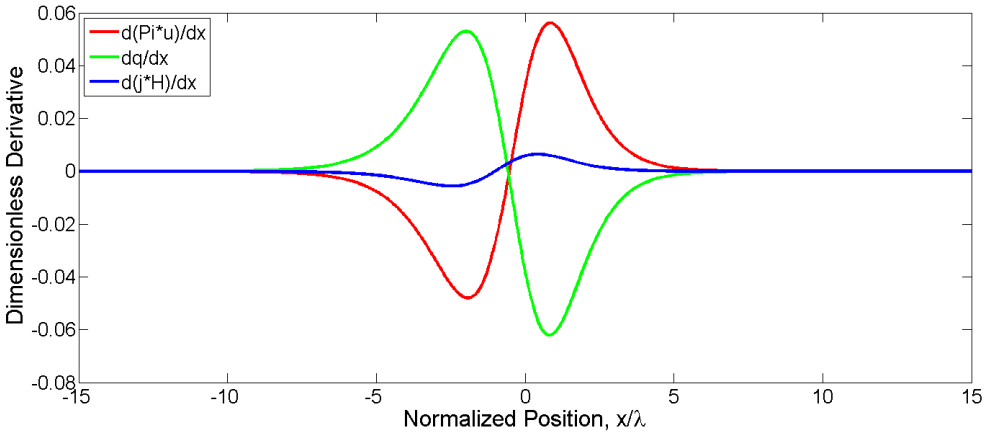

(a)

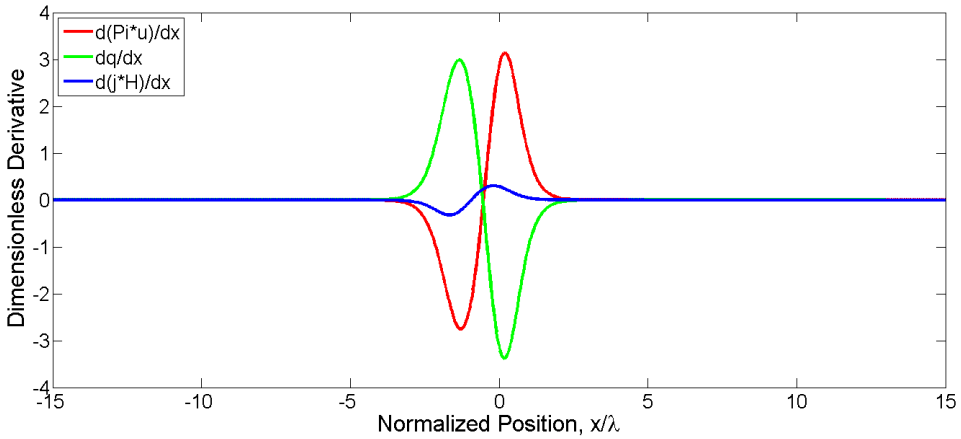

(b)

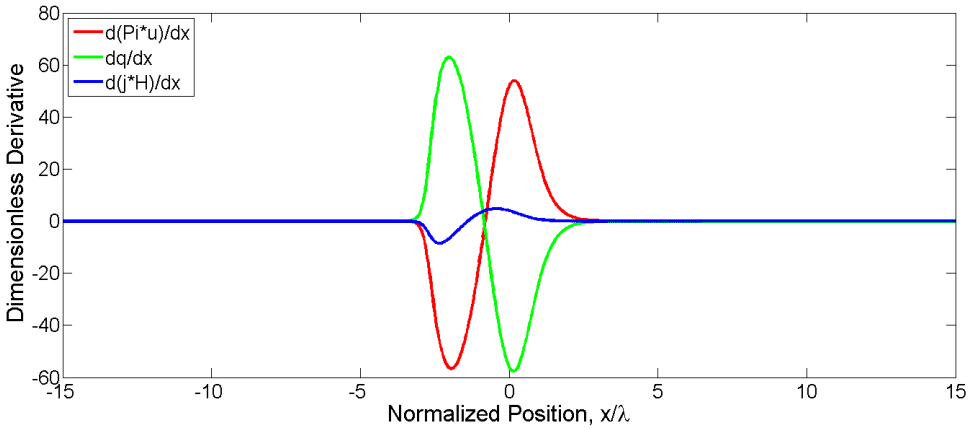

(c)

Figure 6.5.3: Derivative contribution to the conservation of energy equation for argon gas at Mach1.55 (a), Mach 3.38 (b), and Mach 9 (c) using the Power Law viscosity model.

6.6 Total Energy

The effect of the viscosity model on the total energy is negligible as shown in Figures 6.6.1 – 6.6.3. The Mach number has the obvious impact of increasing the kinetic energy until the initial total energy and initial kinetic energy are nearly identical at higher Mach numbers. At high Mach numbers the total energy and kinetic energy are offset by minimal energy level available at room temperature for an ideal gas.

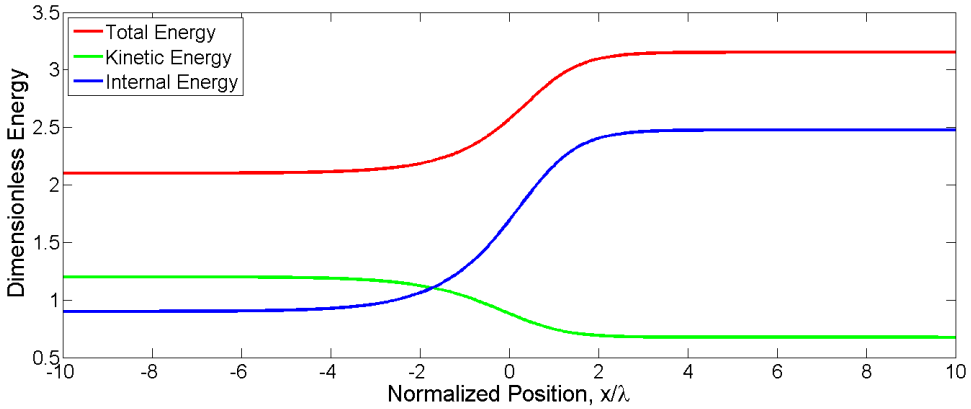

Figure 6.6.1: Total energy, kinetic energy, and internal energy vs. normalized position for argon gas at Mach1.55 assuming constant viscosity.

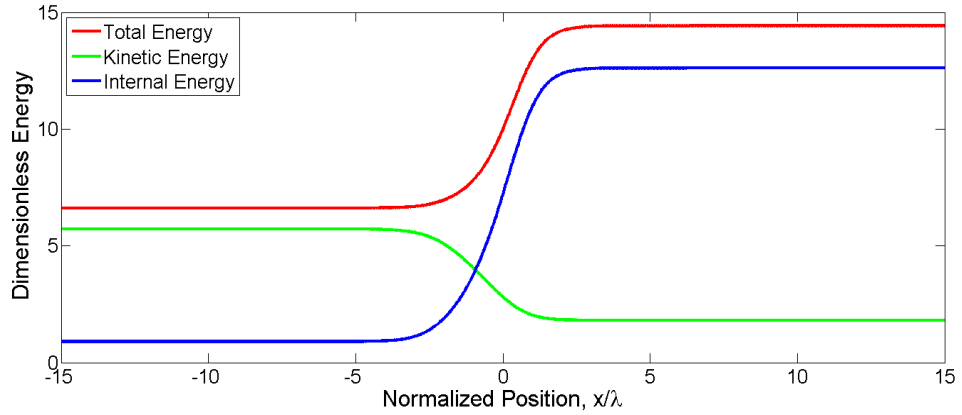

Figure 6.6.2: Total energy, kinetic energy, and internal energy vs. normalized position for argon gas at Mach 3.38 using Maxwell's viscosity model.

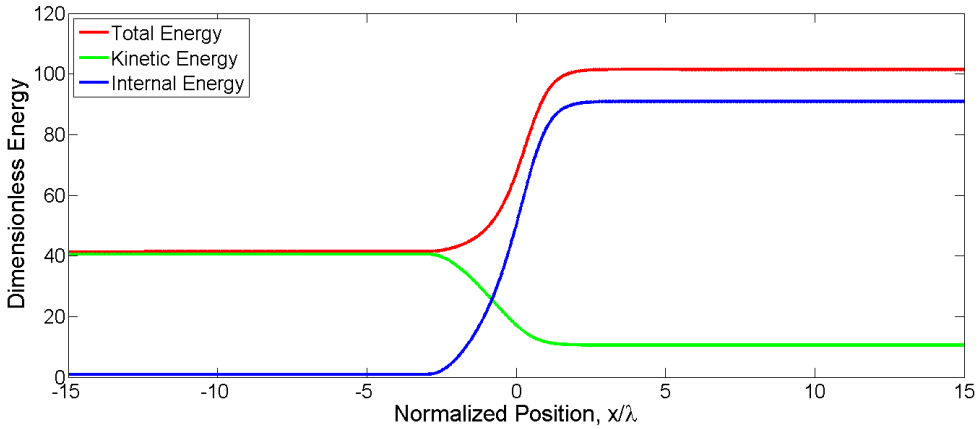

Figure 6.6.3: Total energy, kinetic energy, and internal energy vs. normalized position for argon gas at Mach 9 using the Power Law viscosity model.

6.7 Viscous Dissipation and Heat Conduction

Irreversibilities based on bulk thermodynamic concepts are used in this formulation instead of artificial viscosity. The bulk thermodynamic irreversibilities are shear stress and heat conduction. In their discritized form heat conduction and shear stress are defined as:

$$\Pi_{i+1} = \frac{4}{3}\left(\frac{1}{2}\left(\eta_{i+2} + \eta_i\right)\right)\left(\frac{u_{i+2} - u_i}{h_x}\right), \tag{6.7.1}$$

$$q_{i+1} = -\frac{1}{(\gamma - 1)\,\mathrm{Pr}}\left(\frac{1}{2}\left(\eta_{i+2} + \eta_i\right)\right)\left(\frac{T_{i+2} - T_i}{h_x}\right). \tag{6.7.2}$$

Figures 6.7.1 – 6.7.3 show the dimensionless quantities for shear stress and heat conduction for argon gas at Mach 1.55, Mach 3.38, and Mach 9 respectively; assuming constant viscosity or using Maxwell's viscosity model or the Power Law viscosity model. Note that the shear stress and heat conduction dimensionless quantities are of the same order of magnitude and therefore both sources of irreversibility are important and contribute to the dissipative process that replaces the artificial viscosity model. This

equality in magnitude between viscous dissipation and heat conduction is gases may not be true in other mediums and may be the reason why these two sources of irreversibility have difficulty replaces artificial viscosity in those particular mediums.

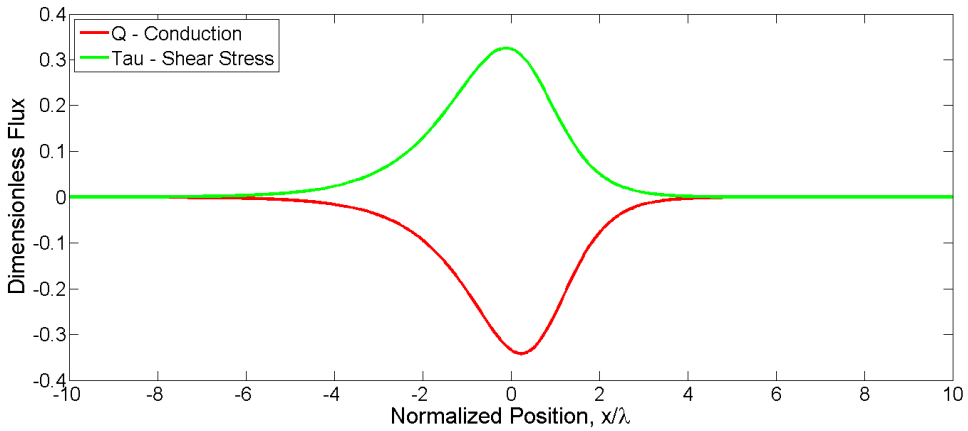

Figure 6.7.1: Dimensionless shear stress and heat conduction vs. normalized position for argon gas at Mach1.55 assuming constant viscosity

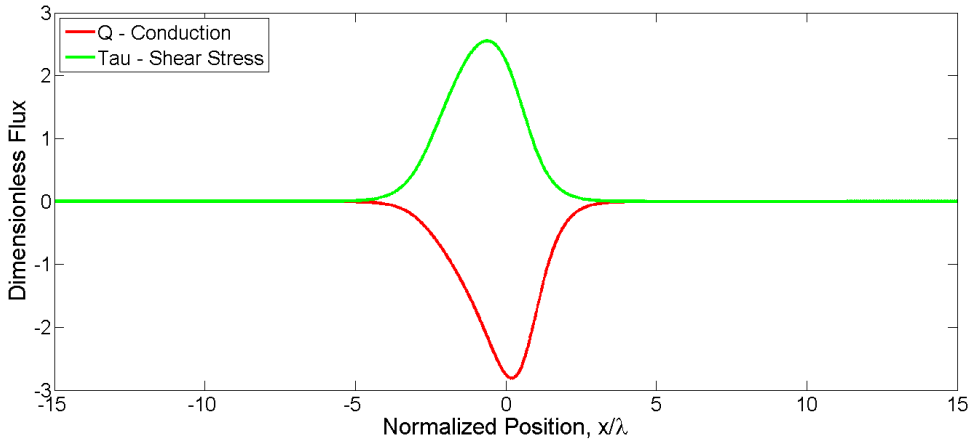

Figure 6.7.2: Dimensionless shear stress and heat conduction vs. normalized position for argon gas at Mach 3.38 using Maxwell's viscosity model.

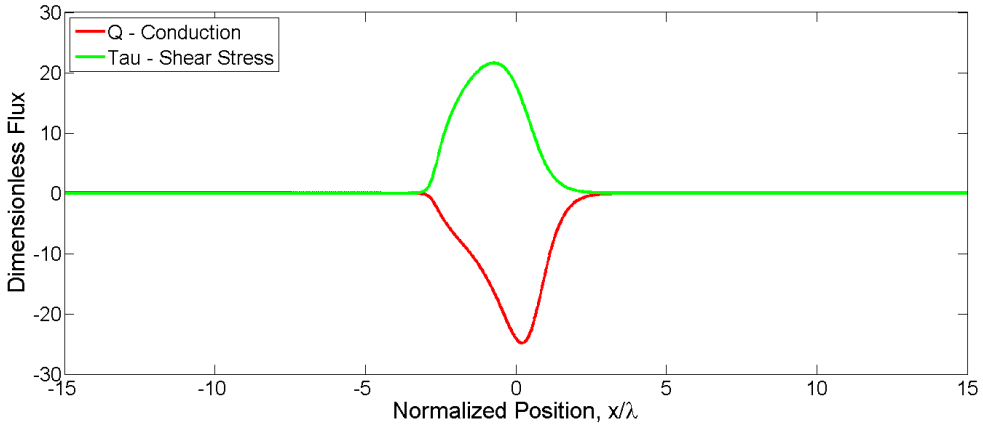

Figure 6.7.3: Dimensionless shear stress and heat conduction vs. normalized position for argon gas at Mach 9 using the Power Law viscosity model.

Chapter 7

Liquids & Solids

7.1 Introduction - Liquids

The one-dimensional second order accurate Navier-Stokes (NS) equations in finite difference form are applied to compressible Newtonian fluids. The particular fluid studied in this work is liquid water due to the abundance of experimental data. The NS equations and code are readily applicable to liquids because the formulation was derived for Newtonian fluids. However, the equation of state will have to be modified from ideal gas to Mie-Grüneisen. Material strength is typically ignored in liquids, therefore there is no need to include a strength of material model to account for plastic deformation and work.

The equation of state used in the NS code changes from the ideal gas law to the Mie-Grüneisen equation of state [14]. The Mie-Grüneisen equation of state is applicable to liquids since they are compressible and fully consolidated. Recall from Chapter 5 that the Mie-Grüneisen equation of state asserts that pressure is function of volume change and internal energy. Using the Mie-Grüneisen equation of state and artificial viscosity KO does an adequate job of modeling shocks in liquids. Therefore this work seeks to successfully model shock wave structures in liquids with the NS code using the Mie-Grüneisen equation of state without the aid of artificial viscosity.

When working with the NS code the initial/boundary conditions are important because this code is used to numerically resolve the shock front. In the case of

compressible substances the initial/boundary conditions are determined through the jump conditions which are function of γ, the ratio of specific heats, and Mach number. In perfect gas simulations the upstream conditions before the shock in nondimensional form are

$$\rho = 1, \tag{7.1.1}$$

$$U = M, \tag{7.1.2}$$

$$P = 1/\gamma, \tag{7.1.3}$$

$$E = \frac{\rho U^2}{2} + \frac{P}{\gamma - 1}, \tag{7.1.4}$$

$$T = \frac{\gamma P}{\rho}. \tag{7.1.5}$$

Downstream of the shock in nondimensional form the jump conditions as a function of γ and Mach number are

$$\rho_s = \frac{\rho(\gamma+1)M^2}{(\gamma-1)M^2+2}, \tag{7.1.6}$$

$$P_s = P\frac{\left(2\gamma M^2 - (\gamma-1)\right)}{(\gamma+1)}, \tag{7.1.7}$$

$$T_s = \gamma\frac{P}{\rho}, \tag{7.1.8}$$

$$U_s = U\frac{\left(2+(\gamma-1)M^2\right)}{(\gamma+1)M^2}, \tag{7.1.9}$$

$$E_s = \frac{\rho U_s^{\,2}}{2} + \frac{P_s}{(\gamma+1)}. \tag{7.1.10}$$

The subscript s denotes the shocked region of the domain.

Simulating standing waves in a shock tube for an ideal gas is a relatively straight forward process. Simulating liquids is complicated by the fact that the thermodynamic states are not merely some functional relation of γ, the ratio of specific heats, and Mach number. The setup was further complicated by the need to transform a propagating wave to a standing wave, because the experimental data used for comparison involved a propagating wave. In liquids and solids the symbol "γ_0" refers to the Grüneisen parameter. The upstream conditions before the shock in nondimensional form are

$$\rho = \frac{\rho_0}{\rho_\infty}, \tag{7.1.11}$$

$$U = M, \tag{7.1.12}$$

$$P = \frac{\gamma_0 \rho_0 P_{ref} / \gamma_0 / \rho_0}{\rho_0 {c_\infty}^2}, \tag{7.1.13}$$

$$E = \frac{P_{ref} / \gamma_0}{\rho_0 {c_\infty}^2}, \tag{7.1.14}$$

$$T = \frac{T_0}{{c_\infty}^2 / C_v}. \tag{7.1.15}$$

The term P_{ref} refers to atmospheric pressure of 101.325kPa. Downstream of the shock in nondimensional form the jump conditions are

$$U_s = \frac{\left(U_s - u_p\right)}{c_\infty}, \tag{7.1.16}$$

$$\rho_s = \rho \frac{U}{U_s}, \tag{7.1.17}$$

$$P_i = P + \rho_0 U^2 - \rho_s {U_s}^2, \tag{7.1.18}$$

$$E_s = \left[\left(E\rho + U^2/2 + P/\rho\right) - \left(U_s^2/2 + P_i/\rho_s\right)\right] \Big/ \rho, \tag{7.1.19}$$

$$P_s = \left(\rho_\infty c_0^2\right)\left(x + \left((2s) - (\gamma_0/2)\right)x^2 + s\left(3s - \gamma_0\right)x^3\right) + \gamma_0 E_s \text{ where } x = 1 - \rho_0/\rho_s, \quad (7.1.20)$$

$$T_s = \left(T_0 + \frac{\left(\rho_0 c_\infty^2 E_s - P_{ref}/\rho_0/\gamma_0\right)}{C_v \rho_0}\right) \Big/ \rho_\infty c_\infty^2. \quad (7.1.21)$$

The subscript s denotes the shocked region of the domain. Implementing the boundary conditions for the solids and liquids becomes non trivial; the equation of state must return the same value as the Rankine Hugoniot equations. The Rankine-Hugoniot equations that determine the density, pressure, and energy of the shock state are presented below;

$$\rho_2 = \frac{\rho_1 u_1}{u_2}, \quad (7.1.22)$$

$$P_2 = P_1 + \rho_1 u_1^2 - \rho_2 u_2^2, \quad (7.1.23)$$

$$E_2 = \frac{\rho_1 u_1}{\rho_2 u_2}\left(E_1 + \frac{1}{2}u_1^2 + p_1/\rho_1\right) - \frac{1}{2}u_2^2 + p_2/\rho_2. \quad (7.1.24)$$

Comparing the equations of state for the ideal gas to the Mie-Grüneisen and the pressure relationship obtained from the Rankine-Hugoniot relationships reveals that for the same parameters identical results are not obtainable.

$$P = \rho RT \text{ (Ideal Gas)}, \quad (7.1.25)$$

$$P = k_1 x + k_2 x^2 + k_3 x^3 + \gamma E \text{ (Mie} - \text{Grüneisen)}, \quad (7.1.26)$$

$$P_2 = P_1 + \rho_1 u_1^2 - \rho_2 u_2^2 \text{ (Rankine-Hugoniot)}. \quad (7.1.27)$$

Note that the ideal gas and Rankine-Hugoniot pressure equations are linear while the Mie-Grüneisen in nonlinear.

While undergoing dynamic loading a material follows a thermodynamic path that is described (shocks up) via the Rayleigh line, which is a combination of the continuity and momentum equations, to its final state. If the Rayleigh line is plotted against the

Fanno line, which is a combination of the continuity and energy equations, the two lines will intersect one another twice on an enthalpy versus entropy plot. The two points where they intersect represent the points where the conservation equations are satisfied which are the states before and after the shock.

In pressure-density space the Fanno, Rayleigh, and Mie-Grüneisen equation are;

$$Rayleigh: P_1 = P_0 + \rho_0 U_0 U_0 - \rho_1 U_1 U_1, \tag{7.1.28}$$

$$Fanno: P_1 = U_0(E_0 + \rho_0 U_0 U_0 / 2 + P_0)/U_1 - (\rho_1 U_1 U_1 / 2 + E_1), \tag{7.1.29}$$

$$Mie\text{-}Grüneisen: P_1 = (x + (2s - \gamma_0/2)x^2 + s(3s - \gamma_0)x^3) + \gamma_0 E_1, \quad and \ x = 1 - \rho_0/\rho_1. \tag{7.1.30}$$

Note in Figure 7.1.1 that the Mie-Grüneisen equation intersects the Fanno and the Rayleigh line at the initial and jump states. Figure 7.1.1 shows that in pressure-density space the Fanno and Rayleigh lines overlap and fall on top each other. The Mie-Grüneisen equation of state correctly predicts the shock state pressure and density as well as the upstream far field conditions. The first intersection point shown in Fig. 7.1.1 represents the liquid flowing left to right in the ground state. The second intersection point represents the shocked liquid. The red line represents the peak pressure after the shock determined from the jump conditions. Given that this is a boundary value problem, the boundary values are set by the Rankin-Hugoniot equations. However, if the selected equation of state fails to match the boundary conditions, the result of this mismatch will cause the numeric simulation to diverge. The effect of this error is that throughout the computational domain the equation of state will predict a different pressure for a given strain compared to the boundary conditions. The solution will deviate from the set boundary conditions creating erroneous step functions upstream and downstream of the

shock front which eventually will cause the solution to go awry. It is interesting to reflect on this mismatch as it does not affect a wide host of hydrodynamic formulations. This is because the use of artificial viscosity will dampen disturbances everywhere in the domain.

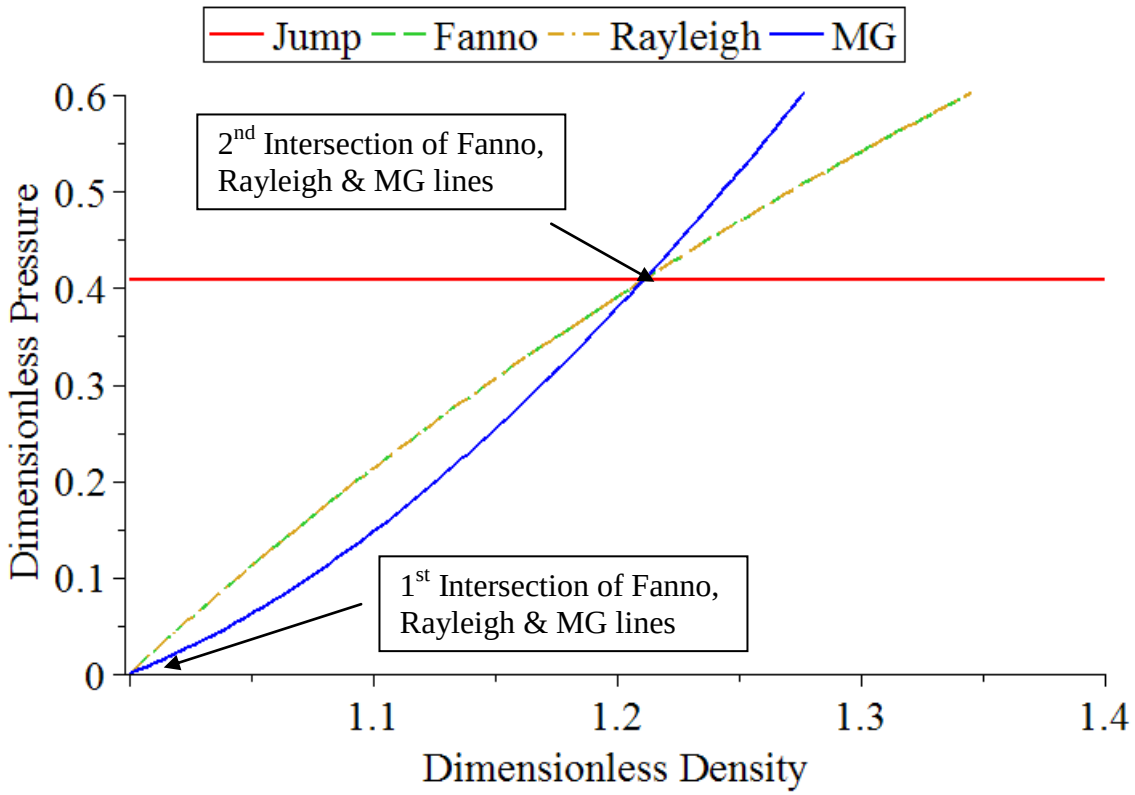

Figure 7.1.1: Dimensionless Pressure vs. Dimensionless Density for the Fanno, Rayleigh, and Mie-Grüneisen equations applied to water. The red line represents the shock (jump) pressure.

This problem results in numeric instability and the solution rapidly degrades because these errors cannot be smoothed out by the available thermodynamic irreversibilities i.e. viscous dissipation and heat conduction. Nor can artificial viscosity negate the time evolved propagation of error. There are several options to correct this problem. One alternative would be to optimize the error associated with the Rankine-Hugoniot intersection with the equation of state. Another alternative is to adjust the Grüneisen parameter used in the Mie-Grüneisen equation of state from the 0.1 value obtained in

open literature to 2.84 [30]. This new value causes the Mie-Grüneisen line to intersect the Fanno and Rayleigh lines at the first and second intersection points which represent the ground and shock state.

For the implementation utilized here the Mie-Grüneisen γ_0 equation (7.1.30), was adjusted so that the equation of state exactly matched the Rankine-Hugoniot equations at the shock locus. Interestingly enough, this turns out to be a unique value, as will be illustrated here. This is common practice for the Mie-Grüneisen equations of state when applied to ideal gases where it is assumed that the ratio of specific heat is equal to the Mie-Grüneisen gamma minus one, $\gamma = \gamma_0 - 1$. This identically insures that the Mie-Grüneisen equation of state matches the Rankine-Hugoniot equations. In fact this assumption, in the absence of a strain potential, reduces the Mie-Grüneisen to a perfect gas model.

In order to insure the equation of state intersects the pre- and post-shock states, we substitute jump conditions into the equation of state and solve for the new gamma, the resulting equation is:

$$\gamma_{00} = \frac{2\left(P(i) - \left(x + 2sx^2 + 3s^2x^3\right)\right)}{\left(-x^2 - 2sx^3 + 2E(i)\right)} \tag{7.1.40}$$

For the specific case investigated here the Grüneisen parameter of 0.15 value obtained in open literature was set to 2.84. This new value causes the Mie-Grüneisen line to intersect the Fanno and Rayleigh lines at a second intersection point which represents the shock state.

The simulation of liquids can become increasingly complicated because dynamic loading may potentially solidify the liquid. If this occurs the physical models currently

included in code and the underlying assumptions made in its formulation are no longer sufficient to capture the physics of the problem. Furthermore, the liquid may solidify upon isentropic release from the shock state. In an effort to mitigate these problems the shock states were carefully chosen to avoid solidification during loading and solidifying upon release is a non issue in this work because the isentropic release phenomena was not studied or taken into consideration. Figures 7.1.2 shows where the dynamic loading process is relative to the saturation dome.

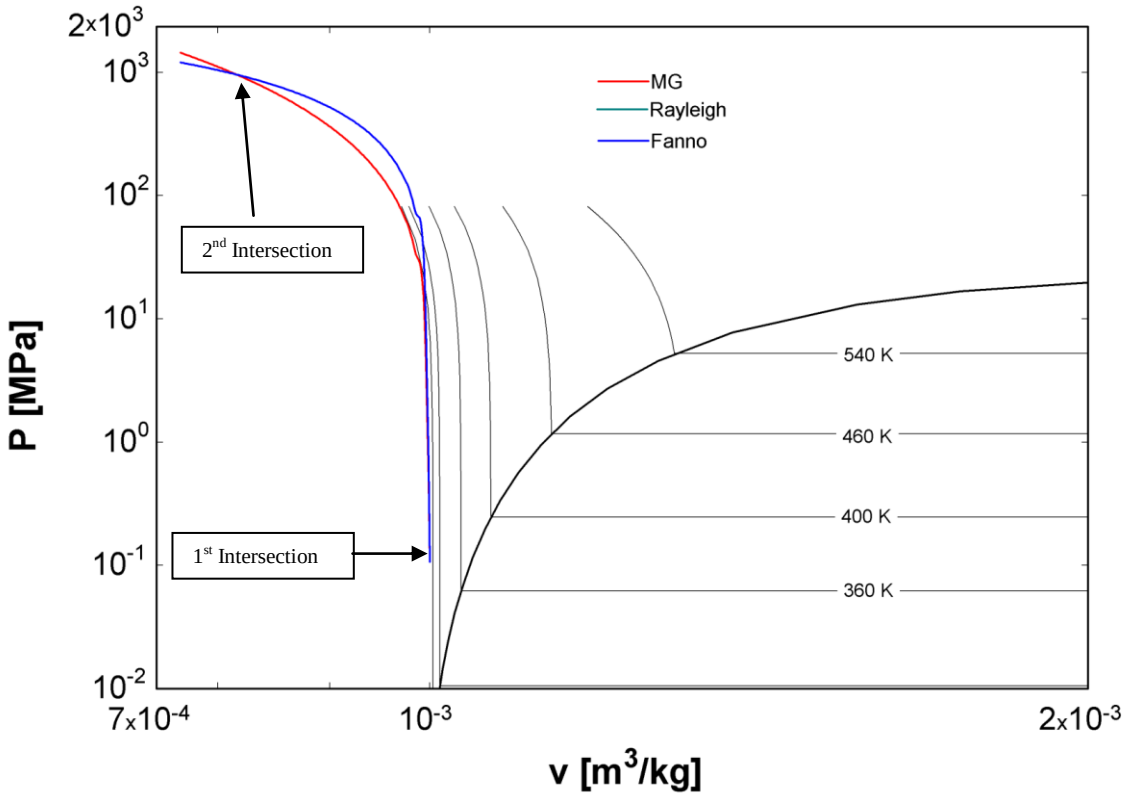

Figure 7.1.2: Pressure vs. Specific Volume for water and includes saturation dome with constant entropy and temperature lines. Note that the Mie-Grüneisen, Fanno line, and Rayleigh line are in the compressed liquid region away from the saturation dome and the solid (ice) space.

For water a low pressure case and a high pressure case were tested. The low pressure case is based on the work of K. Nagayama et al [31]. The data was obtained from a gas gun experiment. Details concerning gas gun experimental setup and

procedures are contained in Chapter 5 of this work. Figure 7.1.3 shows the initial conditions and the two shock conditions tested on a phase diagram of water.

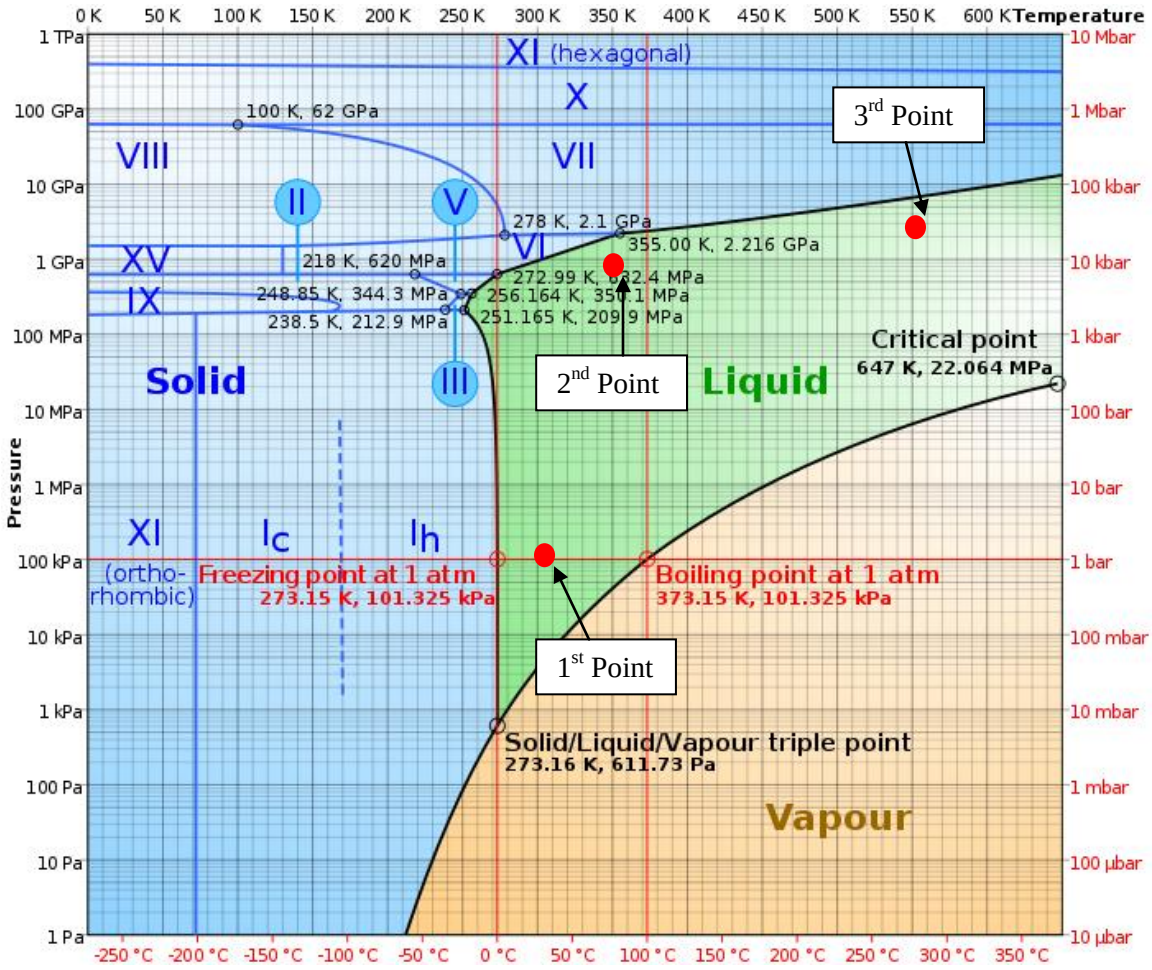

Figure 7.1.3: Phase diagram of water. Point one is the initial condition used for the two water cases. Point two is the shock state for the low pressure water case and point three is the shock state for the high pressure water case. Note all three states are in the liquid phase away from either the solid or vapor space. Graph is taken from Wikipedia (Phase Diagram).

Important parameters related to three water cases, low pressure water, high pressure water, and high pressure water with a larger domain and smaller time step are contained in Table 7.1.1.

Table 7.1.1: Material parameters for water.

	Low Pressure Water	***High Pressure Water***	***High Pressure Water***
γ_{00}	2.8381831	2.9543413	2.9543413
ρ	1000 kg/m^3	1000 kg/m^3	1000 kg/m^3
μ	1.003e-3 kg/m/s	1.003e-3 kg/m/s	1.003e-3 kg/m/s
α	1.00E-05	1.00E-04	1.00E-05
λ	6.2E-10 m	6.2E-10 m	6.2E-10 m
Pr	7.01	7.01	7.01
C_V	1385 J/kg*K	1385 J/kg*K	1385 J/kg*K
C_0	1450 m/s	1450 m/s	1450 m/s
hx	12.5	12.5	25
s	1.99	1.99	1.99
U_P	387.5 m/s	858 m/s	858 m/s

The second high pressure water case is a repeat of the first case with the domain size increased by a factor of two.

In the experiment for the low pressure water case a copper flyer plate with a measured velocity of 412 m/s impacted a PMMA drive plate launching a shock wave into a liquid water sample. The shock pressure and density in the water sample was determined using the jump conditions. The peak pressure is 0.862 GPa and the shock density corresponding to that pressure is 1.211 g/cc. In keeping with the ideal gas analysis the results of applying the Navier-Stokes formulation with the Mie-Grüneisen equation of state will be analyzed using the individual components of the conservation equations. Figure 7.1.4 is graph of the momentum flux versus normalized position. The flux terms represent the right hand side of equations (6.4.1) and (6.5.1). As seen in Fig. 7.1.4 the change in shear stress per unit length is small when compared to the pressure gradient and momentum flux.

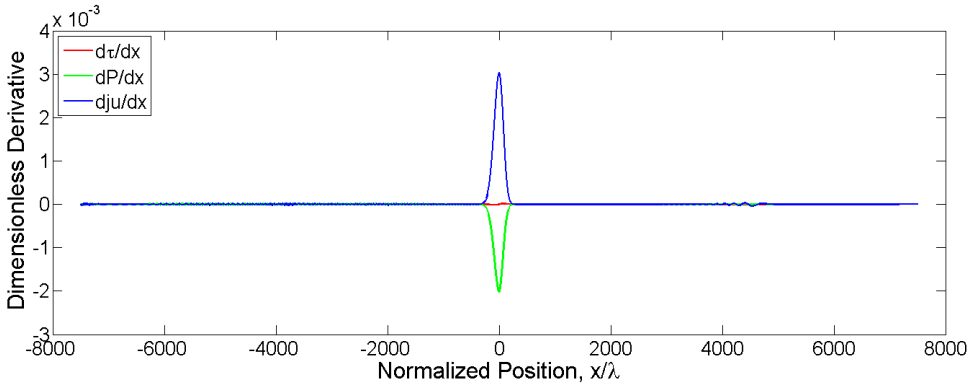

Figure 7.1.4: Dimensionless Derivatives versus Normalized Position for the conservation of momentum equation in water.

The total domain is shown in Fig. 7.1.4 for comparative purposes. While it appears in dimensionless space that this shock front is substantially larger than the ideal gas in fact it isn't because in dimensional space the shock front is smaller for water than for argon gas. Shock front thickness values in units of nm will be presented later in Table 7.2.1. Figure 7.1.5 is a graph of the energy derivatives versus normalized position. Note the significant amount of fluctuations taking place away from the shock front which is centered near zeta zero. At this point in the simulation the high frequency fluctuations have reflected off of the boundaries and are heading back toward the shock front. Plots derived from data obtained earlier in the simulation do not show unobstructed views of the energy flux terms in the shock front. Despite the appearance of the reflected numeric noise in the domain within the shock front the conduction gradient is small relative to the energy associated with viscous shear, momentum and enthalpy.

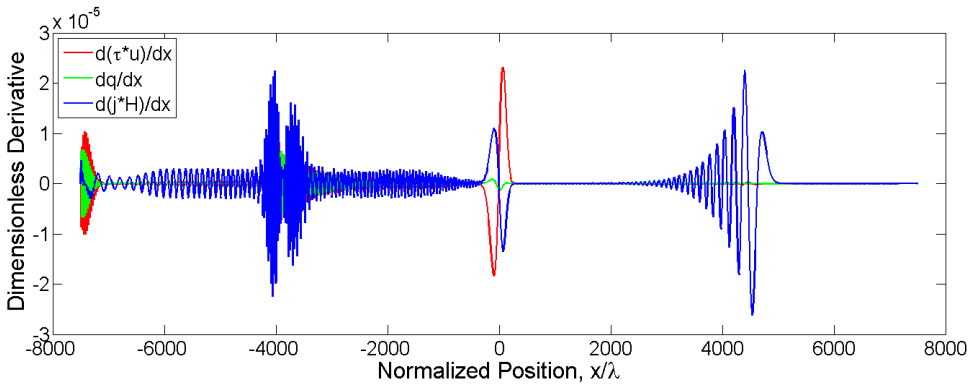

Figure 7.1.5: Dimensionless Derivatives versus Normalized Position for the conservation of energy equation in water.

The dominate term across the entire domain in the conservation of energy equation appears to be the product of j*H where j is the momentum = ρu and H is enthalpy, $H = u + \rho v$. Figure 7.1.6 shows the total energy, defined here as the internal and kinetic, as well as the kinetic and internal energy individually. The results of this plot are similar to the ideal gas plot with the distinction that the kinetic energy dominates upstream of the shock. This occurs because of the transformation of the propagating shock to the standing shock wave where the liquid is assumed to be flowing at a specified speed through the standing shock wave. The relatively large kinetic energy, as compared to the internal energy, creates numeric difficulty when resolving the temperature. Since the internal energy is the difference of two large numbers, which is then used in the denominator of the Temperature calculations, see equation (7.1.21), the result is numeric sensitivity of the Temperature calculations. This variability in Temperature "feeds-back" into the overall simulation through the presence of the conduction term in equation (6.5.1). A way to improve the current technique is to formulate an evolution equation for Temperature directly based on the conservation equations. This would be to take the dot product of the momentum equation with velocity to arrive at an equation for mechanical

energy and subtract this equation from the total energy equation. The result would be an evolution equation for temperature alone ([29], pg 81).

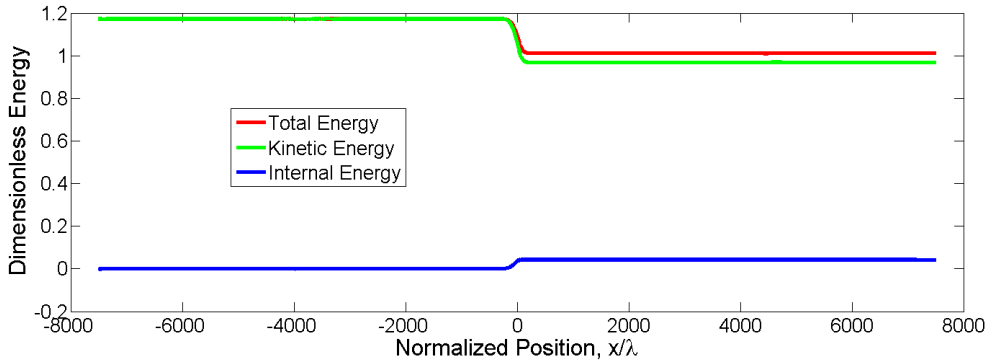

Figure 7.1.6: Total Energy, Kinetic Energy, and Internal Energy versus Normalized Position in water.

Another very interesting characteristic of the energy distribution of the liquid versus the gas, Figure 6.6.1, is that the total energy decreases through the shock for the liquid whereas the total energy increased for the gas. In addition for the gas there was an exchange of dominate energy from kinetic to internal as the material passed through the shock, whereas the liquid is completely dominated by kinetic energy both fore and aft of the shock.

Figure 7.1.7 is a graph of momentum versus normalized position. Note the small scale on the vertical axis. Since momentum must be conserved, even through the shock, changes in momentum represent error (i.e. residual) in the converged solution. This zoomed in view is provided to show how momentum changes through the computational domain. There is variation in the momentum through the shock, centered near zero, which represents residual. Note the large deformation downstream of the shock front, between zeta 4000 and 6000. This wave packet originates as a result of the initial conditions set to a step function, which contains near infinite gradients, and propagates down stream as the shock profile evolves toward a steady state solution. The wave

packet eventually should pass out of the domain. The presence of this disturbance, and the residual near zero, indicates that the solution is either not converged or that the irreversible processes included in the formulation aren't significant enough to eliminate all of the spurious waves (numeric noise) that form in shock front. To some degree this plot which illustrates the momentum is not yet constant, indicates convergence of the solution. For a completely converged solution the dimensionless momentum should be a constant through the shock, from negative to positive infinity.

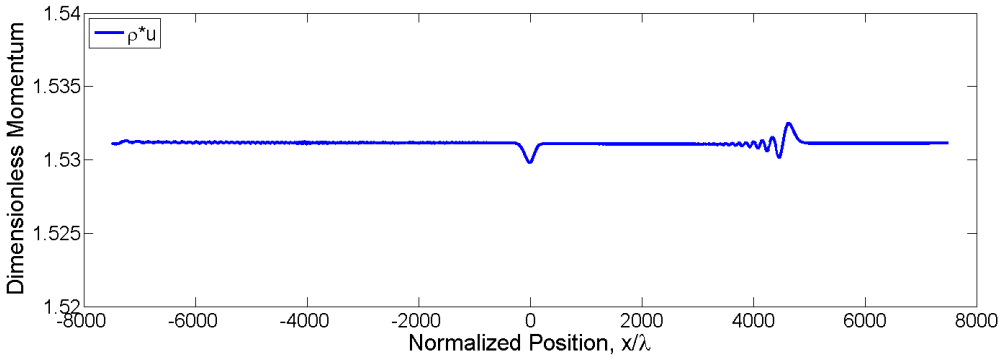

Figure 7.1.7: Momentum versus Normalized Position in water.

Figure 7.1.8 presents the nondimensional shear stress and heat conduction; the heat conduction is small in comparison to the shear stress. This is quite different than the gas where the conduction and shear stress terms were closer in magnitude, see Figures 6.7.1-6.7.3. Recall that change in shear stress is negligible in comparison to the pressure gradient and momentum flux in the conservation of momentum equation.

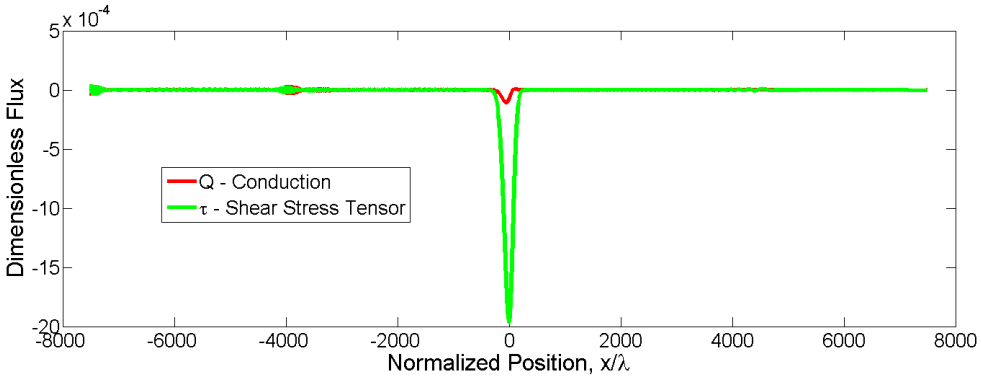

Figure 7.1.8: Conduction and Shear Stress versus Normalized Position in water.

These results for liquid water are in stark contrast to the ideal gas results in that the irreversible terms are small for liquid water as compared to the ideal gas argon. This view point is all supported by the fact that the time step had to be lowered in order for the solution not to go awry and the domain size had to be enlarged as well. These factors made it necessary to run the simulation for a minimum of 50 million iterations and the time step was decreased by one order of magnitude.

Figure 7.1.9 is a plot of the dimensionless density versus normalized position for water, at various snapshots in time. Note in Fig. 7.1.9 that the density values are offset from one another on the vertical axis for improved visualization of the shock evolution and the propagation of wave packets (numeric noise). Not that the wave packets continually move out away from the shock front towards the boundary. The domain size was increased to allow more time for the viscous dissipation and shear stress to reduce these wave packets. If the domain size was not increased then these wave packets would hit the boundary and return to the shock front causing the solution to go awry. The reader should keep in mind that the wave packets, and their suppression, are a complete artifact of the numeric approach taken here. Since the initial condition of the shock was a step

function, something that could not be duplicated experimentally, the resulting wave packets and their evolution could not be observed in nature.

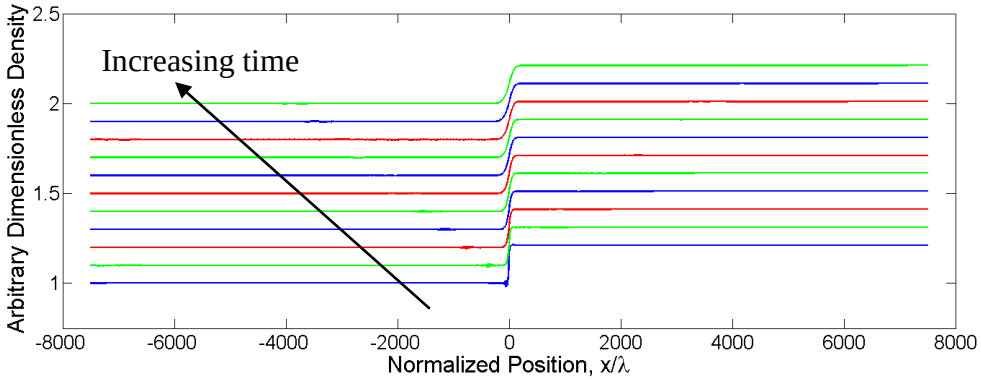

Figure 7.1.9: Density profiles versus Normalized Position in water. Note that in the last profile graphed that the spurious waves are nearly all removed.

In Fig. 7.1.10 momentum is shown to be affected by the domain size.

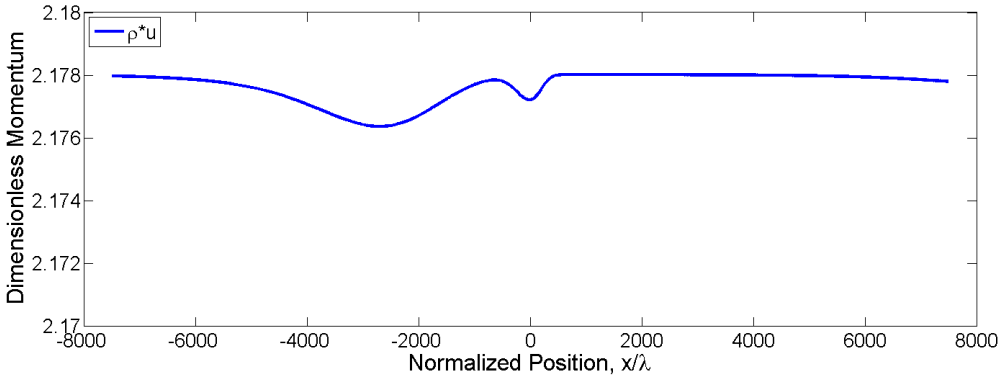

Figure 7.1.10: Momentum versus Normalized Position in water. Note the disturbance to the left of the shock front which is located at zero.

Figure 7.1.10 indicates that a spurious wave packet has reflected off of the left boundary is now returning toward the shock wave. In order to clarify what the disturbance is the time evolved density profile is presented next in Fig. 7.1.11.

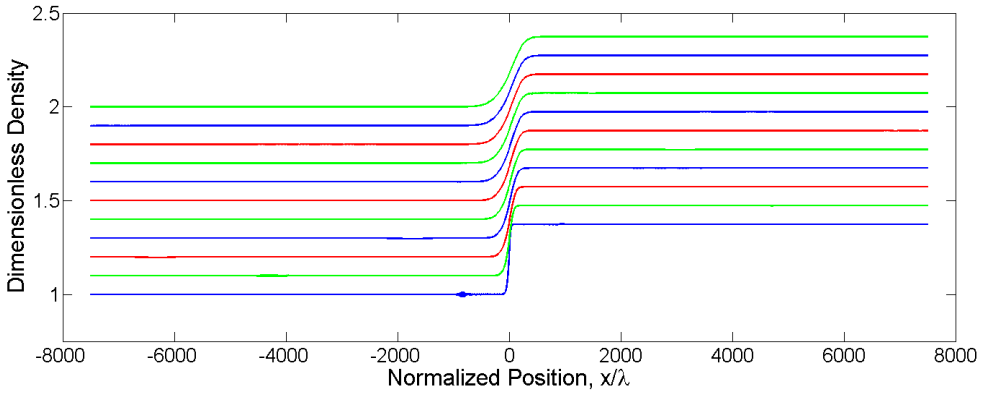

Figure 7.1.11: Density profiles versus Normalized Position in water. Note that in the last profile graphed that the spurious waves are nearly all removed.

While it appears that all the numerical noise is eliminated from the last density profile shown (top) in Fig. 7.1.11 that is not the case if one zooms in on the last profile. Notice that the spurious waves are moving back and forth in the domain until it appears that more noise is being generated partially though the simulations. This simulation was carried out for 50 million iterations just as the lower pressure case was. It appears that while a lower time step can be used to resolve this shock front care must be take to halt the simulation at an appropriate time so that the spurious waves don't have time to reflect back and obscure the results. Finally it appears that it is best to use a slower time step in order give time for the spurious wave packets to dissipate before they encounter either boundary.

Figure 7.1.12 is graph of total energy, kinetic energy, and internal energy versus normalized position. As expected there is a larger increase in the internal energy as opposed to the lower pressure case.

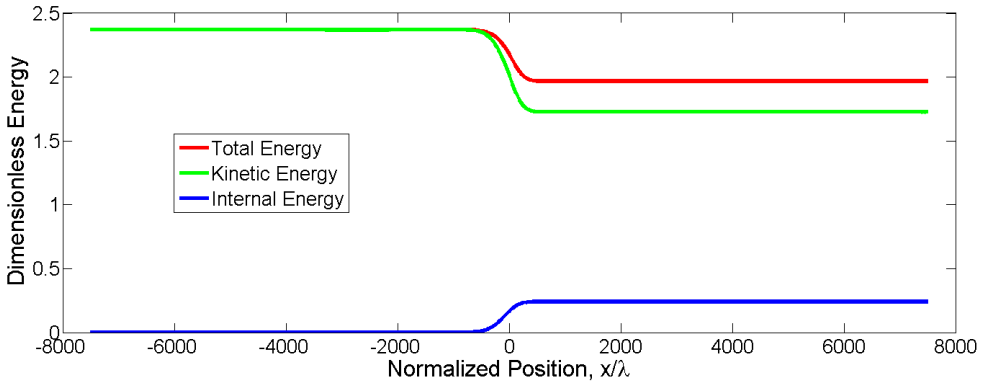

Figure 7.1.12: Total Energy, Kinetic Energy, and Internal Energy versus Normalized Position in water.

Figure 7.1.13 shows a significant increase in the conduction term, however when compared to other terms in the energy equation conduction remains small.

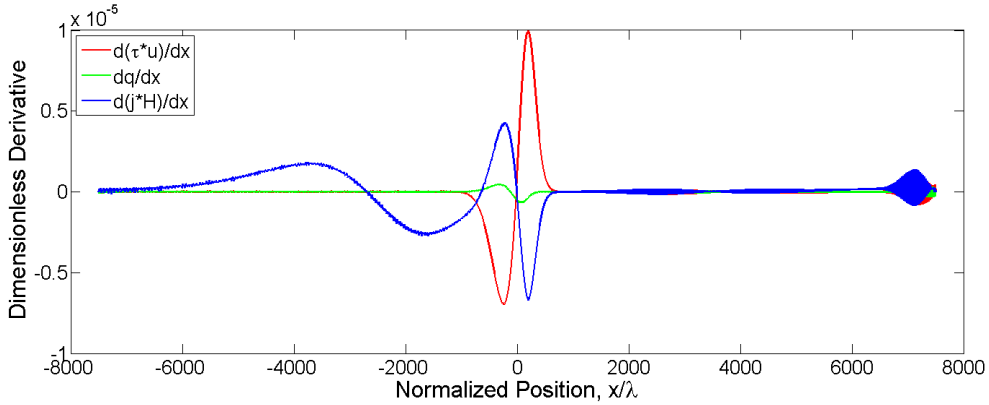

Figure 7.1.13: Dimensionless Derivatives versus Normalized Position for the conservation of energy equation in water.

Figure 7.1.14 shows that as velocity is increased and subsequently there is a larger change in pressure and momentum flux that the shear stress becomes relatively smaller. Figure 7.1.15 illustrates that at high pressures conduction remains relatively small compared to the shear stress tensor.

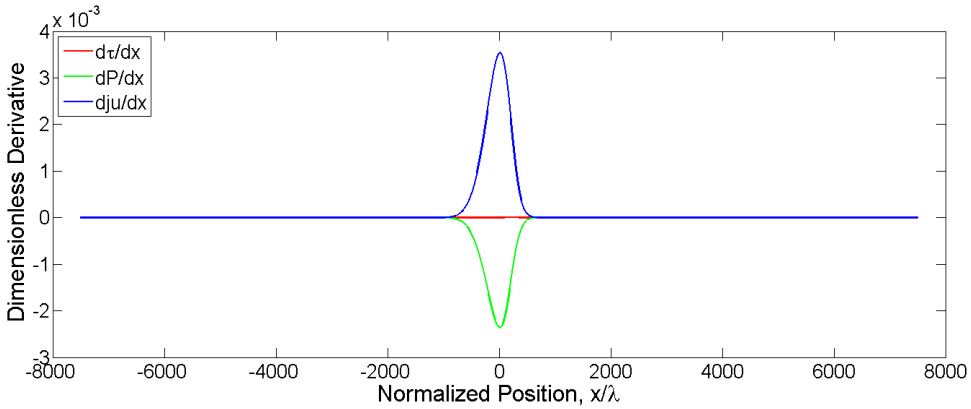

Figure 7.1.14: Dimensionless Derivatives versus Normalized Position for the conservation of momentum equation in water.

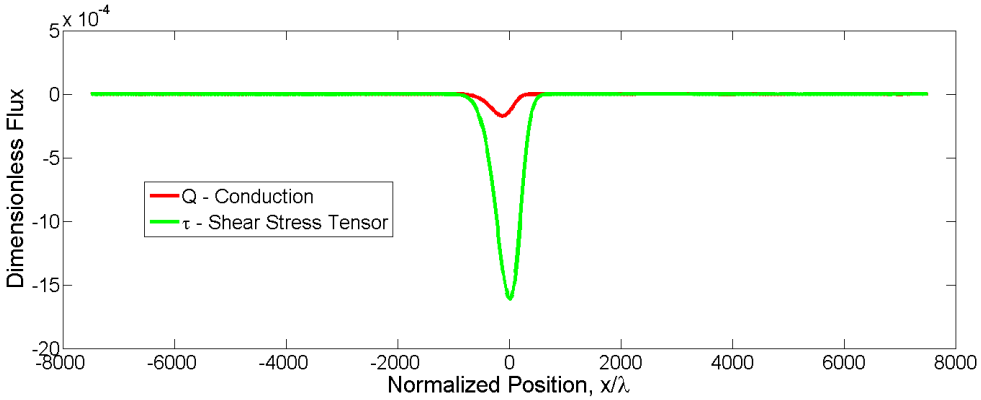

Figure 7.1.15: Conduction and Shear Stress versus Normalized Position in water.

The effect of the domain size and time step is further examined by doubling the domain size and repeating the high pressure simulation with a smaller time step. In Fig. 7.1.16 the conservation of momentum graph shows the spurious waves moving away from the shock front towards the boundaries.

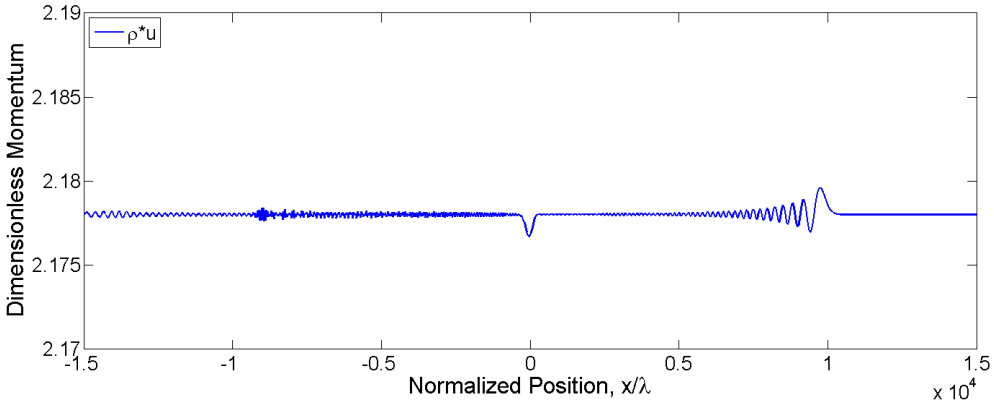

Figure 7.1.16: Dimensionless Momentum versus Normalized Position for water with increased domain size.

This point is reinforced in Fig. 7.1.17 - Fig. 7.1.19 which show the time evolved arbitrary dimensionless density, dimensionless pressure, and dimensionless temperature profiles for water with increased domain size.

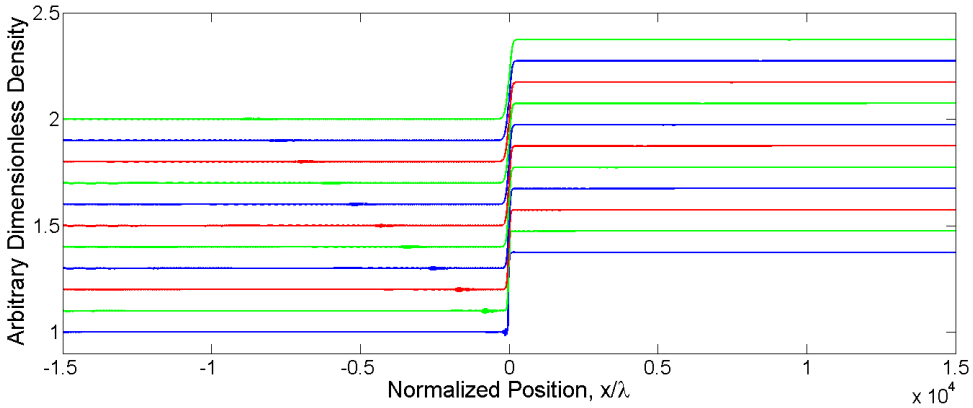

Figure 7.1.17: Arbitrary Dimensionless Density versus Normalized Position for water with increased domain size.

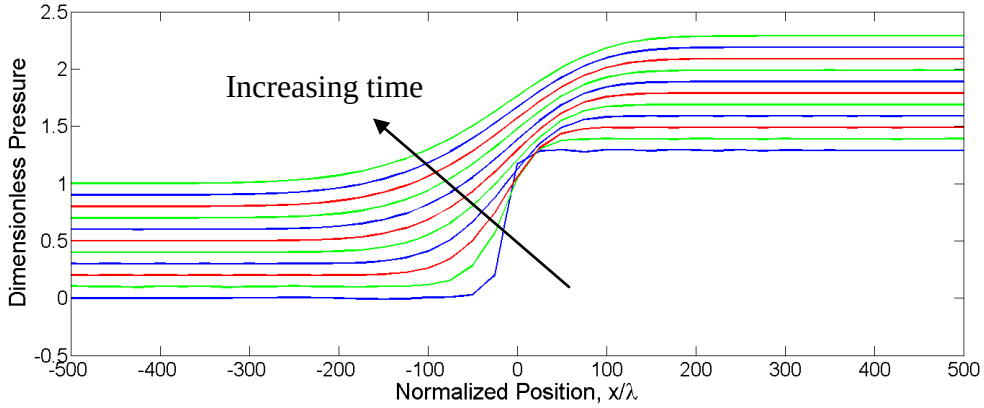

Figure 7.1.18: Dimensionless Pressure versus Normalized Position for water with increased domain size.

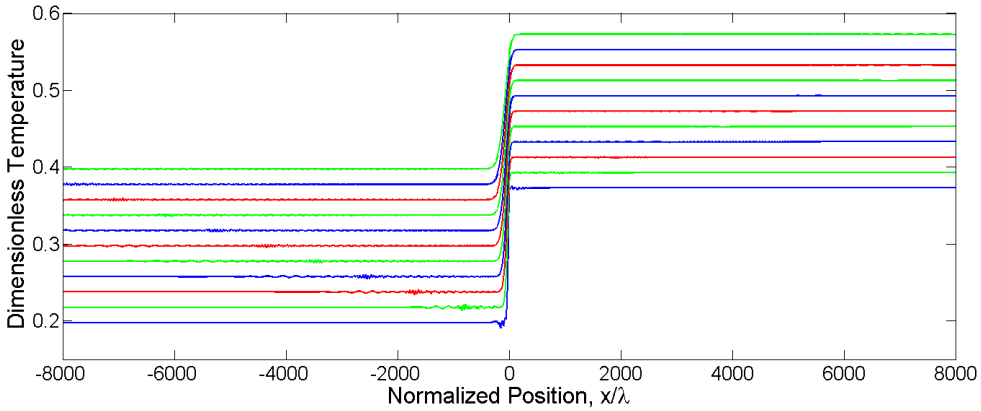

Figure 7.1.19: Dimensionless Temperature versus Normalized Position for water with increased domain size.

Note in Fig. 7.1.17 – Fig. 7.1.19 that the dimensionless domain size has been increased from a value of 7500 to 15000. In the particular graphs the domain size may have been changed in order to maximize the viewing of the spurious waves moving out towards the boundaries. With the increased domain size and smaller time step the spurious waves appear to be diminishing in magnitude as they propagate out towards the boundaries and in case of the last presented profiles in Figs. 7.1.17 – 7.1.19 seem to have disappeared all together. Figures 7.1.20 – 7.1.23 present the individual derivative contributions for the conservation of momentum and energy along with the relative contributions of the

viscous shear tensor and heat conduction terms and the kinetic, internal and total energy summation as affected by domain size.

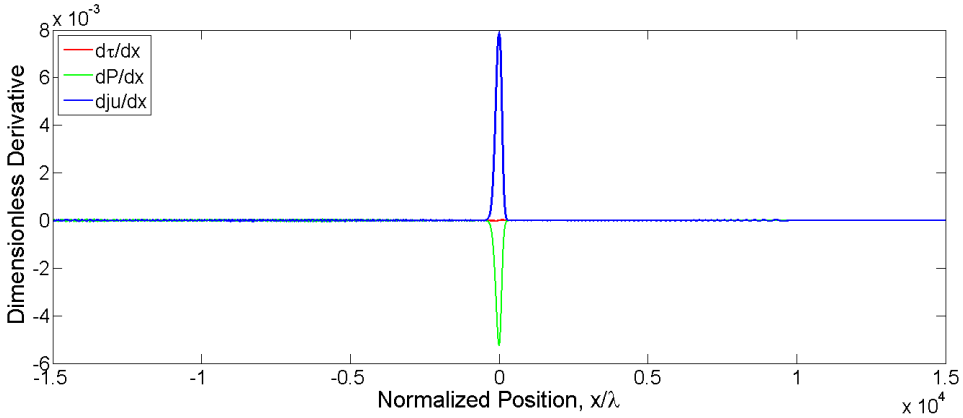

Figure 7.1.20: Dimensionless Derivative versus Normalized Position for the conservation of momentum for water with increased domain size.

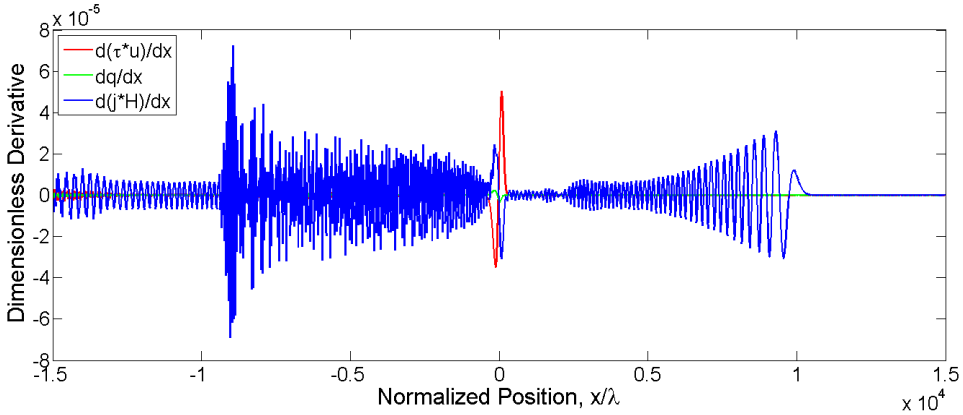

Figure 7.1.21: Dimensionless Derivative versus Normalized Position for the conservation of energy for water with increased domain size.

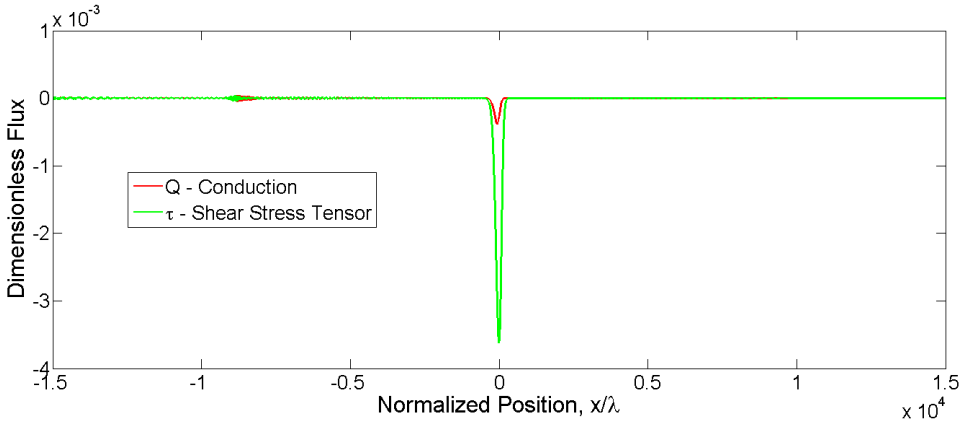

Figure 7.1.22: Heat Conduction and Shear Stress versus Normalized Position for water with increased domain size.

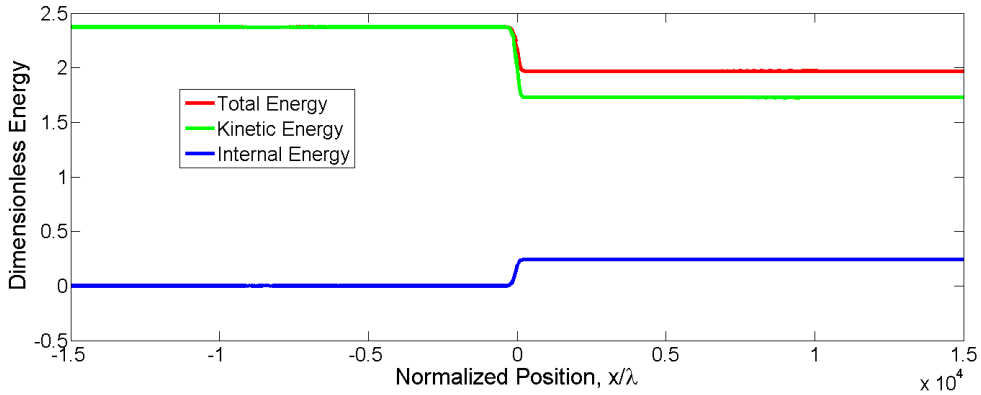

Figure 7.1.23: Total Energy, Kinetic Energy, and Internal Energy versus Normalized Position for water with increased domain size.

Note that by increasing the domain size and decreasing the time step that the high frequency fluctuations, spurious waves, numeric noise, and negative feedback are minimized. However, care must be taken to insure that resolution throughout the domain remains relatively high to reduce the chances of steep gradients forming at the boundaries or around the shock front.

Figure 7.1.24 compares the experimental pressure signature to the pressure signature predicted by the NS code. The data presented here comes from flyer plate experiments performed by Morley [32]. The data was obtained from Manganin gage trace but was converted to a profile in space by multiplying by the shock speed of water, 3158 m/s. The particle speed in the water sample is 858 m/s as compared to 387.5 m/s in the lower pressure case discussed earlier. The dimensionless experimental pressure signature was nondimensionlized in the same way as the computational pressure signature, namely dividing the dimensional pressure signature by the far field dynamic pressure ($\rho_\infty C_\infty C_\infty$). The far field dynamic pressure is found by multiplying the far field density of water 1000 g/m^3 times the far field sound speed squared which is 1450 m/s. The experimental pressure signature is immediately relieved upon reaching its peak

pressure. The experimental pressure signature shown in Fig. 7.1.24 has been shortened because where it currently ends another reshock starts. Note that the peak pressure predicted using the NS code is an under prediction of the experimental peak pressure which is a signature trace of a reshock of the water sample.

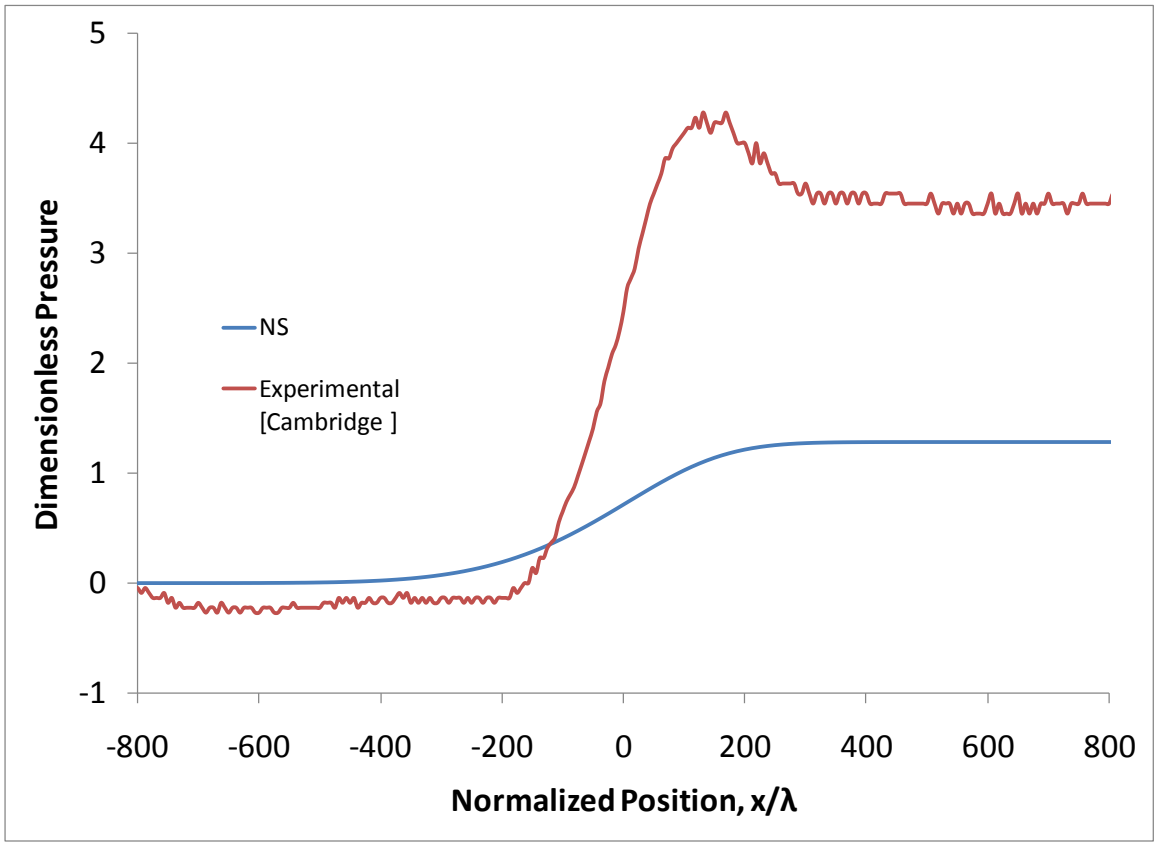

Figure 7.1.24: Experimental pressure signature versus computational pressure signature generated with NS code for high pressure water case.

Table 7.1.1 compares the shock front thickness values obtained from experiments with those obtained from numeric simulations. The numeric simulations under predicts the shock front thickness in water at high pressure. The pressure signature for the low pressure case was not available therefore the shock thickness could not be determined. Vogel and Busch [33] observed shock front thicknesses values between 200-300 μm, which is in good agreement with the 253 μm value obtained in this work. The predicted shock thickness value of 868 nm using the NS code is narrow in comparison to what is

observed experimentally. There could be several reasons for this discrepancy. The gas simulations exhibited sensitivity of shock thickness to the dynamic viscosity (i.e. shear viscosity); whereas the viscosity for the water simulations was held constant. Although the dynamic viscosity for liquids exponentially decreases as a function of temperature, the functionality of the liquid viscosity at these pressures and temperatures is not well understood. The dynamic viscosity of water becomes super critical near 800 K. In addition, the formulation utilized here invoked the hypothesis that the ratio of the bulk viscosity to the shear viscosity is 4/3, whereas at standard pressure and density, this ratio is more like three. Again the validity of this assumption is not well understood for the thermodynamic states of interest here.

Table 7.1.2: Shock front thickness values in water.

Water	*SFT-Simulations*	*SFT-Experiment*	*Entropy-Simulations*	*Entropy-Calculations*	*Nist Data*
Low Pressure	310 nm	NA	1.71 KJ/Kg*K	0.879 KJ/Kg*K	0.712 KJ/Kg*K
High Pressure	868 nm	253 μm	1.51KJ/Kg*K	0.230 KJ/Kg*K	NA

7.2 Introduction – Solids

The solid used in this work is porous silica. Porous silica of densities 0.1 g/cc, 0.25 g/cc, and 0.77 g/cc will be studied. This material was chosen because it represents a transitional material between liquid and solid; transmitted waveforms do not exhibit HEL behavior and granular materials have strain rate shear stress. With regard to experimental measurements, a highly porous material exhibits relatively long structured compaction wave forms. However, the mechanisms for irreversibilities in granular materials are more complicated as compared to the liquids. These mechanisms include not only heat conduction and some viscous shear stress, through either bulk mechanics or localized plastic flow, but also inter-granular friction and grain fracture.

The data and material parameters used here were determined through experimental work by Borg et al [4, 25].

Table 7.2.1: Material parameters for porous Silica.

	Silica 65% Porosity	***Silica 89% Porosity***	***Silica 95% Porosity***
γ_{00}	0.1918117	0.7240199	0.1016222
ρ	100 kg/m^3	250 kg/m^3	770 kg/m^3
μ	4.40E-5 kg/m/s	1.10E-4 kg/m/s	3.39E-4 kg/m/s
α	1.00E-07	1.00E-07	1.00E-05
λ	1.61E-10 m	1.61E-10 m	1.61E-10 m
Pr	0.91	2.27	7.00
C_V	86.2 J/kg/K	86.2 J/kg/K	86.2 J/kg/K
C_0	121 m/s	97 m/s	1070.9 m/s
hx	0.25	0.25	0.25
s	0.9736	1.2509	0.4045
U_P	704 m/s	770 m/s	934 m/s

The highest shot velocities available for the three densities will be used in the simulations presented in this work. It is of interest to this work to determine if the NS formulation can numerically resolve the shock front a distended material. It is assumed that porous silica has no material strength like a liquid until it is fully consolidated thereby eliminating the need to include a strength of material model into the formulation. The simulations of the 0.1 g/cc and 0.25 g/cc samples were run out to 75 million iterations, while the 0.77 g/cc silica sample was stopped at 50 million iterations because it was assumed that either convergence or reflected noise from boundaries would have arrived to distort the shock front because the time step (α) used was two orders of magnitude larger than in the two cases. The results indicate a high sensitivity to the time step size. If the time step used was too large the solution would quickly go awry because the gradients would not be resolved within the given time step. If the time step chosen was

too small the number of iteration needed for convergence would make the particular simulation impractical.

Figure 7.2.1 is a graph of dimensionless density versus normalized position for porous silica of density 0.1 g/cc, 0.25 g/cc, and 0.77 g/cc. For the most distended case, porous silica with a density of 0.1 g/cc, high frequency disturbances appear in the density profile as the solution converges. Note in Fig 7.2.1 (b) the appearance of large waves upstream of the shock front. They appear to be moving to the left and increasing in number. These waves are not thought to be spurious waves or numerical noise because of their size and their duration in the computational zone. It also appears that they are beginning to immerge downstream of the shock front leading edge. In Fig 7.2.1 (c) the spurious waves seen upstream of the shock dissipate as they move towards the left boundary.

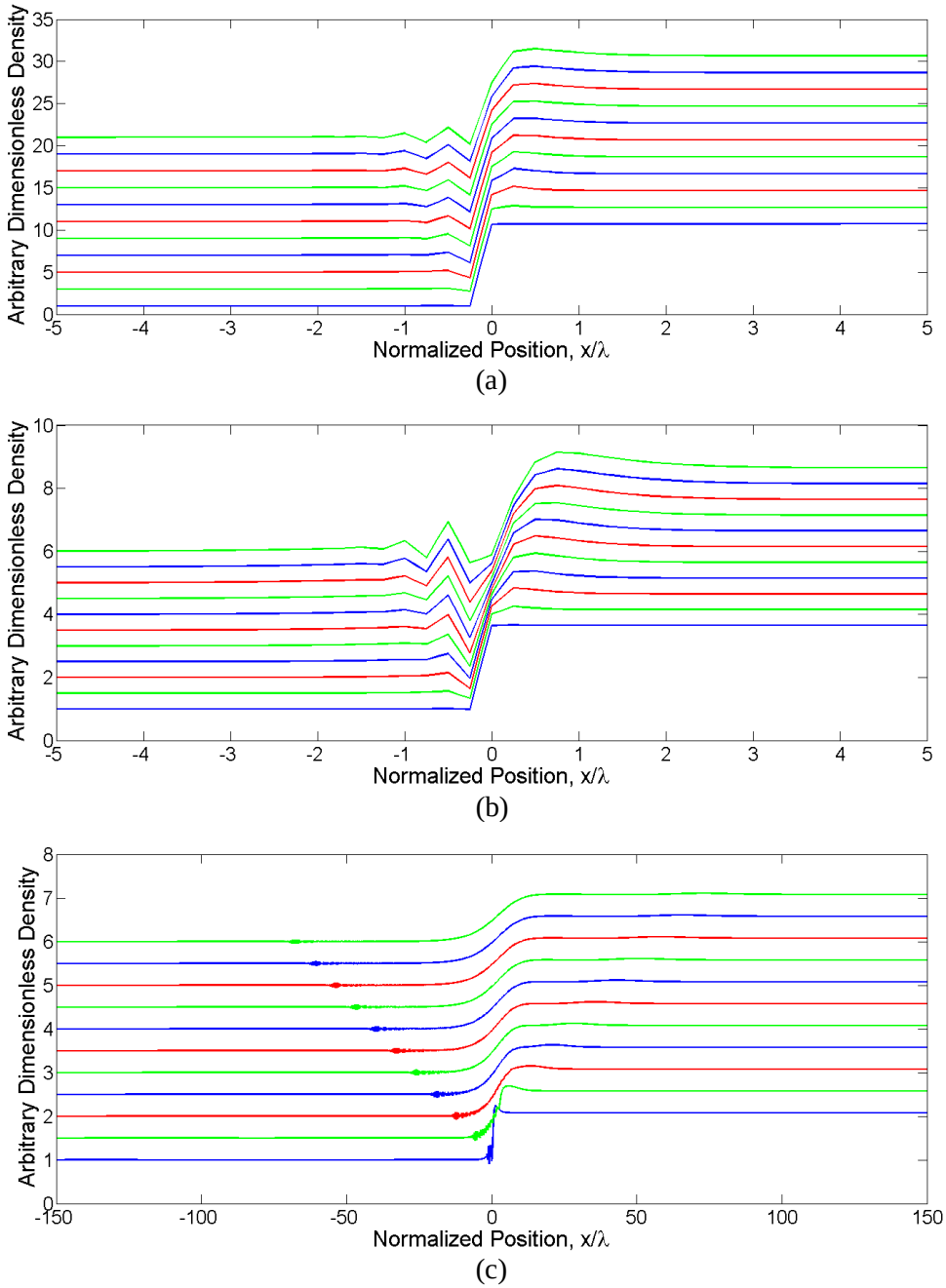

Figure 7.2.1: Dimensionless Density versus Normalized Position for porous silica with a density of 0.1 g/cc (a), 0.25 g/cc (b), and 0.77 g/cc (c).

Figure 7.2.2 shows the evolution of the dimensionless pressure profile for all three silica samples is smoothing out and becoming less steep as the simulations progress in time. Note that for two of silica samples densities 0.1 g/cc and 0.25 g/cc respectively that the pressure values are initially non physical because the code is predicting negative

pressures. As the simulations progress the non physical negative pressure profile is eliminated over a finite number of iteration until the pressure profile behaves as expected, which is a smooth transition from low pressure to high pressure. Porous silica with a density of 0.77 g/cc behaves correctly replicating fully consolidated behavior.

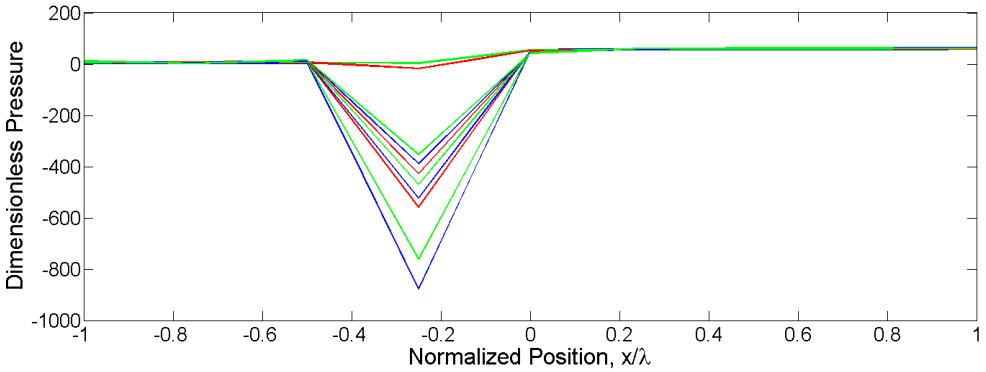

(a)

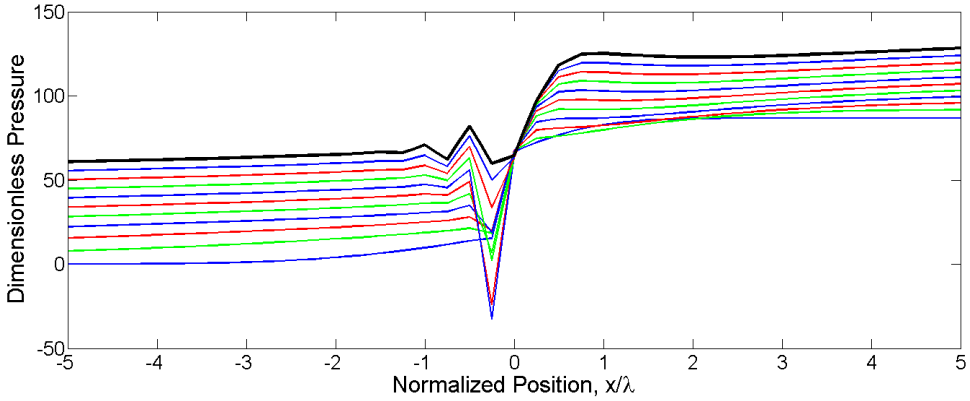

(b)

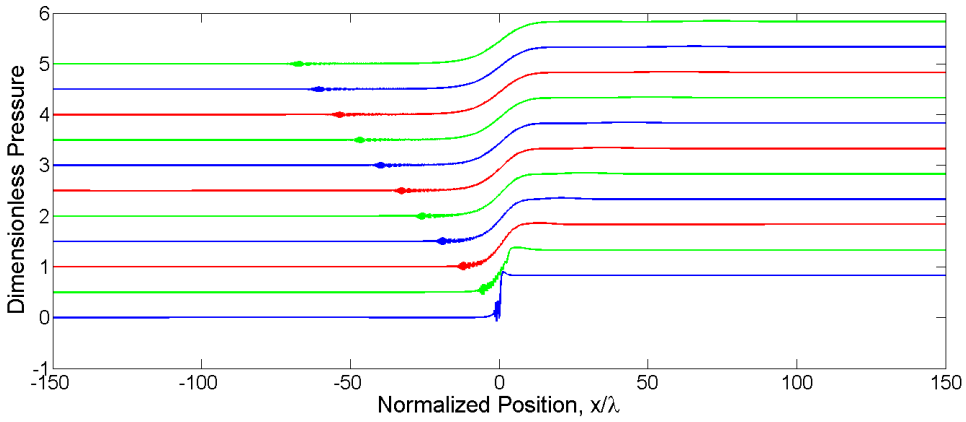

(c)

Figure 7.2.2: Dimensionless Pressure versus Normalized Position for porous silica with a density of 0.1 g/cc (a), 0.25 g/cc (b), and 0.77 g/cc (c).

Figure 7.2.3 shows the time evolution of the temperature profile for all three densities used in this work. Note in Fig 7.2.3 in both (a) and (b) that the vertical curve is the temperature profile of the first iteration of the simulation. As can be seen in Fig 7.2.3 the temperature profile continually improves during the simulation forming a gradual slope. It appears from studying the results presented in Fig 7.2.3 that the solution improves with respect to temperature regardless of the initial porosity. Figure 7.2.3 (c) appears different because a larger offset was used in graphing the data so the subsequent iterations would appear above the initial solution instead of overlapping like in (b) and (a). The overlapping technique used in Fig 7.2.3 (a) and (b) show in a more obvious manner the change in the slope of the shock rise for temperature. The benefit of using a larger offset like the one used in Fig 7.2.3 (c) is that it permits visualization of the wave packets. Notice in Fig 7.2.3 (c) that no wave packets appear either upstream or downstream of the shock front. This seems to indicate that the 0.77 g/cc sample behaves more like fully consolidated silica and less like the more porous samples tested in this work. A viable solution is more easily obtained for the less porous samples of silica such as the 0.77 g/cc case and more slowly for the most distended case which is the 0.1 g/cc case.

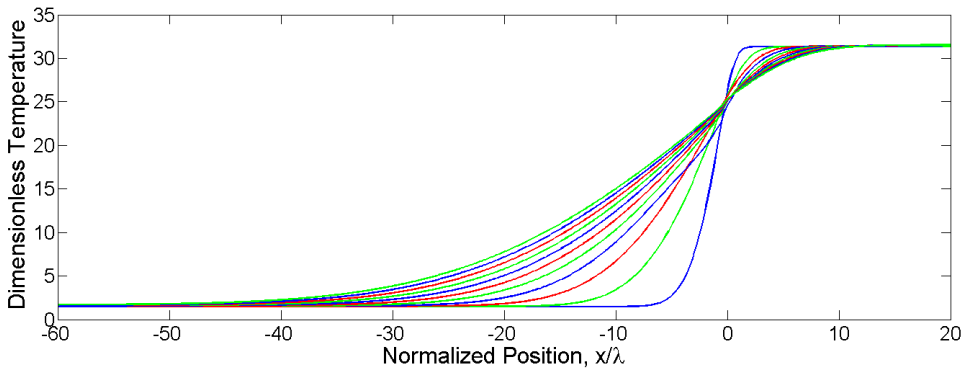

(a)

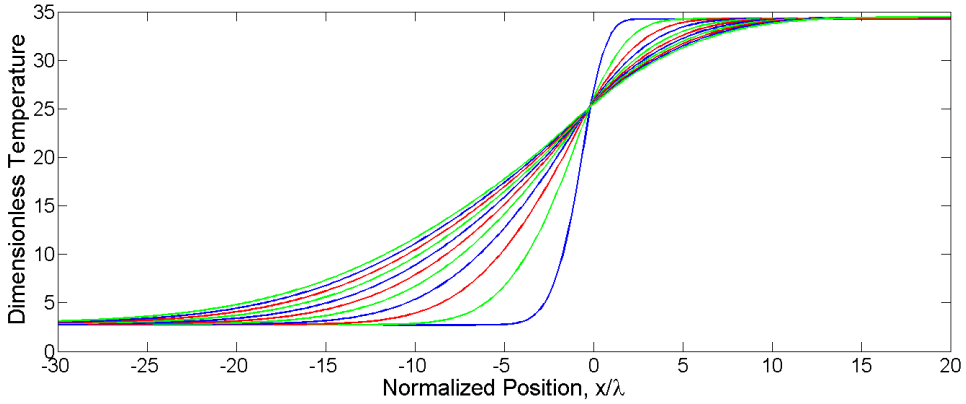

(b)

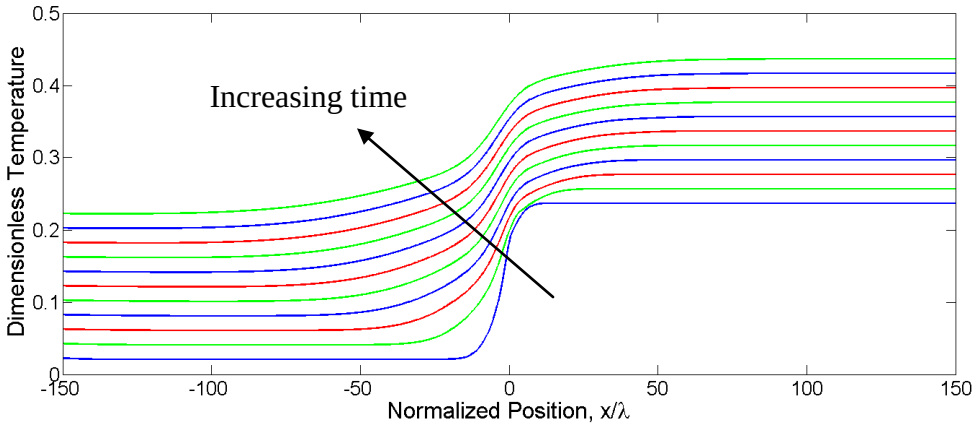

(c)

Figure 7.2.3: Dimensionless Temperature versus Normalized Position for porous silica with a density of 0.1 g/cc (a), 0.25 g/cc (b), and 0.77 g/cc (c).

The next graph Fig. 7.2.4 is for momentum which is a good indicator for when the solution has converged. Note in Fig 7.2.4 that the steepness of the momentum reduces as initial porosity is decreased. In Fig 7.2.4 (c) that in the shock front which is centered near

zero in dimensionless space that the momentum change across the shock is small. However, there is a large displacement in the downstream field in Fig 7.2.4 (c). The appearance of a large wave downstream of the shock front and a smaller wavelet upstream of the shock are indicative of wavelets propagating out towards the boundaries. These waves need to be studied more because their appearance was not expected based on the momentum profile in Fig 7.2.4 (a) and (b), which seem like they are either fully converged or nearly converged solutions because the absence of spurious waves (b) or the minimization of such waves.

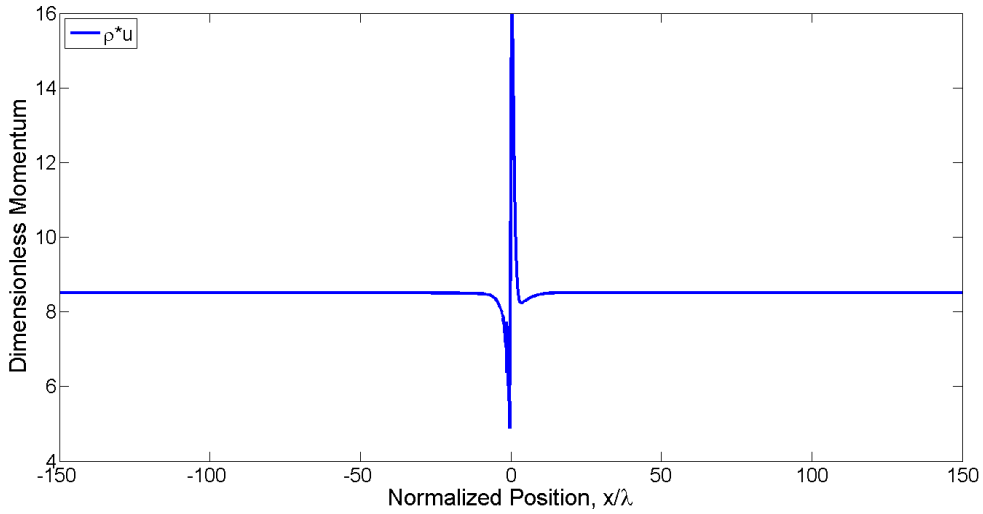

(a)

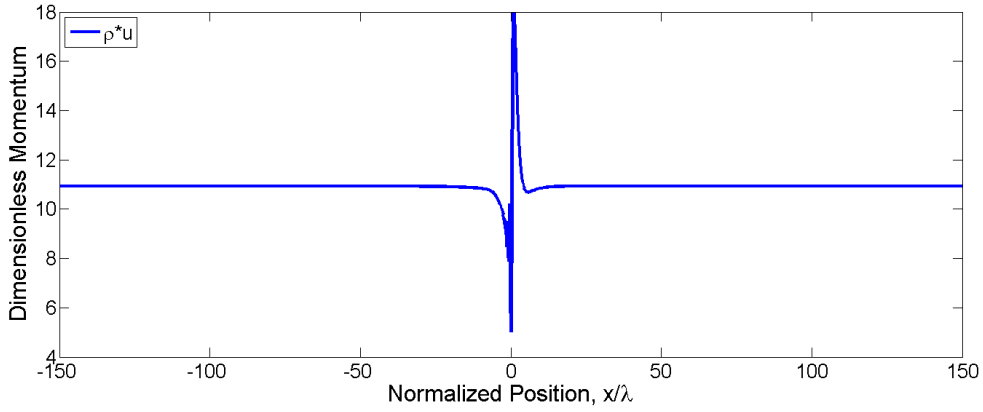

(b)

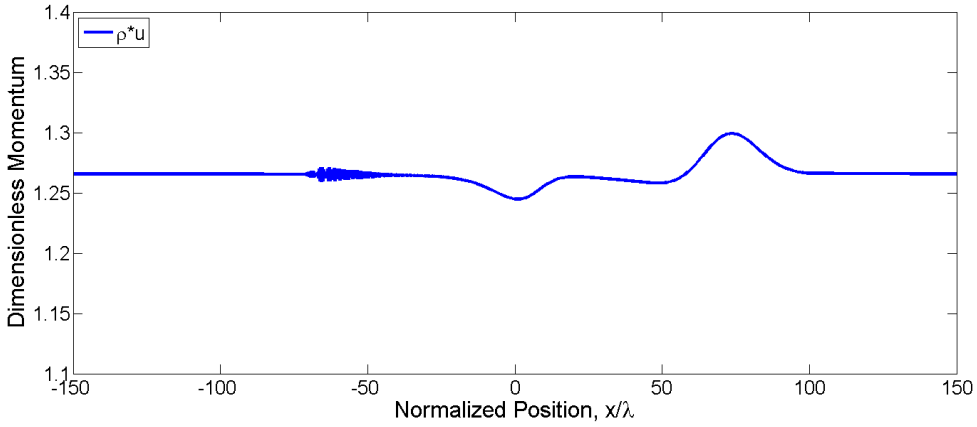

(c)

Figure 7.2.4: Dimensionless momentum versus normalized position for porous silica with a density of 0.1 g/cc (a), 0.25 g/cc (b), and 0.77 g/cc (c).

In order to shed some light the appearance of these waves in Fig. 7.2.4 (c) graphs of the total energy, momentum and energy fluxes will be presented. Figure 7.2.5 graphs the total energy of the three densities studied. The steep change in momentum depicted in Fig. 7.2.4 (a) and (b) are replicated here in Fig. 7.2.5 (a) and (b). The smoothness of Fig. 7.2.4 (a) and (b) are replicated in Fig. 7.2.5 (a) and (b) away from the shock front. It appears that the solution obtained for porous silica with a density of 0.77 g/cc may not be fully converged at 50 million iterations. The wavelets seen in Fig. 7.2.4 (c) are less pronounced in the total energy graph of Fig. 7.2.5 (c). The magnitude of waves in dimensionless space suggests that these waves can be attributed to mere numeric noise or reflected noise that is now geometrically increasing. Subsequent investigation and plotting of the solution as it evolved shows that these waves present in Fig. 7.2.5 (a) and (b) are caused by numeric instability originating within the shock and growing as the solution progresses. Merely rerunning the solution may eliminate these waves; however when considering the time step and grid spacing used to obtain these solutions it may be impractical to wait for these waves to move away from the shock front. It becomes impractical because the waves may be generated within the shock front itself, which means a wavelet would always be present and eventual the wavelets would reflect back into the domain at the boundary causing the solution to go awry. Instead an entire new setup such as material parameters used in the simulation, the domain size and time step used may have to be adjusted. Many of the parameters used in the simulation of the porous silica are not available such as Prandtl number and viscosity, because these parameters are used in reference to fluids. Therefore density weighted averaging was used to obtain the necessary values. Since these values are only present in the shear

stress tensor and heat conduction terms and only the change in these quantities is used in the simulations there relative importance is thought to be small.

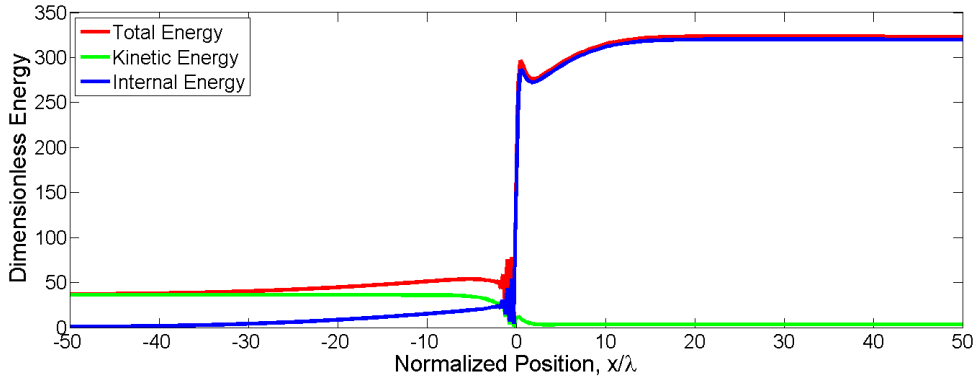

(a)

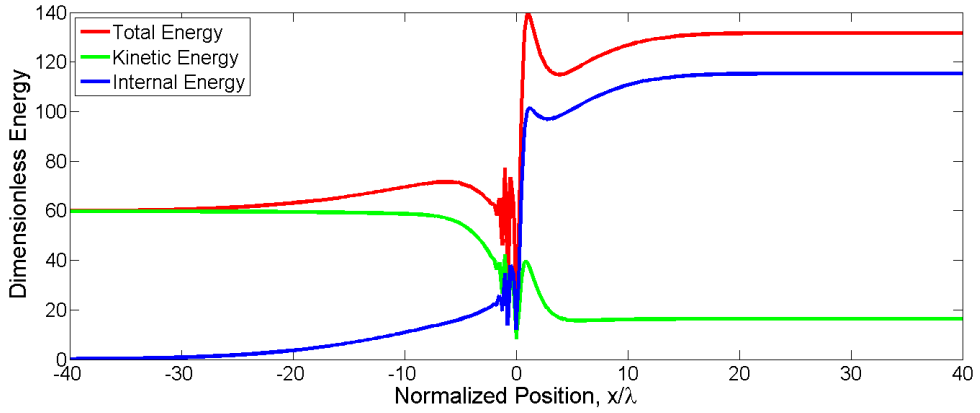

(b)

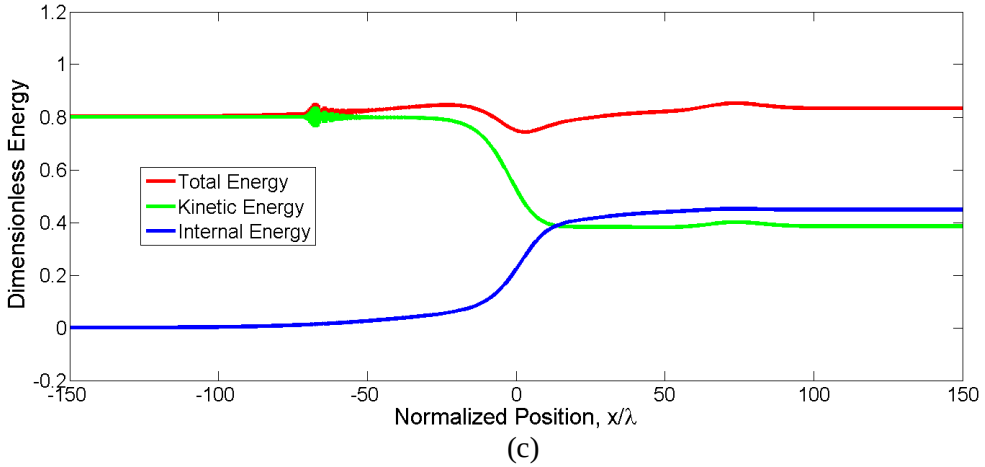

(c)

Figure 7.2.5: Dimensionless Energy versus Normalized Position for porous silica with a density of 0.1 g/cc (a), 0.25 g/cc (b), and 0.77 g/cc (c).

Figure 7.2.6 and Fig. 7.2.7 show the individual contributions to the momentum and energy conservation equations.

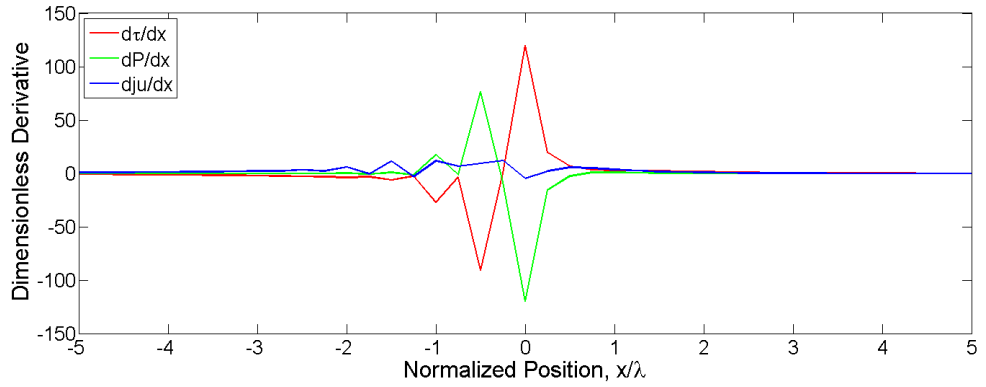

(a)

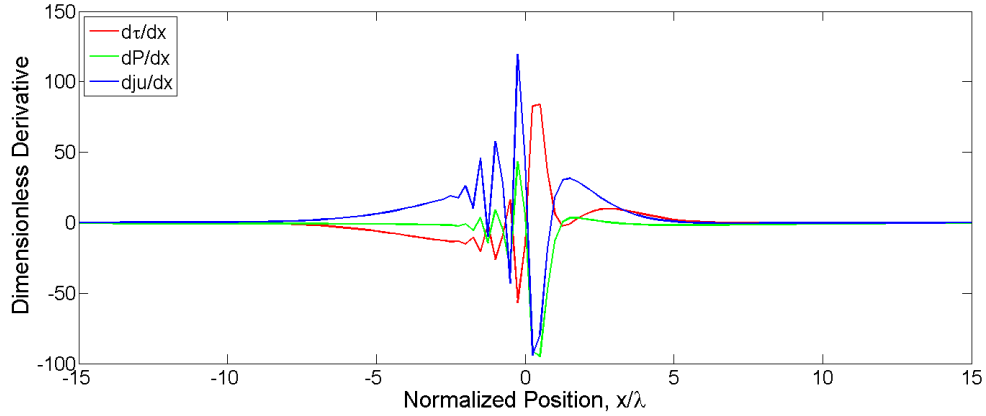

(b)

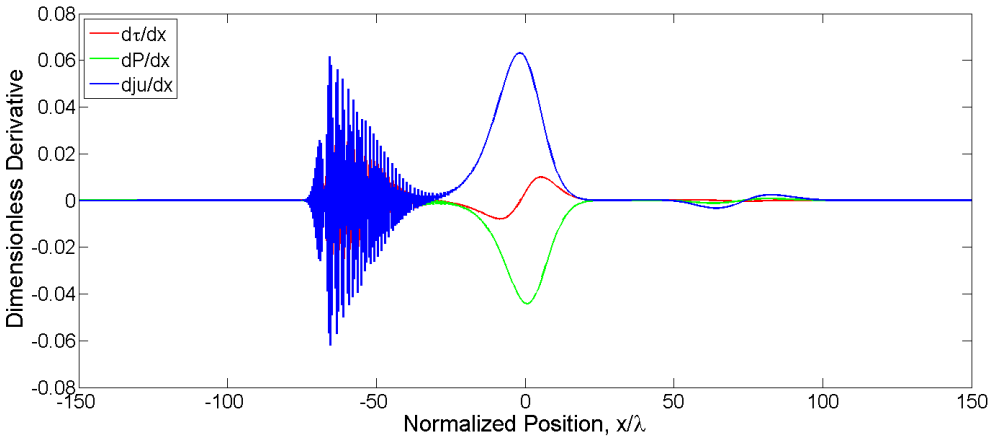

(c)

Figure 7.2.6: Dimensionless Derivative versus Normalized Position for the momentum equation applied to porous silica with a density of 0.1 g/cc (a), 0.25 g/cc (b), and 0.77 g/cc (c).

Note in Fig. 7.2.6 and Fig. 7.2.7 that the magnitude of the derivatives are orders of magnitude larger for the 0.1 and 0.25 g/cc cases as opposed to the 0.77 g/cc case.

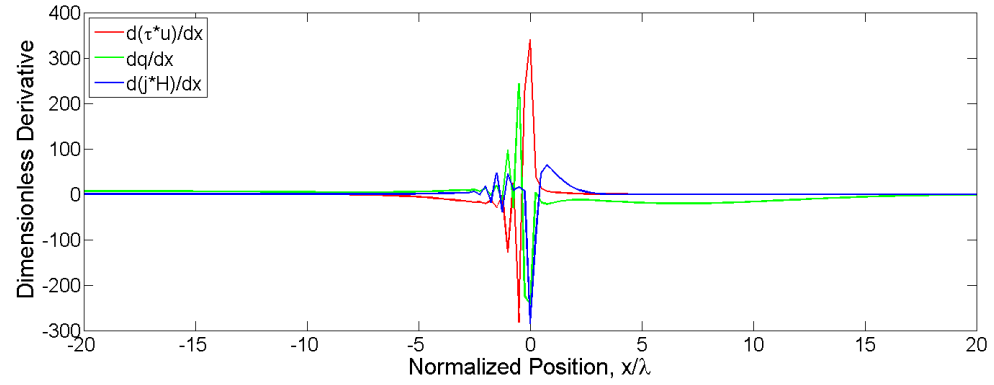

(a)

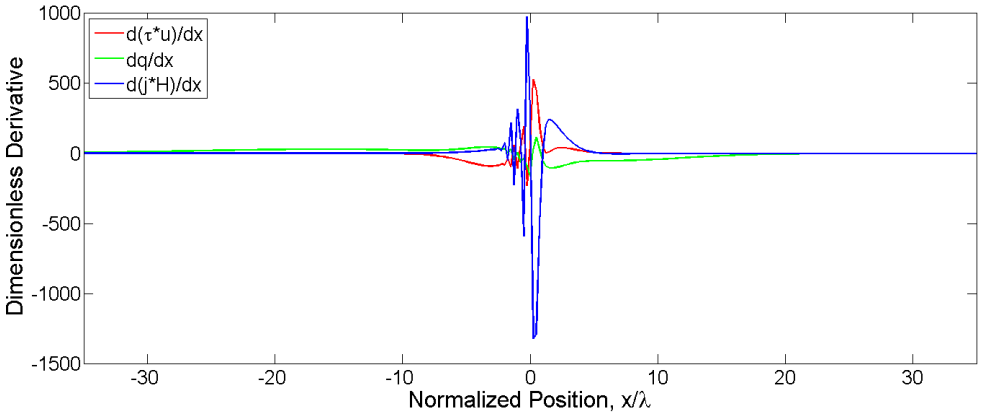

(b)

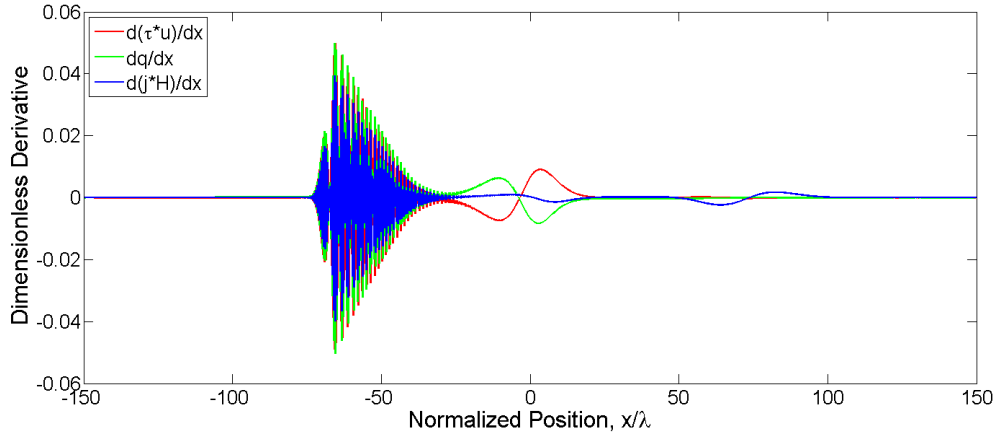

(c)

Figure 7.2.7: Dimensionless Derivative versus Normalized Position for the energy equation applied to porous silica with a density of 0.1 g/cc (a), 0.25 g/cc (b), and 0.77 g/cc (c).

The results in (c) of Fig. 7.2.7 and Fig. 7.2.8 show that the 0.77 g/cc case behaves differently than the 0.1 g/cc and 0.25 g/cc cases.

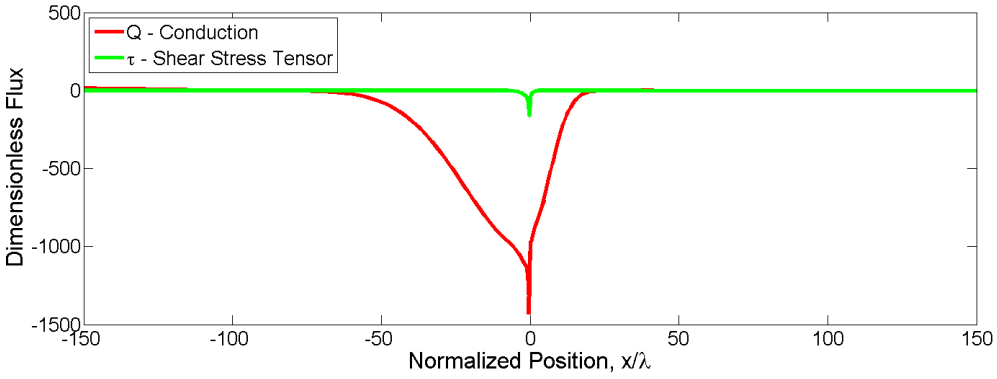

(a)

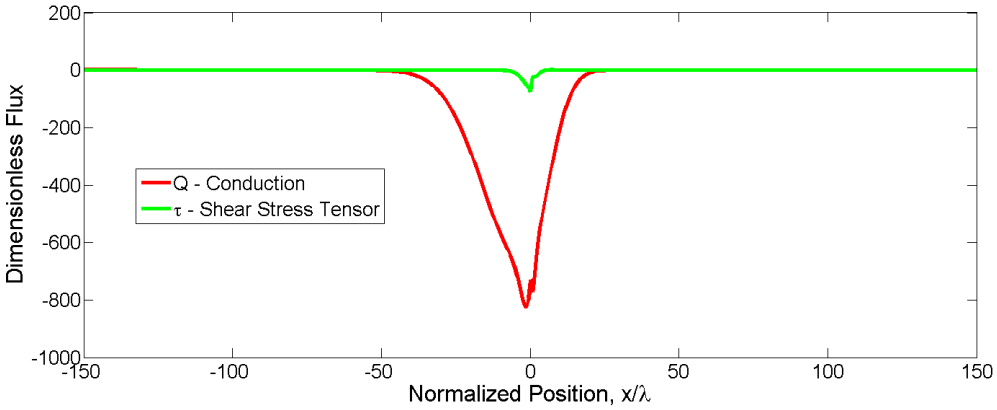

(b)

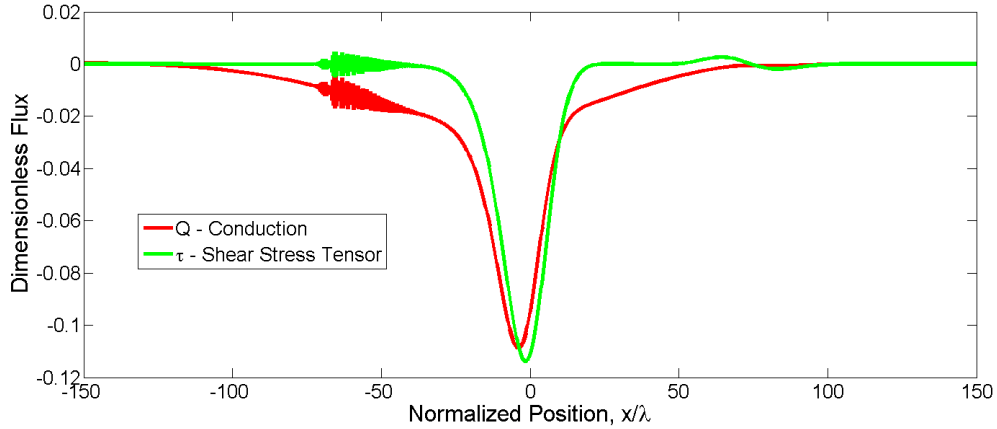

(c)

Figure 7.2.8: Dimensionless Flux versus Normalized Position for the shear stress tensor and heat conduction for porous silica with a density of 0.1 g/cc (a), 0.25 g/cc (b), and 0.77 g/cc (c).

Figure 7.2.8 shows that as initial porosity is increased heat conduction dominates the shear stress tensor, and conversely as initial porosity is decreased the magnitude of the shear stress tensor increases. As noted in Fig. 7.2.8 (c) the shear stress tensor is equal to the heat conduction.

Table 7.2.1 contains the calculated shock front thickness values in nm for porous silica, liquid water, and argon gas. The trends seen in Table 7.2.1 are not consistent with respect to the anticipated values because they are too small. Initial porosity has a significant effect on the shock thickness values for the porous silica. Each silica sample has a different range of values for shock thickness which may be indicative of a compaction wave versus a shock wave. Pressure signatures for porous silica indicate a broad shock front in which porosity is removed from the test sample. In general this compaction wave is much thicker than a shock wave in a fully consolidated material. The numeric simulations of porous silica under predict shock thickness values.

The shock front thickness values for liquid water are not consistent with what is expected. While shock front thickness increases as the pressure increases the values are entirely too large. The shock front in a liquid should be smaller than that of a gas. The results from the numeric simulations of liquid water over predict the shock thickness values.

The shock front thickness values determined from the numeric simulation of the ideal gas argon are consistent with both analytic and experimental data. The values shown in Table 7.2.1 for argon were found using the Power Law viscosity model. The Power Law viscosity model was chosen because it most closely followed the experimental data available in open literature [28]. In experiments that directly measured

shock front thickness as a function of Mach number the results resemble a bell curve. At lower Mach number the shock front is some finite thickness which reduces until it reaches a minimum value and then proceeds to increase again as the Mach number increases. Shock front thickness values obtained from numeric simulations of argon gas are quantitatively accurate and consistent with experimental data and analytic solutions.

Table 7.2.2: Shock front thickness values in nm for porous silica, water, and ideal gas argon.

Solids	*Silica*	*Shock Front Thickness*
	0.10 g/cc	1.6 nm → 16 nm
	0.25 g/cc	4.0 nm → 16 nm
	0.77 g/cc	8.1 nm → 32 nm
Liquids	*Water*	*Shock Front Thickness*
	Low Pressure	310 nm
	High Pressure	868 nm
Ideal Gas	*Argon*	*Shock Front Thickness*
	Mach 1.55	419 nm
	Mach 3.38	184 nm
	Mach 9	228 nm

Chapter 8

8.1 Conclusions

There are several conclusions that can be made based on the work presented here. The first conclusion is that the analytic 6^{th} order polynomial for the cold curve representation for the Mie-Grüneisen does improve the predictive capabilities of a hydrocode when applied to a lagrangian formulation such as KO. The 5^{th} order representation based on the exact solution as used in CTH performs better in general but cannot simulate the unique features seen in pressure signatures for distended materials such as porous silica. The work presented here leads to the conclusion that numerically solving the cold curve error function is the most accurate way to predict pressure based on strain when using the Mie-Grüneisen equation of state. This method is thought to be more accurate than using a polynomial to represent the exact solution because at high strain the representative solution may deviate from the exact solution, whereas if one uses the exact solution at every point then numeric error should be less than using a representative method.

The other conclusion is the Navier-Stokes equations using the Mie-Grüneisen equation of state can be applied to gases, liquids, and solids in the form of porous/granular or distended materials. The NS formulation works well for the ideal gas argon. Entropy values found by integrating over the shock front match values obtained through the analytic equation for the change in entropy for an ideal gas. Reciprocal shock thickness values at high resolution converge on the values obtained experimentally. However, it should be noted that the NS formulation failed to match the experimentally

obtained shock thickness value for liquid water. Entropy production values were not available for liquid water in the pressure ranges tested. The unique features observed in the experimentally obtained pressure signatures for porous silica were not observed in the numeric simulations performed in this work. In liquids and solids the domain size must be increased to allow time for high frequency disturbances to either dampen out or if they will not dampen out for the code to numerically resolved the shock front.

Viscous dissipation and heat conduction are not sufficient to dampen out numeric noise in liquids and solids. To alleviate this problem one must use large domains and take small time steps. It has been observed in this work that in distended materials heat conductions dominates at high porosity but as porosity is removed heat conduction and the shear stress tensor become equal in magnitude. This is consistent with what is known about distended materials versus their fully consolidated counter parts i.e. for the same dynamic loading condition the temperature is higher for the porous material as opposed to the fully consolidated version. Care must be taken in regards to the boundary conditions when using the Navier-Stokes formulation on a liquid or solid because the jump conditions and the equation of state used may not return the same values for the far field boundary conditions. In this work that problem was solved by recalculating the Grüneisen parameter so that the Mie-Grüneisen equation of state intersected the Rayleigh and Fanno lines which describe the jump conditions.

8.2 Future Work

Code up the exact solution to the cold curve error function and implement it into the lagrangian hydrocode KO. While this approach is computationally expensive it seems to be the most accurate way of implementing the Mie-Grüneisen equation of state.

Incorporate a strength of material model or plastic work model into the Navier-Stokes formulation because they would serve as another method of energy dissipation for solids to go along with viscous dissipation and heat conduction. Also the use of a strength of material model or plastic work model may allow the NS formulation to capture the unique features seen the pressure signatures of distended materials being dynamically loaded. The domain size should be increased to match the grain size of the porous medium, approximately 50 microns. In this work the length scale used for simulating the porous silica was on par with the bond length of silica dioxide which is 16.2 nanometers. Grain dynamics play an important role in the dynamic compaction of porous materials and by changing the scale over which NS formulation is applied some of those features may be captured in a simulation. Finally, entropy in the form of the second law may be included in the governing equations of both the NS and KO formulations. Inclusion of the second law into the derivation may become necessary if the addition of a strength of material model or plastic work model fails to add enough irreversibility into the model to dampen out the numeric noise.

Chapter 9

Appendix – Governing Equations – KO Formulation

9.1 Mass Conservation – Lagrangian Form

$$\frac{D\rho}{Dt} + \rho\nabla\cdot\vec{V} = 0;$$

$\frac{D\rho}{Dt} =$ The time rate of change of density of the element as it moves in space.

$\rho\nabla\cdot\vec{V} =$ The density multiplied by the time rate of change of the volume of a moving element per unit volume.

Mass is not allowed to flow into or out of the system or element therefore $\frac{D\rho}{Dt} = -\rho\nabla\cdot\vec{V}.$

9.2 Momentum Conservation – Lagrangian Form

$$\frac{D\rho\vec{V}}{Dt} = -\nabla\vec{P} + \nabla\cdot\vec{\vec{\sigma}} + \rho\vec{g}$$

$\frac{D\rho\vec{V}}{Dt}$ = The time rate of change of the element velocity and density.

$-\nabla\vec{P}$ = The mechanical pressure exerted on surface element.

$+\nabla\cdot\vec{\vec{\sigma}}$ = The shear force as element resist shear distortion due to ΔP exerted on element surface.

$\rho\vec{g}$ = The gravitational force.

Assumptions

Effects of gravity and external forces are negligible, $\rho\vec{g} = 0$.

$$\frac{\rho D\vec{V}}{Dt} = -\nabla\vec{P} + \nabla\cdot\vec{\vec{\sigma}}$$

Where $\vec{P}$ is mechanical pressure and $\vec{\vec{\sigma}}$ is deviatoric shear distortion.

9.3 Energy Conservation – Lagrangian Form

Starting Assumptions

No nuclear energy; No radiative energy; No electromagnetic energy;
No chemical energy; No potential energy; Constant Entropy

$$\frac{D}{Dt}\left(\rho e+\rho\frac{\vec{V}^2}{2}\right)=-\rho\dot{q}+\rho(\vec{V}\cdot\vec{g})-\nabla\cdot(k\vec{T})-\left(\nabla\cdot\vec{P}\vec{V}\right)-\nabla\cdot\left[\vec{\vec{\sigma}}\cdot\vec{V}\right]$$

$\frac{D}{Dt}\left(\rho e+\rho\frac{\vec{V}^2}{2}\right)=$ The total energy per unit volume.

$\rho\dot{q}=$ The internal heat generation per unit volume.

$\rho(\vec{V}\cdot\vec{g})=$ The energy associated body forces per unit volume.

$\nabla\cdot(k\vec{T})=$ The energy associated with heat conduction per unit volume.

$\left(\nabla\cdot\vec{P}\vec{V}\right)=$ The work done on element per unit volume by mechanical pressure.

$\nabla\cdot\left[\vec{\vec{\sigma}}\cdot\vec{V}\right]=$ The work done on element per per unit volume due to resistance of shear distortion.

Simplifying Assumptions

No internal heat generation $\rho\dot{q}=0.$

Assume adiabatic conditions before and after the shock front $\nabla\cdot(k\vec{T})=0.$

Effects of gravity and external forces are negligible $\rho\left(\vec{V}\cdot\vec{g}\right)=0.$

Simplified Energy Equation

$$\frac{D}{Dt}\left(\rho e+\rho\frac{\vec{V}^2}{2}\right)+\left(\nabla\cdot\vec{P}\vec{V}\right)+\nabla\cdot\left[\vec{\vec{\sigma}}\cdot\vec{V}\right]=0,$$

$$\dot{E}=\text{ Internal }+\text{ Kinetic }=\text{ Total Energy }=\frac{D}{Dt}\left(\rho e+\rho\frac{\vec{V}^2}{2}\right),$$

$$\dot{E}+\left(\nabla\cdot\vec{P}\vec{V}\right)+\nabla\cdot\left[\vec{\vec{\sigma}}\cdot\vec{V}\right]=0.$$

Where $\vec{P}$ is mechanical pressure and $\vec{\vec{\sigma}}$ is deveatoric shear distortion.

9.4 Stress-Strain Relation

The mean pressure, P is defined as $P = -\frac{1}{3}(\sigma_{xx} + \sigma_{yy} + \sigma_{zz})$.
The principle stress in the element, σ is defined as $\sigma_{ii} = (-P + q) + s_{ii}$,
where q is artificial viscosity and $i = j$.

Along the principle axis the resistance to shear distortion,
s is defined as $s_{ii} = 2\mu(\varepsilon_{ii} - \frac{1}{3}\frac{\Delta V}{V})$ where $i = j$.

The cross terms for stress and distortion are as follows; $\sigma_{ij} = s_{ij}$,
where $s_{ij} = 2\mu\varepsilon_{ij}$ where $i \neq j$

Using the continuity equation the relationship between the
change in volume and the strain is as follows;

$$\frac{\Delta \mathrm{V}}{\mathrm{V}} = \varepsilon_{xx} + \varepsilon_{yy} + \varepsilon_{zz}.$$

Note: Stress deviators are defined so that they do not contribute
to the mean pressure, P.

BIBLIOGRAPHY

VonNeumann, J., Richtmyer, R. D., 1950, "A Method for the Numerical Calculation of Hydrodynamic Shocks", J. Applied Physics, 21, pp 232-237.

Wilkins, M. L., 1980, "Use of Artificial Viscosity in Multidimensional Fluid Dynamic Calculations", J. Comp. Phy., 36, pp 281-303.

Caramana, E. J., Shashkov, M. J., Whalen, P. P., 1998, "Formulations of Artificial Viscosity for Multi-dimensional Shock Wave Computations", J. Comp. Phy., 144, pp 70-97.

Borg, J. P., Chapman, David, J., Tsembelis, Kostas, Proud, William, G., Cogar, John R., 2005, "Dynamic Compaction of Porous Silica Powder", J. of Appl. Physics 98, 073509.

Herrmann, W., 1969, "Constitutive Equation for the Dynamic Compaction of Ductile Porous Materials" J. Appl. Phys. 40, No. 6.

Grady, D. E., Winfree, N. A., 2001, "A Computational Model for Polyurethane Foam" In: Staudhamer , Murr and Meyers , editors, Fundamental Issues and Applications of Shock-Wave and High-Strain-Rate Phenomena. Elservier-Science. pp 485-491.

Chtourou, H., Gakwaya, A., Guillot, M., 2002, "Modeling of the Metal Powder Compaction Process using the CAP Model. Part I. Experimental Material Characterization and Validation" Int. J. Solids Struct., 39.

Hayes, D. B., 1973, "Introduction To Stress Wave Phenomena", Lecture Notes.

Wilkins, M. L., 1999, Computer Simulation of Dynamic Phenomena. Springer ISBN 3-540-63070-8.

Benson, D.J., 1990, Computational Methods in Lagrangian and Eulerian Hydrocodes, Dept. of AMES.

R. Landshoff, 1955, "A Numerical Method for Treating Fluid Flow in the Presence of Shocks," Los Alamos Scientific Laboratory Report LA-1930.

Elizarova, G. T., Shirokov, I. A., Montero, S., 2005, "Numerical simulation of shock-wave structure for argon and helium", Physics of Fluids, 17, 068101.

Johnson, J. N., 1968, "Single-Particle Model of a solid: The Mie-Gruneisen Equation*", Am. J. Physics, 36, No. 10, pp 917-919.

Davison, L., Graham, R., 1979, A Phys. Rep. 55 255-379.

Z. Rosenberg, D. Yaziv, and Y. Partom, 1980, "Calibration of foil-like Manganin gauges in planar shock wave experiments," Journal of Applied Physics **51**(7) 0021-8979/80/073702-04.

D. Yaziv, Z. Rosenberg, and Y. Partom, 1980, "Release wave calibration of Manganin gauges," Journal of Applied Physics **51**(12) 0021-8979/80/126055-03.

W. Mock, Jr., and W.H. Holt, 1976, Report NSWC/DL TR-3473, Naval Surface Weapons Center, Dahlgren, VA.

W. Mock, Jr., and Susan Bartyczak, 2008, Private Communication, Naval Surface Warfare Center, Dahlgren, VA.

Millett, J. C. F., Bourne, N. K., 2006, "The shock induced equation of state and shear strength of polyvinylidene difluoride", J. of Applied Physics 134, pp 719-724.

Bell RL, Baer MR, Brannen RM, Elrich MG, Hertel ES, Silling SA, and Taylor PA., 2003 CTH user's manual and input instructions. Sandia National Laboratories Tech. Rept.

Zel'dovich, Ya. B., Raizer, Yu. P., 1967, "Physics of Shock Waves and High-Temperature Hydrodynamic Phenomena," Academic Press, Inc.

Meyers, M. A., 1994, "Dynamic Behavior Of Materials," John Wiley & Sons, Inc., 1994.

Gust, W. H., 1982, "High impact deformation of metal cylinders at elevated temperatures", J. of Applied Physics 53(5), 3566.

Borg, J. P., Cogar, J. R., Lloyd, A., Ward, A., Chapman, D., Tsembelis, K., Proud, W. G., 2006, "Computational Simulations of the Dynamic Compaction of Porous Media", Int, J. Impact Eng., 33, pp 109-118.

Kerley, G. I., 1997, "Modifications to the Mie-Grüneisen EOS in the CTH Code", Report for NSWC, Dahlgren Division, KPS97-8.

Elizarova, G. T., Khokhlov, A. A., Montero, S., 2007, "Numerical simulation of shock wave structure in nitrogen", Physics of Fluids, 19, 068102.

Alsmeyer, H., 1976, "Density profiles in argon and nitrogen shock waves measured by the absorption of an electron bean", J. Fluid Mech. 74, pp 497.

Bird, B. R., Stewart, E. W., Lightfoot, N. E., 2002, "Transport Phenomena," Second Edition. John Wiley & Sons, Inc.

Nagayama, K., Mori, Y., Shimada, K., 2002, "Shock Hugoniot compression curve for water up to 1 GPa by using a compressed gas gun", J. of Applied Physics 91(1), 476.

Morley, J. Michael, 2011, "Shock compression of water and solutions of ammonium nitrate," PhD Thesis, University of Cambridge, 2011.

Skryl, Yu., Belak, A. Anna, Kuklja, M. Maija, 2007, "Shock-induced polarization in distilled water," Physical Review B 76, 064107.

Goldman, N., Fried, E. L., Mundy, J. C., Kuo, I-F. W., Curioni, A., Reed, J. E., 2007, "*Ab initio* Molecular Dynamics Simulations of Water Under Static and Shock Compressed Conditions," APS Conference on Shock Conditions of Condensed Matter, Kona, HI, June.

Hamad, Hanna, 1996, "Effect of viscosity on the structure of shock waves," Mathematical, Physical and Engineering Sciences, Vol 452, No. 1953, pp. 2163-2172.

Sohrab, H. S., 2007 "A Modified Hydro-Thermo-Diffusive Theory of Shock Waves," 4th WSEAS International Conference on Fluid Mechanics, Queensland, Australia, January, pp 54-59.

Anderson, D. J., 1995, "Computational Fluid Dynamics," McGraw-Hill, Inc., Singapore, ISBN 0-07-113210-4.

Boehler, Reinhard, Kennedy, C. George, 1977, " Pressure dependence of the thermodynamical Grüneisen parameter of fluids," J. Appl. Phys., Vol 48, No 10, October 1977.

Landau, L. D., Lifshitz, E. M., 1987, " Fluid Mechanics," 2nd Edition, Pergamon Press, Toronto, Ontario, Canada, 1987.

Mahdief, M. H., Hall, T. A., 2003, "Real temperature calculation of shock wave driven by sub-nanosecond laser pulses," J. Phys. D: Appl. Phys. 36 (2003) 1188-1191.

Hoover, G. Wm., Hoover, G. C., 2010, "Flexible Macroscopic Models for Dense-Fluid Shockwaves: Partitioning Heat and Work; Delaying Stress and Heat Flux; Two-Temperature Thermal Relaxation," Cond-Mat. Stat-Mech. 10 May 2010, arXiv:1005.1525v1.

Xu, Kun, 2001, "Regularization of the Chapman-Enskog Expansion and Its Description of Shock Structure," NASA/CR-2001-211268, ICASE Report No. 2001-39.

Walsh, M. J., Rice, H. M., 1957, "Dynamic Compression of Liquids from Measurements on Strong Shock Waves," Journal of Chemical Physics, Volume 26, No. 4, April 1957.

Arp, V., Persichetti, M. J., Guo-bang, C., 1984, "The Grüneisen Parameter in Fluids," Journal of Fluids Engineering, Vol. 106, June 1984, pp 193-200.

Hamad, H., 1999, "On the structure of an inviscid shock wave," Acta Mechanica 138, 61-73 (1999).

Iannelli, Joe, 2011, "An implicit Galerkin finite element Runge-Kutta algorithm for shock-structure investigations," Journal of Computational Physics 230 (2011) pp 260-286.

Molinari, A., Ravichandran, G., 2004, "Fundamental structure of steady plastic shock waves in metals," Journal of Applied Physics, Vol. 95, No. 4, 15 February 2004, pp 1718-1732.

Xu, Kun, Prendergast, H. K., 1994, "Numerical Navier-Stokes Solutions from Gas Kinetic Theory," Journal of Computational Physics, Vol. 114, pp 9-17, 1994.

Xu, Kun, 2001, "A Gas-Kinetic BGK Scheme for the Navier-Stokes Equations and Its Connection with Artificial Dissipation and Godunov Method," Journal of Computational Physics, Vol. 171, pp 289-335, 2001.

Gilbarg, D., Paolucci, D., 1953, "The structure of shock waves in the continuum theory of fluids," J. Rat. Mech. Anal. 2, 617 (1953).

Meyers, A. M., Benson, J. D., Olevsky, A. E., 1999, "Shock Consolidation: Microstructurally-Based Analysis and Computational Modeling," Acta Mater, Vol. 47, No. 7, pp. 2089-2108, 1999.

Benson, J. D., 1992, "Computational methods in Lagrangian and Eulerian hydrocodes," Computer Methods in Applied Mechanics and Engineering, Vol. 99, pp 235-394 (1992).

Borg, P. John, Vogler, J. T., 2008, "Mesoscale calculations of the dynamic behavior of a granular ceramic," International Journal of Solids and Structures, Vol. 45, pp 1676-1696 (2008).

Bourne, K. N., Rosenberg, Z., Johnson, J. D., Field, E. J., Timbs, E. A., Flaxman, P. R., 1995, "Design and construction of the UK Plate Impact facility," Meas. Sci. Technol, Vol. 6, pp 1462-1470 (1995).

Benson, J. David, Nellis, J. W., 1994, "Dynamic compaction of copper powder: Computational and experiment," Appl. Phys. Lett. Vol. 65, No. 4, pp 418-420, 25 July 1994.

Borg, P. J., Chapman, J. D., Tsembelis, K., Proud, G. W., Cogar, R. J., 2005, "Dynamic compaction of porous silica powder," Journal of Applied Physics, Vol. 98, 073509 (2005).

Benson, J. David, 1994, "An analysis by direct numerical simulation of the effects of particle morphology on the shock compaction of copper power," Modeling Simul. Mater. Sci. Eng. Vol. 2, pp 535-550 (1994).

Dolan, H. D., Johnson, N. J., Gupta, M. Y., 2005, "Nanosecond freezing of water under multiple shock wave compression: Continuum modeling and wave profile measurements," J. Chem. Phys. Vol. 123, 064702 (2005).

Dolan, H. D., Gupta, M. Y., 2004, "Time Dependent Freezing of Water under Multiple Shock Wave Compression," AIP Conf. Proc. July 20, 2004, Vol. 706, pp 167-171.

Vogel, A., Busch, S., Parlitz, U., 1996, "Shock wave emission and cavitation bubble generation by picoseconds and nanosecond optical breakdown in water," J. Acoust. Soc. Am. Vol. 100 (1), July 1996, 0001-4966/100(1)/148/18.

REFERENCES

[1] VonNeumann, J., Richtmyer, R. D., "A Method for the Numerical Calculation of Hydrodynamic Shocks", J. Applied Physics, 21, pp 232-237, 1950.

[2] Wilkins, M. L., "Use of Artificial Viscosity in Multidimensional Fluid Dynamic Calculations", J. Comp. Phy., 36, pp 281-303, 1980.

[3] Caramana, E. J., Shashkov, M. J., Whalen, P. P., "Formulations of Artificial Viscosity for Multi-dimensional Shock Wave Computations", J. Comp. Phy., 144, pp 70-97, 1998.

[4] Borg, J. P., Chapman, David, J., Tsembelis, Kostas, Proud, William, G., Cogar, John R., "Dynamic Compaction of Porous Silica Powder", J. of Appl. Physics 98, 073509, 2005.

[5] Herrmann, W., "Constitutive Equation for the Dynamic Compaction of Ductile Porous Materials" J. Appl. Phys. 40, No. 6, 1969.

[6] Grady, D. E., Winfree, N. A., "A Computational Model for Polyurethane Foam" In: Staudhamer , Murr and Meyers , editors, Fundamental Issues and Applications of Shock-Wave and High-Strain-Rate Phenomena. Elservier-Science. pp 485-491, 2001.

[7] Chtourou, H., Gakwaya, A., Guillot, M., "Modeling of the Metal Powder Compaction Process using the CAP Model. Part I. Experimental Material Characterization and Validation" Int. J. Solids Struct., 39, 2002.

[8] Hayes, D. B., "INTRODUCTION TO STRESS WAVE PHENOMENA", Lecture Notes, 1973.

[9] Wilkins, M. L., Computer Simulation of Dynamic Phenomena. Springer ISBN 3-540-63070-8, 1999.

[10] Benson, D.J., Computational Methods in Lagrangian and Eulerian Hydrocodes, Dept. of AMES, 1990.

[11] R. Landshoff, "A Numerical Method for Treating Fluid Flow in the Presence of Shocks," Los Alamos Scientific Laboratory Report LA-1930, 1955.

[12] R. Landshoff, "A Numerical Method for Treating Fluid Flow in the Presence of Shocks," Los Alamos Scientific Laboratory Report LA-1930, 1955.

[13] Elizarova, G. T., Shirokov, I. A., Montero, S., "Numerical simulation of shock-wave structure for argon and helium", Physics of Fluids, 17, 068101, 2005.

[14] Johnson, J. N., "Single-Particle Model of a solid: The Mie-Gruneisen Equation*", Am. J. Physics, 36, No. 10, pp 917-919, 1968.

[15] Davison, L., Graham, R., A Phys. Rep. 55 255-379, 1979.

[16] Z. Rosenberg, D. Yaziv, and Y. Partom, "Calibration of foil-like Manganin gauges in planar shock wave experiments," 1980 Journal of Applied Physics **51**(7) 0021-8979/80/073702-04.

[17] D. Yaziv, Z. Rosenberg, and Y. Partom, "Release wave calibration of Manganin gauges," 1980 Journal of Applied Physics **51**(12) 0021-8979/80/126055-03.

[18] W. Mock, Jr., and W.H. Holt, Report NSWC/DL TR-3473, Naval Surface Weapons Center, Dahlgren, VA, July 1976.

[19] W. Mock, Jr., and Susan Bartyczak, Private Communication, Naval Surface Warfare Center, Dahlgren, VA 2008.

[20] Millett, J. C. F., Bourne, N. K., "The shock induced equation of state and shear strength of polyvinylidene difluoride", J. of Applied Physics 134, pp 719-724, 2006.

[21] Bell RL, Baer MR, Brannen RM, Elrich MG, Hertel ES, Silling SA, and Taylor PA. CTH user's manual and input instructions. Sandia National Laboratories Tech. Rept. April 2003.

[22] Zel'dovich, Ya. B., Raizer, Yu. P., Physics of Shock Waves and High-Temperature Hydrodynamic Phenomena. Academic Press, Inc., 1967.

[23] Meyers, M. A., DYNAMIC BEHAVIOR OF MATERIALS. John Wiley & Sons, Inc., 1994.

[24] Gust, W. H., "High impact deformation of metal cylinders at elevated temperatures", J. of Applied Physics 53(5), 3566, 1982.

[25] Borg, J. P., Cogar, J. R., Lloyd, A., Ward, A., Chapman, D., Tsembelis, K., Proud, W. G., "Computational Simulations of the Dynamic Compaction of Porous Media", Int, J. Impact Eng., 33, pp 109-118, 2006.

[26] Kerley, G. I., "Modifications to the Mie-Grüneisen EOS in the CTH Code", Report for NSWC, Dahlgren Division, KPS97-8, 1997.

[27] Elizarova, G. T., Khokhlov, A. A., Montero, S., "Numerical simulation of shock wave structure in nitrogen", Physics of Fluids, 19, 068102, 2007.

[28] Alsmeyer, H., "Density profiles in argon and nitrogen shock waves measured by the absorption of an electron bean", J. Fluid Mech. 74, pp 497, 1976.

[29] Bird, B. R., Stewart, E. W., Lightfoot, N. E., Transport Phenomena: Second Edition. John Wiley & Sons, Inc., 2002.

[30] Boehler, Reinhard, Kennedy, C. George, " Pressure dependence of the thermodynamical Grüneisen parameter of fluids," J. Appl. Phys., Vol 48, No 10, October 1977.

[31] Nagayama, K., Mori, Y., Shimada, K., "Shock Hugoniot compression curve for water up to 1 GPa by using a compressed gas gun", J. of Applied Physics 91(1), 476, 2002.

[32] Morley, J. Michael, 2011, "Shock compression of water and solutions of ammonium nitrate," PhD Thesis, University of Cambridge, 2011.

[33] Vogel, A., Busch, S., Parlitz, U., "Shock wave emission and cavitation bubble generation by picoseconds and nanosecond optical breakdown in water," J. Acoust. Soc. Am. Vol. 100 (1), July 1996, 0001-4966/100(1)/148/18.